Doctoral Thesis

Numerical Simulations of Strained Non-premixed Flames with Thermal Radiation: Intrinsic Flame Instabilities and Supercritical CO_2 Oxy-fuel Combustion

Hyun Su Bak

Department of Mechanical Engineering

Graduate School of UNIST

2020

Numerical Simulations of Strained Non-premixed Flames with Thermal Radiation: Intrinsic Flame Instabilities and Supercritical CO_2 Oxy-fuel Combustion

Hyun Su Bak

Department of Mechanical Engineering

Graduate School of UNIST

Numerical Simulations of Strained Non-premixed Flames with Thermal Radiation: Intrinsic Flame Instabilities and Supercritical CO_2 Oxy-fuel Combustion

A thesis/dissertation
submitted to the Graduate School of UNIST
in partial fulfillment of the
requirements for the degree of
Doctor of Philosophy

Hyun Su Bak

05/27/2020

Approved by

Advisor
Chun Sang Yoo

Numerical Simulations of Strained Non-premixed Flames with Thermal Radiation: Intrinsic Flame Instabilities and Supercritical CO_2 Oxy-fuel Combustion

Hyun Su Bak

This certifies that the thesis/dissertation of Hyun Su Bak is approved.

05/27/2020

Advisor: Chun Sang Yoo

Jaeseon Lee

Jae Hwa Lee

Jooha Kim

Jeong Park

Abstract

Flame instabilities of opposed non-premixed tubular flames are numerically investigated under adiabatic and non-adiabatic conditions. The 1-D/2-D detailed numerical simulations with the linear stability analysis are performed to analyze the regimes which show the flame instabilities. Through 2-D simulations, it is proved that the instability characteristics by 1-D simulations and linear stability analysis can be predicted with reasonable accuracy. In addition, it is found that the discrepancy between experiments and numerical studies comes from locally-strong reaction zones by large order of perturbation. The radiation effects on opposed non-premixed tubular flames are also investigated in the same manner, for which dual extinction limits are observed. The cellular instability and oscillatory instability are identified near the radiation-induced extinction limit. As different initial flames, such as C-shaped or asymmetric IC, the total extinction from head-on collision between two propagating flame cells or a rotating flame cell are observed over the radiation-induced extinction limit. Under extremely large radiation intensity, all non-premixed tubular flames are stable in the form of cellular flames.

Under supercritical CO_2 (sCO_2) oxy-fuel combustion conditions, flame structure and NO_X emission characteristics are identified by 1-D numerical simulations using a modified OPPDIF code. To reflect real-gas effects at extremely high pressure, the Soave Redlich-Kwong equation of state, thermodynamic and transport models for real fluid are implemented to the code. Through various numerical simulations, it is found that the ingress of N_2 from oxidizer side can be more fatal to NO_X generation because of higher N_2 concentration in the flame zone. Also, the pressure effects on NO_X formation are obtained by NO_X reaction pathway analysis.

Although there are many numerical studies on the sCO_2 oxy-fuel combustion, the radiative heat transfer has not been considered so far. The main reason using adiabatic condition is the absence of an appropriate radiation model for extremely high pressure. Therefore, two different weighted sum of gray gases (WSGG) models for the pressure

of 300 bar are estimated by using the parameters from the pressurized WSGG model (Shan et al., *Int. J. Heat Mass Transf.* 121 (2018) 999–1010) by using two different extrapolation ways: One is the WSGG-Linear that estimates the absorption coefficients of four gray gases using those at 1 bar multiplied by the total pressure and the weighting factors at 1 bar. The other is the WSGG-Log that estimates the emissivity and absorption coefficients with a logarithmic function. It is found that the temperature reduction by radiative heat loss is marginal in the most range of strain rate in spite of the high pressure and abundant CO_2 conditions.

To extend the fundamental understanding to practical problem, 3-D Reynolds-averaged Navier-Stokes equations (RANS) simulations of turbulent reacting flows in a model gas turbine combustor are conducted to figure out the characteristics of partially premixed flames as different geometry of nozzle and NO_X emission. It is obtained that the high swirler nozzle cases shows more stable than the low swirler nozzle cases due to relatively-strong recirculation zones. However, the NO_X emission is more generated in the high swirler nozzle cases than low swirler nozzle cases, because the longer residence time is, the more NO_X is generated. As transferring the temperature and pressure field to solid region for boundary condition, the thermal fatigue analysis is performed to find the vulnerable parts in the combustor.

Contents

List of Figures

Chapter I

Introduction

1.1 Intrinsic Flame Instabilities

1.1.1 Cellular Flame Instability

In most practical engines, combustion instabilities need to be avoided because they may deteriorate the integrity of the mechanical systems in the engines. Occasionally, however, the cellular flame instability may play a positive role by enhancing the operation range of hydrogen-fueled engines by extending the extinction limit of hydrogen/air flames [3–5]. For meso-scale combustors, moreover, the flame instability can also be utilized to achieve stable combustion by increasing heat release per unit volume and consequently, compensating for increased heat losses associated with the high surface-to-volume ratios of such small-scale devices [6]. As such, the cellular flame instability has been extensively investigated in the combustion community not only because of its practical importance, but because of its most dynamical and beautiful features among combustion dynamics [3–8].

There exist three different modes of cellular flame instability, i.e. hydrodynamic instability, buoyancy-driven instability, and diffusive-thermal (D-T) instability [5]. The hydrodynamic instability is caused by a finite density drop across a premixed flame such that it is absolutely unstable to perturbations at all wavelengths. The buoyancy-driven instability occurs under the condition of negative density stratification in the direction

of gravity and, as such, an upwardly-propagating premixed flame is buoyantly unstable. The D-T instability occurs due to the imbalance between diffusion of heat and mass at a flame front such that a flame can be stable or unstable depending on the mixture Lewis number upstream of the flame front [4, 5, 9].

Although these cellular flame instabilities are intrinsic characteristics of premixed flames, the D-T instability has also been observed in many non-premixed flames with their effective Lewis number being less than unity near the extinction limit [3,9–16]. The structure of non-premixed flames becomes similar to that of premixed flames near extinction, and as such, they are considered to be in the "premixed flame regime" according to Liñán's asymptotic study of a non-premixed counterflow flame [5,10,17]. From this point of view, it is a natural extension that non-premixed flames near extinction would also exhibit cellular flame structures like premixed flames when the effects of the preferential diffusion and/or curvature become significant [10].

Among the many different flow configurations, an opposed non-premixed tubular flow is an ideal one to simultaneously investigate the effects of stretch rate and curvature on the characteristics of the D-T instability [3]. In this configuration the stretch rate and curvature are independently specified and hence their effects on the cellular flame instability can systematically be investigated. In this context, the characteristics of opposed non-premixed tubular flames have extensively been investigated by Pitz and coworkers [3, 15, 16, 18–20]. As mentioned above the D-T instability of non-premixed tubular flame also occurs near the extinction limit when the Lewis number of the fuel is less than unity [3,15,16]. Near extinction, small perturbations can induce alternating locally-weak and strong reaction regions of the tubular flame due to the focusing and defocusing effects of mass and heat diffusion, leading to the formation of flame cells. The resultant temperature at the edge of a flame cell is higher than it is in the central part due to the strong focusing of the fuel mass flux at the edge. By the same mechanism flame cells can survive beyond the one-dimensional (1-D) flame extinction limit [12, 13].

Although numerous experimental and theoretical/numerical studies of cellular flame instability in tubular and counterflow flames have been conducted [4, 5, 11–13, 18, 21–24], a numerical study of the D-T instability in opposed non-premixed tubular flames has not

been performed. Moreover, discrepancies still remain between experimental/numerical observations of cellular flame instability and theoretical prediction via linear stability analysis [13,21] even though linear stability analysis predicts numerical simulation results with reasonable accuracy [24]. In Chapter II, therefore, the D-T instability of opposed non-premixed tubular flames near stretch-induced extinction limit is investigated by using 1-D/2-D detailed numerical simulations with the linear stability analysis.

1.1.2 Radiation-induced limit phenomena

Flames under microgravity exhibit quite different behaviors from their corresponding flames under normal gravity mainly due to buoyancy-free environments. Therefore, numerous theoretical and experimental studies have been performed to elucidate their characteristics especially near ignition/extinction limits [25–28]. For instance, the ignition, flame spreading, and extinction characteristics of weakly-strained flames in a spacecraft have been extensively investigated because such flame characteristics found under normal gravity cannot be directly used for the fire-safety assessment of a spacecraft [5]. The existence of a steady spherical premixed flame or a flame ball has been verified in microgravity experiments. Moreover, flame balls cannot survive beyond a critical flame radius due to stretch effect and radiative heat loss [5, 29–34].

Diffusion- and/or radiation-induced limit phenomena including cellular flame instability and radiation-induced flame extinction have also been widely investigated because they become prominent in microgravity environments. For a non-premixed flame under microgravity, its flame thickness usually increases with decreasing stretch rate, and hence, radiative heat loss can significantly reduce flame temperature, leading to an extinction [35]. The characteristics of low-stretched flame extinction by excessive radiative heat loss have been extensively investigated in various conditions [36–44]. In particular, the effects of radiative heat loss on spherical non-premixed flames under microgravity have been identified through comprehensive experimental measurements of flame radius, temperature, radiation intensity, and soot formation [45, 46].

Various flame instabilities of non-premixed flames have also been reported under mi-

crogravity conditions. However, there have been few studies on flame instabilities induced by radiative heat loss because it is not only observed less frequently but also difficult to construct experimental environments. It has been predicted that the oscillatory instability of non-premixed flames can occur when fuel Lewis number and/or radiative heat loss are large enough [11, 47, 48]. For instance, Sohn et al. [49] numerically investigated nonlinear dynamics of radiation-induced oscillatory instability of non-premixed flames in a 1-D stagnant mixing layer with unity Lewis number such as three different types of flame evolution near radiation-induced extinction limit: the decaying oscillatory solution, diverging solution to extinction, and stable limit-cycle solution. They demonstrated that oscillatory instability occurs prior to extinction due to radiative heat loss, similar to that in a droplet flame experiment in a space shuttle [50].

Moreover, Nanduri et al. [51] investigated the flame structure and dynamics of non-premixed counterflow flames with radiative heat loss for which fuel Lewis number is less than unity. They observed three oscillatory flame responses of decaying oscillation, stable limit-cycle, and oscillatory extinction for low-stretched flames through 1-D numerical simulations. From 2-D numerical simulations, they observed various flames including wavy flames, stationary cellular flames, and propagating cellular flames depending on initial conditions and Damköhler number. In short, various flame responses such as oscillatory and cellular behaviors of low-stretched non-premixed flames have been reported, which is primarily attributed to the Lewis number effect and radiative heat loss. However, detailed investigation on nonlinear evolution of 2-D non-premixed flame oscillations combined with D-T instability through the stability analysis have not been conducted near radiation-induced extinction limit when fuel Lewis number is less than unity. Moreover, the flame dynamics under extremely-large radiative heat loss has not been elucidated. In Chapter III, hence, cellular instability and oscillatory instability of non-premixed tubular flames near radiation-induced extinction limit are investigated by using 1-D/2-D detailed numerical simulations with the linear stability analysis.

1.2 Supercritical Oxy-fuel Combustion

1.2.1 Estimation of N_2 Ingress Situations

As one of next-generation power cycles for enhancing the cycle efficiency and meeting environmental regulations, a direct-fired supercritical carbon dioxide (sCO_2) power cycle, or the Allam cycle, has been highlighted since it was first proposed. The benefits of the cycle mainly originate from its high efficiency, small machinery footprints, and ability of carbon capture and storage [52, 53]. The cycle also adopts oxy-fuel combustion in which natural gas is designed to burn with O_2 diluted only with CO_2 and can literally generate no NO_X emissions. As such, the cycle can be designed without considering NO_X emissions and non-premixed combustion can be utilized for stable operation [52, 54].

However, even for such oxy-fuel combustion, a small amount of N_2 can infiltrate the combustor not only because natural gas typically includes 0–5% of N_2 by volume but also because N_2 can leak into the oxidizer stream through an air separation unit (ASU) that separates oxygen from air. For typical oxy-fuel combustion, the effect of N_2 amount on NO_X emissions was investigated at atmospheric pressure [55,56] but has not been studied at high pressures of 250–300 atm relevant to the sCO_2 oxy-fuel combustion.

For conventional air-fuel combustion, the study of NO_X formation has been also limited to atmospheric or relatively-low pressure conditions. For instance, Drake and Blint [57] investigated the relative importance of thermal NO_X, prompt NO_X, and N_2O pathways for NO_X formation in CH_4/N_2 versus air counterflow non-premixed flames at atmospheric pressure and found that the prompt NO_X mechanism dominates NO_X formation. From experimental and numerical studies at 1–15 atm, Naik et al. [58] found that the thermal NO_X and N_2O pathways play a critical role in generating NO_X at relatively-high pressure conditions while the contribution of prompt NO_X decreases with increasing pressure. In addition, Hewson and Bolling [59] reported the importance of NO_X reburn initiation reactions at relatively-high pressure (e.g. 40 atm). Although the NO_X emission characteristics of the oxy-fuel and air-fuel combustion at atmospheric and relatively-high pressures were investigated, those of the oxy-fuel combustion at extremely high pressures

(e.g. 300 atm) have not been studied. In Chapter IV, therefore, the flame structures and NO_X emission characteristics of supercritical oxy-fuel combustion are found by using 1-D numerical simulations of counterflow CH_4 versus O_2/CO_2 non-premixed flames and discussed with the assumption of various N_2 ingress situations.

1.2.2 Estimation of Radiative Heat Transfer

Including Chapter IV, the fundamental characteristics of sCO_2 oxy-fuel combustion have been numerically investigated [60–62], in which the simulations were conducted under adiabatic condition without considering radiative heat loss. However, there is no reasonable evidence behind the assumption for using the adiabatic condition since there exist large amount of strong absorbers such as H_2O and CO_2 in the combustor. Moreover, it is well known that their optical depth becomes thicker as pressure increases.

In the oxy-fuel combustion, many researchers have focused on developing accurate and efficient thermal radiation models based on enormous spectral data [63–66]. Among various radiation models, the weighted sum of gray gases (WSGG) model based on the statistical narrow band (SNB) model has been considered one of the best compromises between accuracy and computation demand [67]. Since most WSGG models were developed for atmospheric pressure, a pressurized WSGG model was recently proposed, which is validated for pressures up to 30 bar [68]. Although the pressurized WSGG model can be adopted for numerical simulations of current gas turbine combustion, it is not proper for simulations at extremely-high pressures like sCO_2 oxy-fuel combustion. Development of a thermal radiation model at such high pressure is still not feasible because of many difficulties in directly measuring radiative properties. In Chapter V, therefore, the radiation effect on counterflow non-premixed flames under supercritical CO_2 oxy-fuel combustion conditions is estimated by using extrapolated radiative properties.

1.3 Large-scale Numerical Simulations

Although the fundamental characteristics of strained non-premixed flames under various conditions have been numerically investigated as described, another important objective

of numerical simulations in the combustion field is to solve the large-scale problem such as the internal engine, the rocket engine, the gas turbine combustor, the furnace and so on. In particular, the development of high performance computing enable to solve the large and more complicated problems. In the context, Reynolds averaged Navier-Stokes equations (RANS) simulations quickly and easily show practical results even though the accuracy is questionable. Therefore, we introduce and carry out various numerical simulations for the prediction of combustion phenomena, the thermal fatigue, and the NO_X emission.

Thermo-acoustic instability has been a lingering problem since lean premixed combustion was adopted for the gas-turbine combustion to improve its thermal efficiency and eco-friendly power generation [69–71]. Thermal-acoustic instability is a complicated phenomenon induced by the interaction between unsteady heat release and acoustic perturbations. As such, the unexpected accidents have been frequently reported at high temperature components of the gas turbine system such as vane blades and a nozzle tip which are directly exposed to heated products because of the amplification of heat release. The problem not only threatens the safety, but also brings large financial losses by ceasing power production. Similarly, the lack of proper repair and replacement of obsolete and enfeebled components can lead to safety incidents and reduce power generation efficiency. Therefore, the thermal fatigue life of components has investigated to precisely estimate the cycles [72–75].

The fatigue life of high temperature components is generally known to have guidelines provided by the manufacturer. However, because the operation condition changes from time to time, the guidelines are not universal, and especially when operating in cycling mode, the actual life cycles often fall short of the expectancy. Also, frequently turning on/off the power system can negatively affect the entire gas turbine components, leading to reduce fatigue life cycles.

Generally, cycle fatigues are divided into two types; high cycle fatigue (HCF) and low cycle fatigue (LCF) [76, 77]. HCF is a break in a vibrating part with constant and rapid repetition cycles, mainly observed in aircraft fuselage or pumps. Since small stresses in the elastic region are applied, the control of the stress width is a major factor in improving

fatigue life. Therefore, high strength materials are suitable to avoid the problems. On the other hands, LCF is induced by a change in thermal stress and a cyclic load with a slow repetition cycle. In usual, it is known that a high ductile material is advantageous in preventing breakage because a high stress or deformation including the plastic region is applied. Therefore, it is necessary to anticipate the type of fatigue and to use the component of the appropriate material, considering the operation condition.

In addition, power generation technologies including low NO_X concept basically become more important to meet the environmental regulations. The prediction of NO_X emission has been widely investigated by using chemical reactor network (CRN) method [78–81]. Through the comparison between experiments, computational fluid dynamics (CFD) simulations, and CRN analysis, reasonable accuracy has been validated. In this context, numerical analysis becomes essential in various fields. Since it costs enormously to do experiments for a real scale gas turbine with different models and operating conditions, the numerical analysis has been widely used.

In Chapter VI, hence, we shows a series of numerical simulations of a model gas turbine combustor using commercial softwares such as Fluent 2019 R2, CHEMKIN-PRO 2019 R2 [82], and Abaqus 2019 [83] as follows. First, 3-D RANS simulations of a model combustor are carried out and compared to validate numerical models. Second, the CRN method with a detailed chemical reaction mechanism is used to predict the NO_X formation in the combustor. Third, the finite element analysis for the thermal fatigue analysis based on ε-N curve is conducted by using the temperature and pressure field from the RANS simulation.

Chapter II

Flame Instability of Opposed Non-premixed Tubular Flames near Strained-induced Extinction Limit

In this chapter, the D-T instability of opposed non-premixed tubular flames and the dynamics of flame cell formation are investigated using 2-D direct numerical simulations together with conventional linear stability analysis. By comparing previous experimental results with numerical/theoretical predictions, the implication of cellular flame instability found in the numerical simulations on the experimental results is also elucidated. To investigate the cellular flame characteristics induced by the D-T instability, highly-diluted hydrogen is considered as the fuel, for which its Lewis number is much less than unity.

2.1 Problem Formulation

In the experiments by Pitz and coworkers [15, 16, 19, 20] the opposed tubular flow configuration is designed such that fuel and oxidizer issue from a porous inner nozzle and contoured outer nozzle, respectively, and a tubular flame develops between the two nozzles. Readers are referred to [15, 16, 19, 20] for details of the experimental setup. An idealization of this configuration adopted in the present numerical study is such that fuel and oxidizer are assumed to issue from two infinitely-long concentric cylinders, forming a

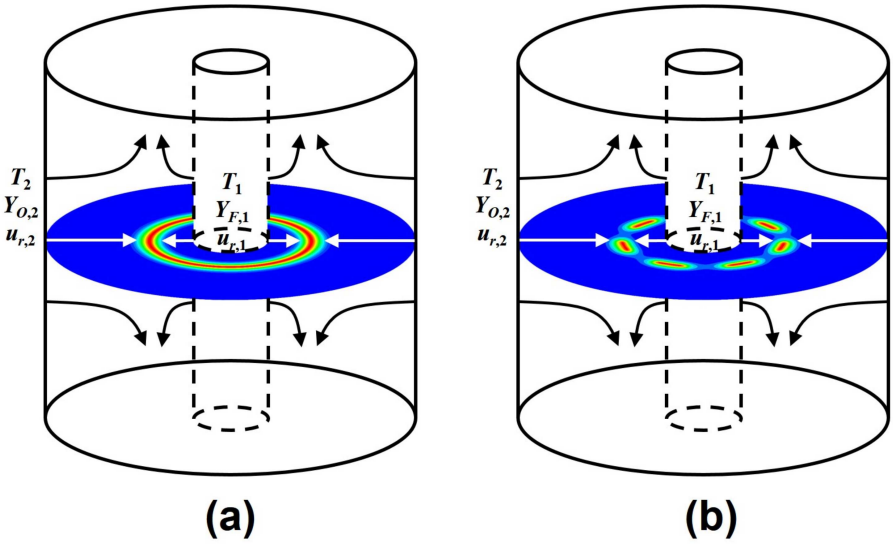

Figure 2.1: Schematic of (a) a noncellular tubular flame with large Damköhler number and (b) flame cells induced by the diffusive-thermal instability with small Damköhler number near the extinction limit.

tubular flame in between. To further simplify the problem, only variations in the plane of symmetry are considered as shown in Fig. 2.1. In particular, there is no axial variation in the solutions and the characteristics of non-premixed flame cell formation induced by the D-T instability in the $r-\theta$ plane are elucidated. Therefore, these effects are investigated without performing expensive 3-D simulations.

2.1.1 1-D Axisymmetric Tubular Flames

Prior to performing 2-D simulations of non-premixed tubular flames, the extinction characteristics of 1-D steady opposed non-premixed tubular flames are investigated and compared with previous experimental and numerical results. For this purpose, a 1-D axisymmetric model of opposed tubular flames, similar to the models for opposed counterflow flames [4, 13, 21, 84], is adopted:

$$\widetilde{\rho}\widetilde{u}_r\frac{d}{d\widetilde{r}}\begin{pmatrix}\widetilde{c}_p\widetilde{T}\\ \widetilde{Y}_F\\ \widetilde{Y}_O\end{pmatrix}=\frac{1}{\widetilde{r}}\frac{d}{d\widetilde{r}}\left(\widetilde{r}\frac{d}{d\widetilde{r}}\right)\begin{pmatrix}\widetilde{\lambda}\widetilde{T}\\ \widetilde{\rho}\widetilde{D}_F\widetilde{Y}_F\\ \widetilde{\rho}\widetilde{D}_O\widetilde{Y}_O\end{pmatrix}+\widetilde{B}\widetilde{Y}_F\widetilde{Y}_O e^{-\widetilde{E}/\widetilde{R}\widetilde{T}}\begin{pmatrix}\widetilde{\dot{Q}}\\ -\alpha_F\\ -\alpha_O\end{pmatrix}, \qquad (2.1)$$

where $\widetilde{T}$, $\widetilde{Y}_F$, and $\widetilde{Y}_O$ are the dimensional temperature, fuel mass fraction, and oxidizer mass fraction, respectively, with the density, $\widetilde{\rho}$, radial velocity, $\widetilde{u}_r$, specific heat, $\widetilde{c}_p$, thermal conductivity, $\widetilde{\lambda}$, fuel diffusivity, $\widetilde{D}_F$, oxidizer diffusivity, $\widetilde{D}_O$, pre-exponential factor, $\widetilde{B}$, activation energy, $\widetilde{E}$, universal gas constant, $\widetilde{R}$, heat release rate, $\widetilde{\dot{Q}}$, stoichiometric coefficients, α_F and α_O, and independent variable, $\widetilde{r}$, denoting the radial direction.

In this chapter, the D-T instability is numerically investigated by adopting the constant density model not only because it is common practice in many previous studies [4, 13, 21, 24, 84], but also because the density variation or thermal expansion has a minor effect on the D-T instability of non-premixed flames compared to that of premixed flames as found in [14]. Assuming that there is no density variation in the flow, the radial velocity $\widetilde{u}_r$ is analytically given by [85]:

$$\widetilde{u}_r(\widetilde{r}) = \begin{cases} \widetilde{u}_{r,1}\frac{\widetilde{r}_1}{\widetilde{r}}\sin\left(\frac{\widetilde{u}_{r,2}}{\widetilde{u}_{r,1}}\frac{\widetilde{r}_2}{\widetilde{r}_1}\sqrt{\frac{Q}{4}}\left(\frac{\widetilde{r}}{\widetilde{r}_2}\right)^2 + \frac{\pi}{2} - \frac{\widetilde{u}_{r,2}}{\widetilde{u}_{r,1}}\frac{\widetilde{r}_1}{\widetilde{r}_2}\sqrt{\frac{Q}{4}}\right) & : \widetilde{r}_1 \le \widetilde{r} < \widetilde{r}_s, \\ \widetilde{u}_{r,2}\frac{\widetilde{r}_2}{\widetilde{r}}\sin\left(\sqrt{\frac{Q}{4}}\left(\frac{\widetilde{r}}{\widetilde{r}_2}\right)^2 + \frac{\pi}{2} - \sqrt{\frac{Q}{4}}\right) & : \widetilde{r}_s \le \widetilde{r} \le \widetilde{r}_2, \end{cases} \tag{2.2}$$

where $\widetilde{r}_s$ and Q denotes the location of the stagnation plane and pressure eigenvalue, respectively:

$$\widetilde{r}_s = \widetilde{r}_2\left[1 - \frac{(\widetilde{r}_2/\widetilde{r}_1 - \widetilde{r}_1/\widetilde{r}_2)}{(\widetilde{r}_2/\widetilde{r}_1 - \widetilde{u}_{r,1}/\widetilde{u}_{r,2})}\right]^{1/2}, \tag{2.3}$$

$$\sqrt{Q} = \pi\left(\frac{\widetilde{r}_2/\widetilde{r}_1 - \widetilde{u}_{r,1}/\widetilde{u}_{r,2}}{\widetilde{r}_2/\widetilde{r}_1 - \widetilde{r}_1/\widetilde{r}_2}\right). \tag{2.4}$$

Note that the subscripts 1 and 2 denote the fuel and oxidizer inlets, respectively. The 1-D governing equations are subject to Dirichlet boundary conditions at the fuel and oxidizer inlets:

$$\begin{cases} \widetilde{T} = \widetilde{T}_1,\ \widetilde{Y}_F = \widetilde{Y}_{F,1},\ \widetilde{Y}_O = 0,\ \widetilde{u}_r = \widetilde{u}_{r,1}, & \text{at } \widetilde{r} = \widetilde{r}_1, \\ \widetilde{T} = \widetilde{T}_2,\ \widetilde{Y}_F = 0,\ \widetilde{Y}_O = \widetilde{Y}_{O,2},\ \widetilde{u}_r = \widetilde{u}_{r,2}, & \text{at } \widetilde{r} = \widetilde{r}_2. \end{cases} \tag{2.5}$$

By normalizing the dimensional variables with appropriate reference values, i.e. $r = \widetilde{r}/\sqrt{\widetilde{\lambda}/\widetilde{\rho}\widetilde{c}_p\widetilde{\kappa}}$, $u_r = \widetilde{u}_r/\sqrt{\widetilde{\kappa}\widetilde{\lambda}/\widetilde{\rho}\widetilde{c}_p}$, $T = \widetilde{T}/\widetilde{T}_{\text{ref}}$, $Y_F = \widetilde{Y}_F/\widetilde{Y}_{F,1}$, and $Y_O = \widetilde{Y}_O/\widetilde{Y}_{O,2}$, Eq. (2.1) can be written in non-dimensional form:

$$u_r\frac{d}{dr}\begin{pmatrix} T \\ Y_F \\ Y_O \end{pmatrix} = \frac{1}{r}\frac{d}{dr}\left(r\frac{d}{dr}\right)\begin{pmatrix} T \\ Y_F/Le_F \\ Y_O/Le_O \end{pmatrix} + DaY_FY_Oe^{-T_a/T}\begin{pmatrix} q \\ -\alpha_F\widetilde{Y}_{O,2} \\ -\alpha_O\widetilde{Y}_{F,1} \end{pmatrix}, \tag{2.6}$$

where Le_F ($= \widetilde{\lambda}/\widetilde{\rho}\widetilde{c}_p\widetilde{D}_F$) is the fuel Lewis number, Le_O ($= \widetilde{\lambda}/\widetilde{\rho}\widetilde{c}_p\widetilde{D}_O$) is the oxidizer Lewis number, Da ($= \widetilde{B}/\widetilde{\rho}\widetilde{\kappa}$) is the Damköhler number, q ($= \widetilde{Y}_{F,1}\widetilde{Y}_{O,2}\widetilde{\dot{Q}}/\widetilde{c}_p\widetilde{T}_{\rm ref}$) is the heat release rate, and T_a ($= \widetilde{E}/\widetilde{R}\widetilde{T}_{\rm ref}$) is the activation temperature. Note that $\widetilde{\kappa}$ is the reference stretch rate and is inversely proportional to Da by definition. The corresponding non-dimensional boundary conditions at the two inlets are given by:

$$\begin{cases} T = T_1,\ Y_F = 1,\ Y_O = 0,\ u_r = u_{r,1}, & \text{at}\ \ r = r_1, \\ T = T_2,\ Y_F = 0,\ Y_O = 1,\ u_r = u_{r,2}, & \text{at}\ \ r = r_2. \end{cases} \tag{2.7}$$

To simulate cases similar to the experiments of opposed hydrogen/air non-premixed tubular flames [15, 19], we specify $q = 1.2$, $T_a = 8$, $Le_F = 0.3$, $Le_O = 1.0$, $\alpha_F\widetilde{Y}_{O,2} = 1.0$, $\alpha_O\widetilde{Y}_{F,1} = 0.36$, $r_1 = 20$, $r_2 = 100$, and $T_1 = T_2 = 0.2$. Note that these values represent non-premixed tubular flames formed by opposing nitrogen-diluted hydrogen and air flows [13, 84], rendering the maximum flame temperature, $T_{\rm max}$, to be approximately unity near extinction. If $T_1 = T_2 = 0.2$ is assumed to be 300 K, $T_{\rm max} \approx 1$ near extinction represents approximately 1500 K [13].

For a specific stagnation plane, only the ratio of $u_{r,1}$ to $u_{r,2}$ can be determined from Eq. 2.3. To specify each value of $u_{r,1}$ and $u_{r,2}$, another condition is required. For this purpose and for fair comparison between tubular flames with different stagnation planes, we adopt an identical stretch rate, κ, defined as $\kappa = -(u_{r,2}/r_2)\sqrt{Q}$ at the stagnation plane [18, 85]. Since the flame is located close to the stagnation plane for our choice of parameters, it is reasonable to adopt a constant κ at the stagnation plane as the condition for determining $u_{r,1}$ and $u_{r,2}$. For all of the 1-D and 2-D simulations, the same stretch rate, $\kappa = 0.03927$, is used, which is evaluated from $u_{r,1} = -u_{r,2} = 1.0$. Once the stagnation plane is specified, then $u_{r,1}$ and $u_{r,2}$ are uniquely determined from the stretch rate of 0.03927. Note that the identical stretch rate is used for all of the different tubular flames and hence, the effect of stretch rate on the flames is solely incorporated in the Da of the governing equations (see Eq. 2.6).

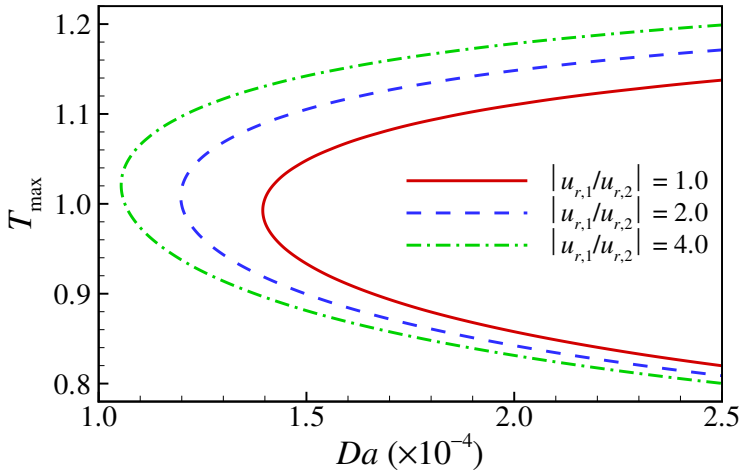

Figure 2.2: The maximum flame temperature, $T_{\max}$, as a function of Damköhler number, Da, for three different $|u_{r,1}/u_{r,2}|$ of 1.0, 2.0, and 4.0.

2.1.2 1-D Steady Solutions

Figure 2.2 shows the so-called "C-curve" of $T_{\max}$ as functions of Da and the ratio of $u_{r,1}$ to $u_{r,2}$. The C-curves are obtained by solving Eq. 2.6 using the Newton-Raphson method with a simple continuation algorithm [84]. The upper branch of the C-curves represents the intensely-burning state and the lower branch is unstable and physically unrealistic. Note that the corresponding parameters, $(u_{r,1}, u_{r,2}, r_s)$, for the three different cases are $(1.0, -1.0, 44.72)$, $(1.7143, -0.8571, 56.06)$, and $(2.6667, -0.6667, 68.31)$, respectively. The extinction Damköhler number, Da_E, for the 1-D tubular flames with $|u_{r,1}/u_{r,2}| =$ 1.0, 2.0, and 4.0 are found to be 13950, 11977, and 10542, respectively.

Two points are noted from the figure. First, Da_E decreases with increasing $|u_{r,1}/u_{r,2}|$ and r_s. Second, for a given Da, $T_{\max}$ also increases with increasing $|u_{r,1}/u_{r,2}|$ and r_s. These results are consistent with those found in a previous 1-D numerical study of opposed tubular flames [18], i.e. "negatively-curved" non-premixed tubular flames become weaker as the stretch rate is increased when the fuel Lewis number is less than unity. Note that a negatively-curved flame is formed in this configuration where fuel and oxidizer issue from the inner and outer nozzles, respectively, as in this chapter. The negative curvature weakens the preferential diffusion of fuel with small Le_F and, as such, the tubular flame becomes more vulnerable to stretch rate ($\sim 1/Da$) as r_s becomes smaller. More generally,

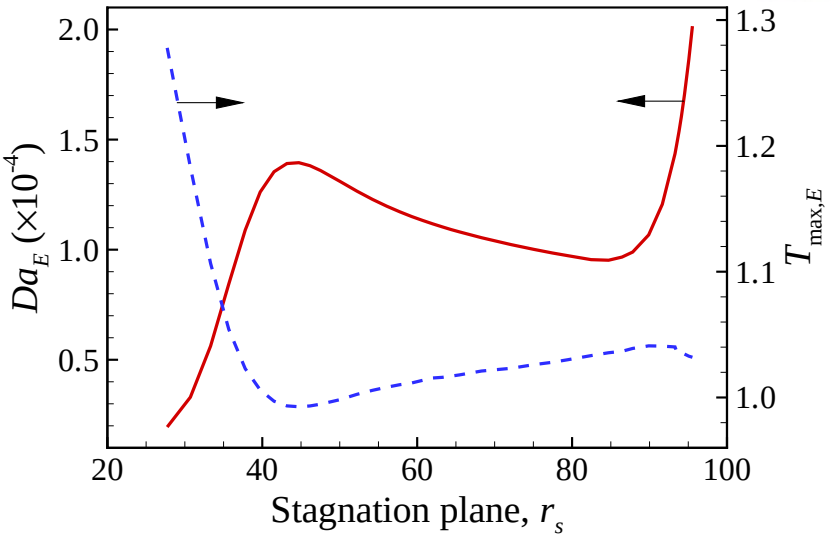

Figure 2.3: The extinction Damköhler number, Da_E, and maximum flame temperature, $T_{\max,E}$, at the extinction point as a function of the stagnation plane location, r_s.

curvature plays a critical role in the extinction of negatively-curved non-premixed tubular flames when the fuel Lewis number is much less than unity and the flame radius becomes the order of the flame thickness [18].

To further quantify the effect of curvature on the extinction of steady tubular flames, the variation of Da_E and $T_{\max,E}$ as a function of r_s is shown in Fig. 2.3. $T_{\max,E}$ denotes the maximum flame temperature at the extinction point. It is readily observed from the figure that if the flame lies in the middle of the domain (i.e. $40 \lesssim r_s \lesssim 90$), Da_E decreases and $T_{\max,E}$ increases with increasing r_s as can be expected from Fig. 2.2 and the previous result [18].

On the contrary, as the tubular flame approaches the inner/outer cylinder ($r_s \lesssim 40$ or $r_s \gtrsim 90$), Da_E decreases/increases and $T_{\max,E}$ increases/decreases. Near the two boundaries, the steady solutions are directly affected by the Dirichlet boundary conditions; when the tubular flame lies very close to the inner cylinder, the fuel mass flux into the flame becomes significantly larger compared to the mass flux into the flame in the center of the domain. Since a highly-diluted hydrogen jet is assumed to issue from the inner cylinder in this chapter, the flame becomes stronger despite the weakened preferential diffusion of the fuel due to the small r_s. This results in smaller Da_E and larger $T_{\max,E}$

for flames lying near the inner cylinder. However, when the tubular flame is formed very close to the outer cylinder, the oxidizer mass flux into the flame increases and the flame becomes weaker, subsequently leading to larger Da_E and smaller $T_{\max,E}$. In this chapter, therefore, only tubular flames formed in the center of the domain ($40 \lesssim r_s \lesssim 90$) are investigated, where such artefacts of the Dirichlet boundary conditions on the solution are minimal.

2.1.3 2-D Tubular Flames

To investigate the characteristics of the D-T instability of non-premixed opposed tubular flames, it is common practice to extend the governing equations describing the 1-D steady tubular flames to time-dependent partial differential equations including variations in the azimuthal direction, θ [4, 13, 21, 84]:

$$\begin{aligned}\left(\frac{\partial}{\partial t}+u_r\frac{\partial}{\partial r}\right)\begin{pmatrix}T\\Y_F\\Y_O\end{pmatrix} = \left(\frac{1}{r}\frac{\partial}{\partial r}\left(r\frac{\partial}{\partial r}\right)+\frac{1}{r^2}\frac{\partial^2}{\partial\theta^2}\right)\begin{pmatrix}T\\Y_F/Le_F\\Y_O/Le_O\end{pmatrix} \\ +DaY_FY_Oe^{-T_a/T}\begin{pmatrix}q\\-\alpha_F\widetilde{Y}_{O,2}\\-\alpha_O\widetilde{Y}_{F,1}\end{pmatrix},\end{aligned} \tag{2.8}$$

which are also subject to the same boundary conditions of Eq. 2.7 in the $r-$direction as in the 1-D problems. Periodic boundary conditions are imposed in the $\theta-$direction. Note that the dimensional time, $\widetilde{t}$, is normalized as $t = \widetilde{t}\widetilde{\kappa}$. The 2-D direct numerical simulations of tubular flames are performed using a six-stage fourth-order explicit Runge-Kutta method for time integration and an eighth-order central finite-difference scheme for evaluating spatial derivatives [86, 87] as in [84]. The message passing interface (MPI) is used for scalable parallelism. After a series of grid convergence tests, a uniform grid system of 400 × 1200 is adopted to discretize the $r-$ and $\theta-$directions for $|u_{r,1}/u_{r,2}| =$ 1.0 and 2.0, while a grid system of 800 × 2400 is used for for $|u_{r,1}/u_{r,2}| = 4.0$. A timestep, Δt, of 0.001 or 0.004 is required for accurate time integration.

For 2-D simulations, two different initial conditions (IC) are adopted to investigate

the effects of small ($\sim O(\varepsilon)$) and large ($\sim O(1)$) amplitude disturbances on the formation of flame cells. The first IC is constructed from the 1-D steady solution of a tubular flame at a given Da, and is replicated along the $\theta-$direction. A small sinusoidal perturbation of temperature ($\sim O(\varepsilon)$) is superimposed on the steady solution field:

$$T_{\text{2-D,init}}(r,\theta) = T_{\text{1-D}}(r) + \varepsilon \cdot \sin\theta \cdot (T_{\text{1-D}}(r) - T_1) \quad : 0 \le \theta < 2\pi, \tag{2.9}$$

where $T_{\text{1-D}}(r)$ represents the 1-D steady temperature solution given by Eq. 2.6. The perturbation amplitude, ε, of 10^{-5} is selected through a series of 2-D simulations from which it is confirmed that there is no change in the number of flame cells and extinction behavior for $\varepsilon \le 10^{-5}$. Henceforth, this initial condition is referred to as the "perturbed IC".

The second IC is devised by combining intensely-burning and frozen-flow solutions through a smooth transition using the hyperbolic tangent function, representing $\sim O(1)$ disturbance [13, 84]:

$$\begin{aligned}\mathbf{x}_{\text{2-D,init}}(r,\theta) = \mathbf{x}_{\text{1-D,F}}(r) + 1 \cdot &\left[\left(\tanh(\theta-\theta_1) - \tanh(\theta-\theta_2)\right)/\sigma\right] \\ &\cdot \left(\mathbf{x}_{\text{1-D,B}}(r) - \mathbf{x}_{\text{1-D,F}}(r)\right)/2 \quad : 0 \le \theta < 2\pi,\end{aligned} \tag{2.10}$$

where $\mathbf{x}$ is the solution vector including T, Y_F, and Y_O; $\theta_1 = 0.5\pi$; $\theta_2 = 1.5\pi$; $\sigma = 0.1\pi$. The subscripts B and F represent intensely-burning and frozen-flow solutions. Note that this type of initial condition was adopted in [13,84] to investigate the edge flame dynamics near the extinction limit. Henceforth, it is referred to as the "C-shaped IC". From the C-shaped IC, a "horseshoe-shaped" cellular flame is formed at relatively-large Da, similar to a large flame cell induced by local quenching in previous experimental studies [15, 16]. Starting from the horseshoe-shaped cellular flame the dynamics of flame cell formation is investigated by gradually reducing Da, similar to the experimentBuckmaster02al procedure in [15, 16]. Figure 2.4 shows isocontours of temperature for the two different ICs. Note that the perturbation amplitude in the perturbed IC is small enough that it cannot be clearly observed in the figure.

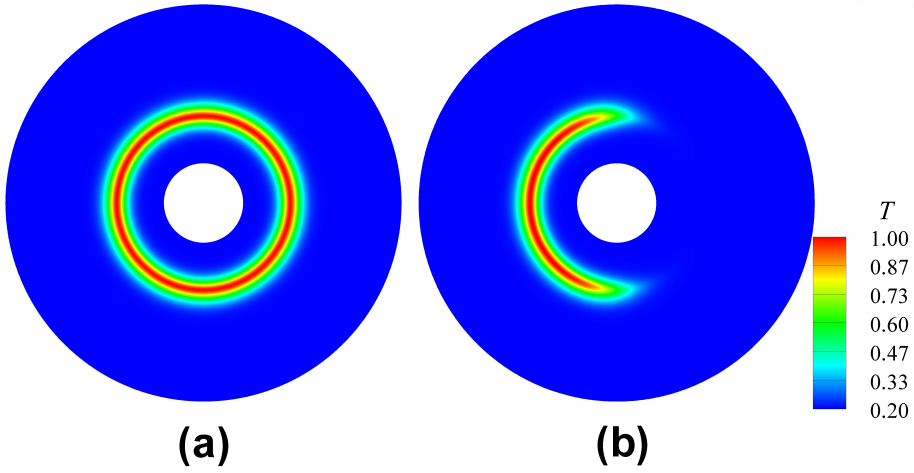

Figure 2.4: Initial temperature fields for 2-D simulations of opposed tubular flames: (a) the perturbed IC and (b) the C-shaped IC.

2.2 Stability Analysis

Prior to performing 2-D direct numerical simulations, a linear stability analysis of opposed non-premixed tubular flames near extinction is conducted to gain insight into the cellular instability characteristics as in [13, 21]. For the stability analysis, the steady solution of the 1-D tubular flame, denoted by an overbar, is perturbed with small harmonic perturbations:

$$T = \bar{T}(r)+\epsilon T'(r)e^{ik\theta+\lambda t},\ Y_F = \bar{Y}_F(r)+\epsilon Y'_F(r)e^{ik\theta+\lambda t},\ Y_O = \bar{Y}_O(r)+\epsilon Y'_O(r)e^{ik\theta+\lambda t}, \quad (2.11)$$

where λ is a complex number whose the real part, $\mathrm{Re}(\lambda)$, represents the growth rate, k is the wavenumber, and ϵ is the small perturbation amplitude similar to ε in the perturbed IC. Substituting Eq. 2.11 into Eq. 2.8 and linearizing the equation yields:

$$\begin{aligned}\frac{1}{r}\frac{d}{dr}\left(r\frac{d}{dr}\right)\begin{pmatrix} T' \\ Y'_F/Le_F \\ Y'_O/Le_O \end{pmatrix} - u_r\frac{d}{dr}\begin{pmatrix} T' \\ Y'_F \\ Y'_O \end{pmatrix} - \begin{pmatrix} k^2/r^2+\lambda \\ k^2/r^2Le_F+\lambda \\ k^2/r^2Le_O+\lambda \end{pmatrix}\begin{pmatrix} T' \\ Y'_F \\ Y'_O \end{pmatrix} \\ +Dae^{-T_a/\bar{T}}\left(\bar{Y}_O Y'_F+\bar{Y}_F Y'_O+\frac{\bar{Y}_F\bar{Y}_O}{\bar{T}^2}T_a T'\right)\begin{pmatrix} q \\ -\alpha_F\widetilde{Y}_{O,2} \\ -\alpha_O\widetilde{Y}_{F,1} \end{pmatrix} = 0,\end{aligned} \quad (2.12)$$

where the boundary conditions are $T' = Y_F' = Y_O' = 0$ at both $r = r_1$ and $r = r_2$. An eigenvalue problem of $(\mathbf{A} - \lambda\mathbf{B})\mathbf{x}' = 0$ is then obtained by discretizing Eq. 2.12, where $\mathbf{x}'$ is the discretized solution vector including T', Y_F', and Y_O'.

By solving the eigenvalue problem for fixed k and Da, the largest growth rate, λ_R, can be obtained among many $\mathrm{Re}(\lambda)$. By finding λ_R for different k and Da values, the variation of λ_R as functions of k and Da is ultimately obtained. Note that if all λ_R exhibit negative values over the entire range of k for a given Da, small perturbations would decay in time and, as such, no flame instability occurs at that Da. However, if at least one λ_R exhibits a positive value over a certain range of k, even infinitesimally-small disturbances would grow in time, ultimately leading to the occurrence of flame instability manifested by the formation of flame cells.

Figure 2.5 shows the largest growth rate, λ_R, as a function of wavenumber for three different $|u_{r,1}/u_{r,2}|$ with several Damköhler numbers near their extinction limits. Several points are noted from the figure. First, it is readily observed that for $|u_{r,1}/u_{r,2}| = 1.0$, 2.0, and 4.0, positive λ_R first appears at approximately $Da_C = 14412$, 12360, and 10865, respectively and the corresponding k is found to be 7.0, 9.0, and 11.0. Henceforth, Da_C denotes the critical Damköhler number at which the first positive λ_R appears, and hence, the D-T instability occurs. This result implies that the D-T instability of opposed non-premixed tubular flames can occur over the range, $Da_E \leq Da \leq Da_C$, near the 1-D extinction limit, consistent with previous theoretical and numerical studies of non-premixed counterflow flames [11–13].

Second, the wavenumber, $k_{\max}$, at which λ_R attains its maximum value for a given Da, slightly increases as Da decreases from Da_C to Da_E; for $|u_{r,1}/u_{r,2}| = 1.0$, 2.0, and 4.0, $k_{\max} = 7.0 \rightarrow 7.8$, $9.0 \rightarrow 9.9$, and $11.0 \rightarrow 12.1$, respectively, as $Da = Da_C \rightarrow Da_E$. Furthermore, it is also observed that the maximum λ_R and the range of k exhibiting positive λ_R increase with decreasing Da. This implies that opposed non-premixed tubular flames are more vulnerable to flame instability at smaller Da as can be expected. It can also be expected that the D-T instability can occur more rapidly in time at smaller Da near Da_E due to its relatively-large λ_R there. Note also that if the wavenumber is related to the number of flame cells, N_{cell}, induced by the D-T instability, it can be expected

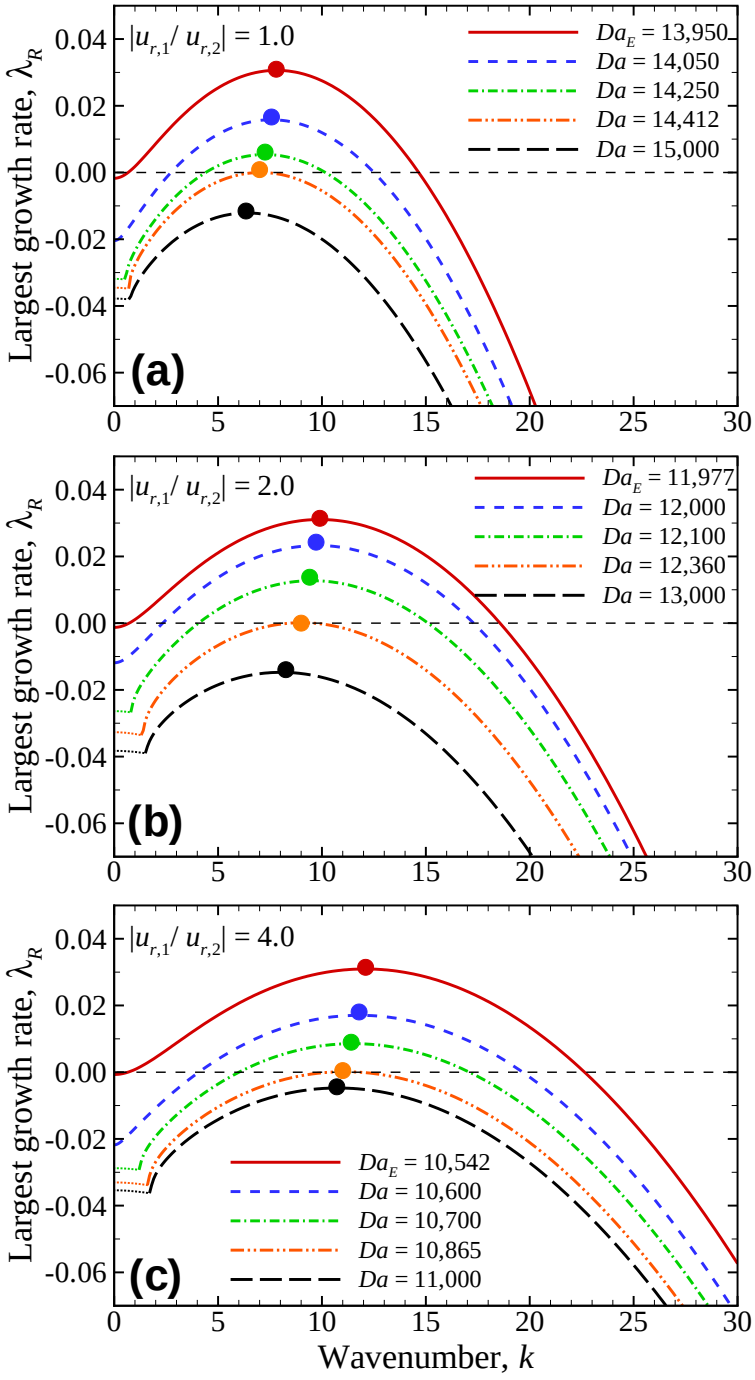

Figure 2.5: The largest growth rate, λ_R, as functions of the wavenumber, k, and the Damköhler number, Da, from the linear stability analysis for different $|u_{r,1}/u_{r,2}|$ of (a) 1.0, (b) 2.0, and (c) 4.0. Thick segments and thin dotted segments represent the imaginary part of $\lambda = 0$ and $\neq 0$, respectively. The solid circles represent the points of $\lambda_{R,\max}$ and $k_{\max}$.

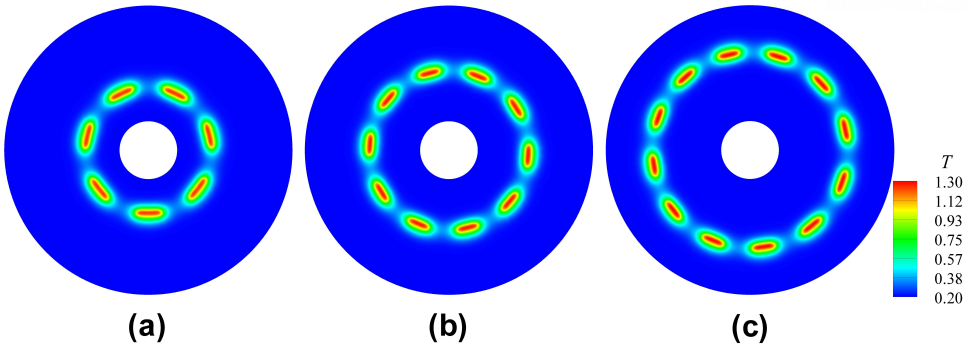

Figure 2.6: Temperature isocontours of steady flame cells from the perturbed IC for different $|u_{r,1}/u_{r,2}|$ of (a) 1.0, (b) 2.0, and (c) 4.0 at their Da_E = 13950, 11977, and 10542, respectively.

that N_{cell} increases with increasing $|u_{r,1}/u_{r,2}|$ and r_s, which is further discussed in the following section.

2.3 The Diffusive-thermal Instability with the Perturbed IC

In this section, 2-D direct numerical simulations of tubular flames are performed to investigate the characteristics of the D-T instability of tubular flames with the perturbed IC. As mentioned above, the perturbed IC is used to compare the results of the numerical simulations based on the full nonlinear equations (Eq. 2.8) with those based on the linearized equations (Eq. 2.12).

Figure 2.6 shows the temperature isocontours of flame cells induced by the D-T instability for three different values of $|u_{r,1}/u_{r,2}|$ at their corresponding Da_E, obtained by numerically integrating Eq. 2.8 with the perturbed IC of Eq. 2.9. As shown in the figure, N_{cell} for $|u_{r,1}/u_{r,2}|$ = 1.0, 2.0, and 4.0 is found to be 7, 10, and 12, respectively, quite similar to the values of $k_{\max}$ obtained from the linear stability analysis (see Fig. 2.5): for $|u_{r,1}/u_{r,2}|$ = 1.0, 2.0, and 4.0, $k_{\max}$ is 7.8, 9.9, and 12.1 at their Da_E, respectively. From these results, it can be conjectured that the number of flame cells induced by the D-T instability in the 2-D simulations is equal to an integer close to $k_{\max}$.

The dynamics of flame cell formation is identified by examining sequential snapshots

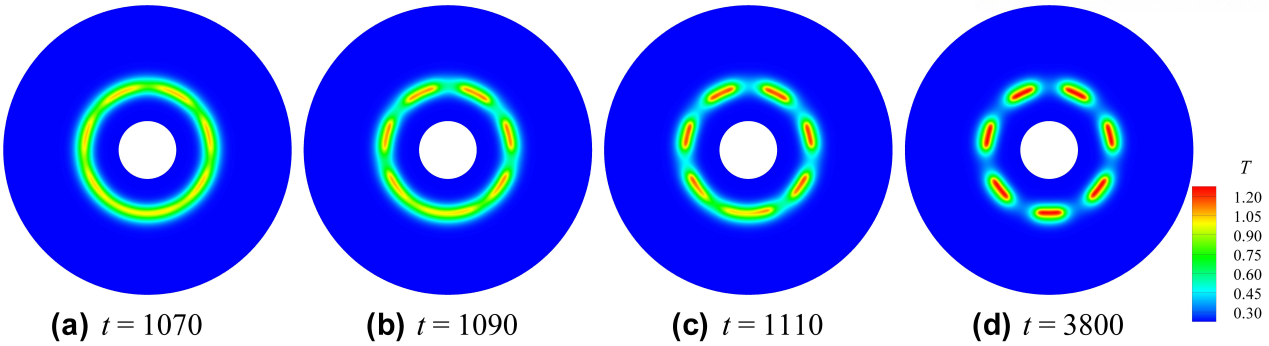

Figure 2.7: Temporal evolution of flame cells from the perturbed IC for $|u_{r,1}/u_{r,2}| = 1.0$ at $Da_E = 13950$. From left to right, t = (a) 1070, (b) 1090, (c) 1110, and (d) 3800.

in time of the temperature field for $|u_{r,1}/u_{r,2}| = 1.0$ at $Da = 13950$ as shown in Fig. 2.7. Small initial perturbations continue to grow in time due to the D-T instability, inducing alternating weak and strong reaction regions (Fig. 2.7a). This leads to local extinction at the weak reaction regions between two strong reaction regions, forming small flame cells (Fig. 2.7b and c). Ultimately, a finite number of steady flame cells are formed as shown in Fig. 2.7d. This sequential dynamics of flame cell formation is qualitatively similar to that observed in non-premixed counterflow flames [21].

To further identify the general characteristics of the D-T instability by the perturbed IC, the variation of $T_{\max}$ and N_{cell} as a function of Da is shown in Fig. 2.8 for three different values of $|u_{r,1}/u_{r,2}|$. For the purpose of comparison, $T_{\max}$ from the 1-D solutions and $k_{\max}$ from the linear stability analysis are also shown in the figure. Note that since the perturbed ICs are based on the 1-D steady solutions, 2-D simulations are performed only for $Da \geq Da_E$. Several points are to be noted from the figure. First, for $|u_{r,1}/u_{r,2}|$ = 1.0, 2.0, and 4.0, the critical Damköhler number with the perturbed IC at the onset of the D-T instability, $Da_{C,\text{PI}}$, is approximately 14350, 12330, and 10830, respectively, which are slightly smaller than the corresponding Da_C from the linear stability analysis: i.e. Da_C = 14412, 12360, and 10865. The corresponding number of flame cells in the 2-D simulations is 7, 9, and 11, which is quite similar to the correspond $k_{\max}$ from the stability analysis. Therefore, the linear stability analysis is able to predict the characteristics of non-premixed tubular flame instability including the number of flame cells and the Damköhler number at the onset of cellular flame instability with reasonable accuracy.

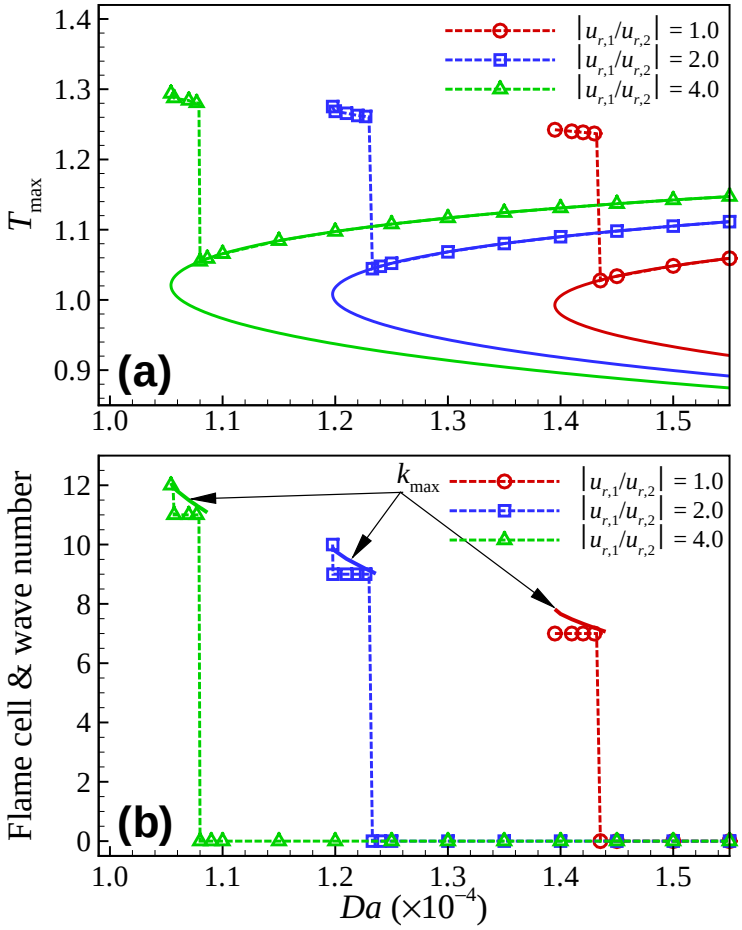

Figure 2.8: The variation of (a) $T_{\max}$ and (b) the number of flame cells as a function of Da from the perturbed IC for $|u_{r,1}/u_{r,2}| = 1.0$, 2.0, and 4.0. The solid lines in (a) and (b) represent $T_{\max}$ of 1-D solutions and $k_{\max}$, respectively.

Second, when the D-T instability occurs, $T_{\max}$ of the flame cells bifurcates from that of the corresponding 1-D steady tubular flame and exhibits a much larger value. This is primarily the result of focusing effects, that is, the fuel-mass diffusion into the edge of the flame cells strengthens overall reaction and hence, the flame temperature near the edges increases significantly compared to the temperature of the corresponding 1-D steady tubular flame as shown in Figs. 2.6 and 2.7.

Third, it is also readily observed from the figure that $T_{\max}$ of the flame cells continues to increase as Da decreases from $Da_{C,\mathrm{PI}}$ to Da_E. This is the result of the flame cell length, l_{cell}, decreasing with decreasing Da, and hence, the focusing effect of fuel-mass diffusion into the flame cell increases, resulting in the increase of $T_{\max}$ with decreasing Da. These results are also consistent with previous studies of the D-T instability of non-premixed counterflow flames [13]. In fact, l_{cell} decreases from 2.68 to $2.48 l_D$ when Da decreases from $Da_{C,\mathrm{PI}}$ to Da_E for $|u_{r,1}/u_{r,2}| = 1.0$, where l_D is the diffusion flame thickness of the corresponding 1-D tubular flame. Note that l_D is measured by the full-width-half-maximum (FWHM) temperature, which remains nearly identical regardless of Da near extinction. From a previous study of the D-T instability of planar diffusion flames [9,88], it was also reported that the characteristic flame cell length at the onset of the instability is in the range of $3 \sim 12 l_D$, which is similar to the results of the present study.

It is of interest to note that the slight discrepancies between the 2-D simulations and the linear stability analysis may stem from the inherent differences between the nonlinear governing equations of Eq. 2.8 for the 2-D simulations and the linearized equations of Eq. 2.12 for the stability analysis. The discrepancies may also be attributed to the slight difference between the perturbed IC for the 2-D simulations and the perturbed variables in Eq. 2.11 for the stability analysis. The numerical dissipation of the solutions in the 2-D simulations may also be another reason for the discrepancies.

2.4 The Diffusive-thermal Instability with the C-shaped IC

As discussed in Section 2.3, the prediction of the linear stability analysis shows good agreement with the characteristics of the D-T instability of 2-D tubular flames with the perturbed IC in terms of Da_C and the resultant N_{cell}. In experiments, however, a noncellular tubular flame is first formed between the two nozzles with low stretch rate and subsequently, the formation of flame cells is observed by incrementally increasing the stretch rate [15]. From a noncellular tubular flame, a horseshoe-shaped cellular flame first appears by local extinction at intermediate stretch rate and subsequently, divides into several flame cells as the stretch rate is further increased (see Fig. 6 in [15]).

In an attempt to replicate this experimental procedure, a horseshoe-shaped cellular flame is first generated from the C-shaped IC by reducing Da, similar to the increase in stretch rate in the experiments. The detailed simulation procedure is as follows: to locate the onset of a horseshoe-shaped cellular flame, a new simulation is started with the C-shaped IC by gradually decreasing Da until a horseshoe-shaped cellular flame is established. For the case with $|u_{r,1}/u_{r,2}| = 1.0$, for instance, the edge flames develop from the C-shaped IC, ultimately merging into a noncellular tubular flame for $Da > 18900$. At $Da = 18900$, however, the two edges propagate towards each other but do not merge. Rather they form a horseshoe-shaped cellular flame as shown in Fig. 2.9. Once a solution exhibiting a horseshoe-shaped flame at a specific Da is obtained, successive simulations at successively smaller Da are restarted from each of the previous steady solutions, resetting the simulation time to the beginning upon restarting. For $|u_{r,1}/u_{r,2}| = 1.0$, the horseshoe-shaped cellular flame divides into five flame cells at approximately $Da = 14600$. From the 2-D simulations performed using this procedure three different types of flames are observed for different values of $|u_{r,1}/u_{r,2}|$ within the entire range of Da as shown in Fig. 2.10: i.e. a noncellular tubular flame at relatively-large Da (Fig. 2.10a), a horseshoe-shaped cellular flame at intermediate Da (Fig. 2.10b), and several flame cells at relatively-small Da (Figs. 2.10c and d). This result is qualitatively similar to

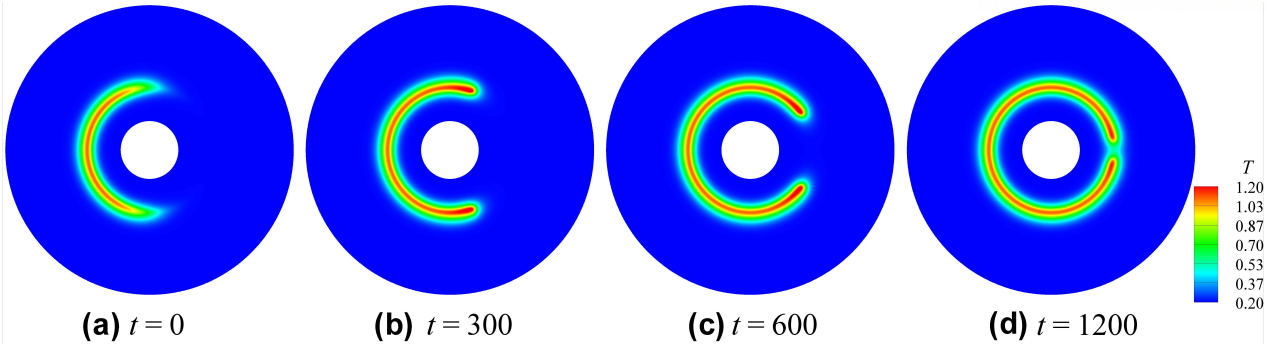

Figure 2.9: Temporal evolution of the horseshoe-shaped cellular flame from the C-shaped IC at $Da = 18900$ for $|u_{r,1}/u_{r,2}| = 1.0$. From left to right, $t =$ (a) 0, (b) 300, (c) 600, and (d) 1200.

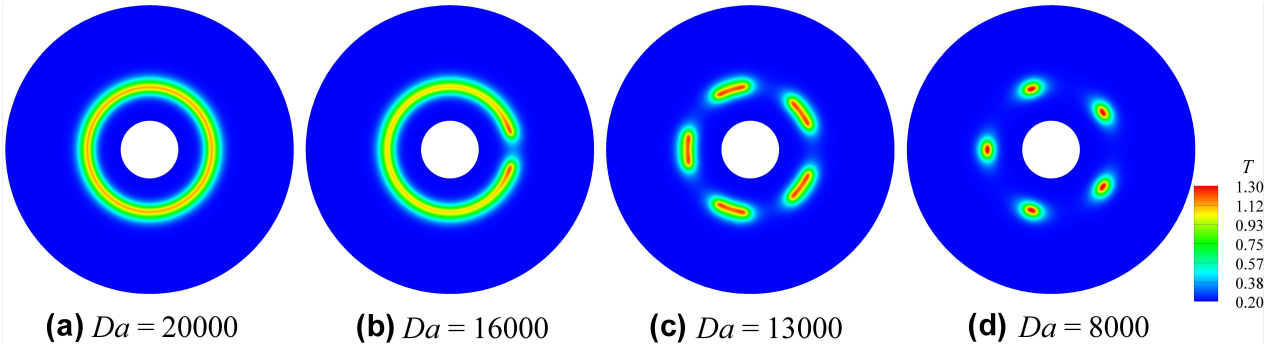

Figure 2.10: Temperature isocontours of steady flame cells from the C-shaped IC for $|u_{r,1}/u_{r,2}| = 1.0$ at $Da =$ (a) 20000, (b) 16000, (c) 13000, and (d) 8000.

the experimental result by Shopoff et al. [15] which identified the sequence of flame cell dynamics evolving from a noncellular flame to a horseshoe-shaped cellular flame to several flame cells with increasing stretch rate.

To further identify the characteristics of the D-T instability, the variation of $T_{\max}$ and N_{cell} as a function of Da for three different values of $|u_{r,1}/u_{r,2}|$ is shown in Fig. 2.11. Several points are noted from the figure. First, it is readily observed that the flame cellularity starts to occur at much larger Da than the corresponding critical Damköhler number, Da_C, from the stability analysis for all cases: i.e. for $|u_{r,1}/u_{r,2}| = 1.0$, 2.0, and 4.0, the horseshoe-shaped cellular flame first occurs at $Da = 18900$, 16300, and 14350, and the corresponding Da_C is 14412, 12360, and 10865, respectively. The implication is that the horseshoe-shaped cellular flame is induced not by small perturbations ($\sim O(\varepsilon)$)

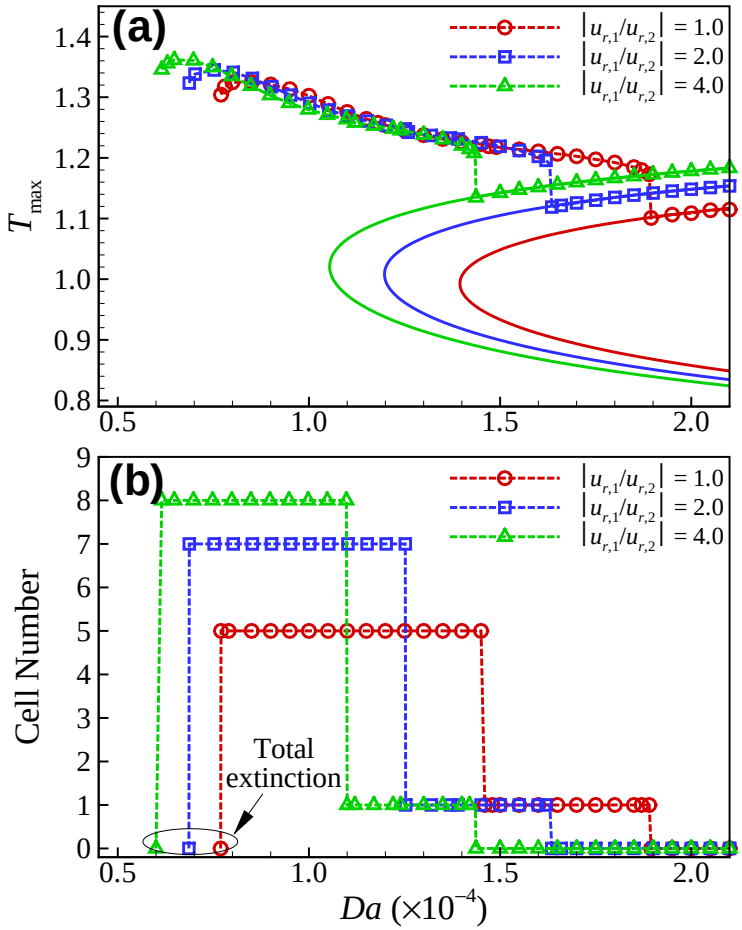

Figure 2.11: The variation of (a) the maximum flame temperature, $T_{\max}$, and (b) the number of flame cells as a function of Damköhler number, Da, from the C-shaped IC for $|u_{r,1}/u_{r,2}| = 1.0$, 2.0, and 4.0.

but by large amplitude disturbances ($\sim O(1)$). From the experimental perspective, it can be conjectured that inevitable asymmetry in the tubular flame experiments may induce locally-high stretch rate, leading to the local extinction of a noncellular tubular flame and the formation of a horseshoe-shaped cellular flame even at intermediate values of mean stretch rate.

Second, although the horseshoe-shaped cellular flame starts to occur at intermediate Da, the formation of several small flame cells induced by the D-T instability starts to occur at the critical Damköhler number with the C-shaped IC, $Da_{C,\mathrm{CI}}$, close to Da_C from the linear stability analysis: i.e. $Da_{C,\mathrm{CI}} = 14600$, 12520, and 10980 for $|u_{r,1}/u_{r,2}| = 1.0$, 2.0, and 4.0, respectively. In fact, the $Da_{C,\mathrm{CI}}$ values are slightly larger than the

corresponding Da_C from the linear stability analysis. This is due to the large amplitude disturbance ($\sim O(1)$) between the two edges of the horseshoe-shaped cellular flame which may induce the onset of flame cells at slightly larger Da than Da_C. This result also confirms that the linear stability analysis can predict Da_C for the 2-D simulations with both perturbed and C-shaped ICs with reasonable accuracy.

Third, however, the number of flame cells at $Da_{C,\mathrm{CI}}$ for $|u_{r,1}/u_{r,2}| = 1.0$, 2.0, and 4.0, is found to be 5, 7, and 8, respectively, which is smaller than that found from the linear stability analysis and the 2-D simulations with the perturbed IC. To identify the characteristics of N_{cell}, the dynamics of flame cell formation is examined as shown in Fig. 2.12. When the horseshoe-shaped cellular flame starts to divide into flame cells, the first local extinction occurs farther away from the flame edge (Figs. 2.12a and b) due to a relatively-large flame edge with strong reaction manifested by high temperature. As such, the flame cell length becomes larger compared to that found in the 2-D simulations with the perturbed IC (see Fig. 2.7). Following the first local extinction, another flame edge develops and subsequently, the second local extinction occurs (Figs. 2.12b and c), ultimately leading to the formation of five flame cells. These results imply that the number and size of flame cells are affected by the size and strength of the edge flames of the horseshoe-shaped cellular flame. From this perspective, the number of flame cells observed in experiments cannot be the same as that from the linear stability analysis because the flame cells in experiments are usually generated from the horseshoe-shaped cellular flame [15, 16].

Fourth, once the horseshoe-shaped cellular flame divides into several flame cells, the number of flame cells remains constant until global extinction occurs for all $|u_{r,1}/u_{r,2}|$ as shown in Fig. 2.11. In the 2-D simulations with the perturbed IC, N_{cell} changes according to $k_{\max}$ as discussed above. For the cases with the C-shaped IC, however, the flame cells generated from the horseshoe-shaped cellular flame are strong enough to survive small Da and hence, no further local extinction occurs within the flame cells up to the point of global extinction.

Fifth, it is also readily observed from the figure that the flame cells can survive beyond the 1-D extinction Damköhler number, Da_E; i.e. for $|u_{r,1}/u_{r,2}| = 1.0$, 2.0, and 4.0 the

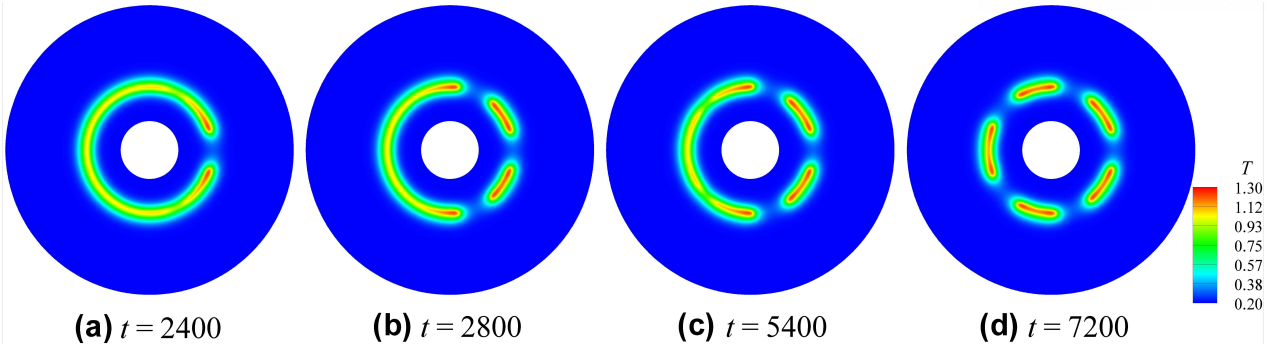

Figure 2.12: Temporal evolution of flame cells from a horseshoe-shaped cellular flame at $Da = 14600$ for $|u_{r,1}/u_{r,2}| = 1.0$. From left to right, $t =$ (a) 2400, (b) 2800, (c) 5400, and (d) 7200.

extinction Damköhler number for the global extinction of the flame cells, $Da_{E,2D}$, is found to be 7690, 6860, and 6000, respectively. In addition, $T_{\max}$ increases with decreasing Da, similar to the results with the perturbed IC. As Da decreases, the flame cell length, l_{cell}, is significantly reduced from 4.0 to $1.4l_D$ as shown in Fig. 2.10, leading to an enhanced focusing effect of fuel-mass diffusion into the flame cells, consequently increasing $T_{\max}$. This result is qualitatively consistent with previous studies of the D-T instability of non-premixed counterflow flames [13]. However, $T_{\max}$ decreases slightly with decreasing Da near the 2-D extinction Damköhler number, $Da_{E,2D}$. This is primarily attributed to incomplete reaction by small Damköhler number near the point of global extinction which becomes significant compared to the enhanced focusing effect of fuel-mass diffusion.

2.5 Dynamics of Flame Cell Formation - Displacement Speed Analysis

In this section, the dynamics of flame cell formation is further quantified by evaluating the propagation speed of the flame cell edges. The propagation speed of the flame edges is obtained by evaluating the displacement speed which measures the velocity of a scalar isocontour (e.g. the fuel mass fraction) relative to the local flow velocity. In this chapter, the azimuthal flow velocity is assumed to be zero and, as such, the displacement speed represents directly the propagation speed of the flame edges along the azimuthal direction.

In the context of constant density and Lewis number, the displacement speed, S_d, can be defined by [84, 89–97]:

$$S_d = S_d^R + S_{d,r}^D + S_{d,\theta}^D = \pm \frac{1}{|\nabla Y_k|} \left[\dot{\omega}_k + \frac{1}{Le_k} \left(\frac{1}{r} \frac{\partial}{\partial r} \left(r \frac{\partial Y_k}{\partial r} \right) + \frac{1}{r^2} \frac{\partial^2 Y_k}{\partial \theta^2} \right) \right], \qquad (2.13)$$

where S_d^R, $S_{d,r}^D$, and $S_{d,\theta}^D$ represent the reaction, $r-$ and $\theta-$directional diffusion components of S_d, respectively. The sign in Eq. 2.13 is positive for products and negative for reactants [91]. In this form, therefore, each component of the displacement speed is a measure of its corresponding contribution to the edge flame propagation.

First, the formation of the horseshoe-shaped cellular flame is investigated. Figure 2.13 shows the temporal evolution of S_d and its components of the edge flame during the formation of the horseshoe-shaped cellular flame from the C-shaped IC for $|u_{r,1}/u_{r,2}| = 1.0$ at $Da = 18900$ (see Fig. 2.9). For this case, S_d is evaluated at the intersection of the $Y_F = 0.0765$ isoline and the stagnation plane. This particular intersection coincides approximately with the location of maximum heat release rate of the edge flames. Initially, S_d exhibits a very large value due to the formation of strong edge flames at the two edges of the C-shaped IC, qualitatively similar to the ignition characteristics of S_d in previous studies [84, 92–97]. After the formation of the edge flames, they propagate towards each other with constant positive speed. Note that the flame edges are convex towards both fuel and oxidizer, and hence, the reaction at the flame edges become stronger due to the focusing effect of fuel mass diffusion with $Le_F < 1$. As the two edge flames approach each other, S_d decreases because its reaction term decreases as the $\theta-$directional fuel diffusion into the edge flame decreases. Ultimately S_d vanishes due to the balance that is established between its reaction and diffusion terms and hence, two stationary edge flames form in the absence of merging, forming a horseshoe-shaped cellular flame.

In other words the two edges of the horseshoe-shaped cellular flame maintain their structure by consuming equal amounts of fuel and oxidizer issuing from the nozzles, while reaction at the edges is not strong due to the relatively-small Damköhler number enough to unite them and form a noncellular tubular flame. This result also implies that the horseshoe-shaped cellular flame is generated not by the D-T instability induced by $O(\varepsilon)$ perturbation but rather by the balance between diffusion and reaction at its edges

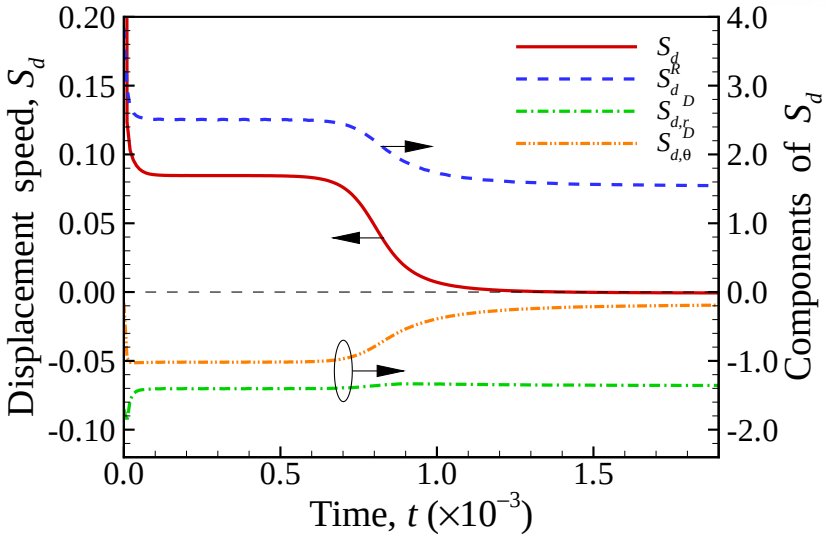

Figure 2.13: Temporal evolution of the displacement speed, S_d, and its components from the C-shaped IC at $Da = 18900$ for $|u_{r,1}/u_{r,2}| = 1.0$.

initiated with $O(1)$ disturbance. In experiments, the $O(1)$ disturbance may be induced by the local extinction of a noncellular tubular flame due to the occurrence of locally-high stretch rate aforementioned.

In addition to the formation of the horseshoe-shaped cellular flame, the dynamics of flame cell formation by the D-T instability is also investigated by examining the displacement speed of the flame cells. Figure 2.14 shows the temperature isocontours and the corresponding 1-D profiles of the displacement speed and its components along the stagnation plane at $Da = 14600$ during the flame cell formation from the horseshoe-shaped cellular flame at the same times as in Fig. 2.12. Note that in the context of non-premixed flames, the displacement speed can be defined only at the location of the flame edges which exhibit propagation characteristics similar to premixed flames. As such S_d at the non-premixed flame between the two flame edges of the horseshoe-shaped cellular flame has no significance except that it represents the balance between diffusion and reaction in the non-premixed flame, manifested by $S_d \approx 0$. In this chapter, however, the profile of S_d along the stagnation plane is examined to elucidate the characteristics of flame cell formation by the D-T instability.

As shown in Fig. 2.14a, the shape of the strong flame edges induces a locally more

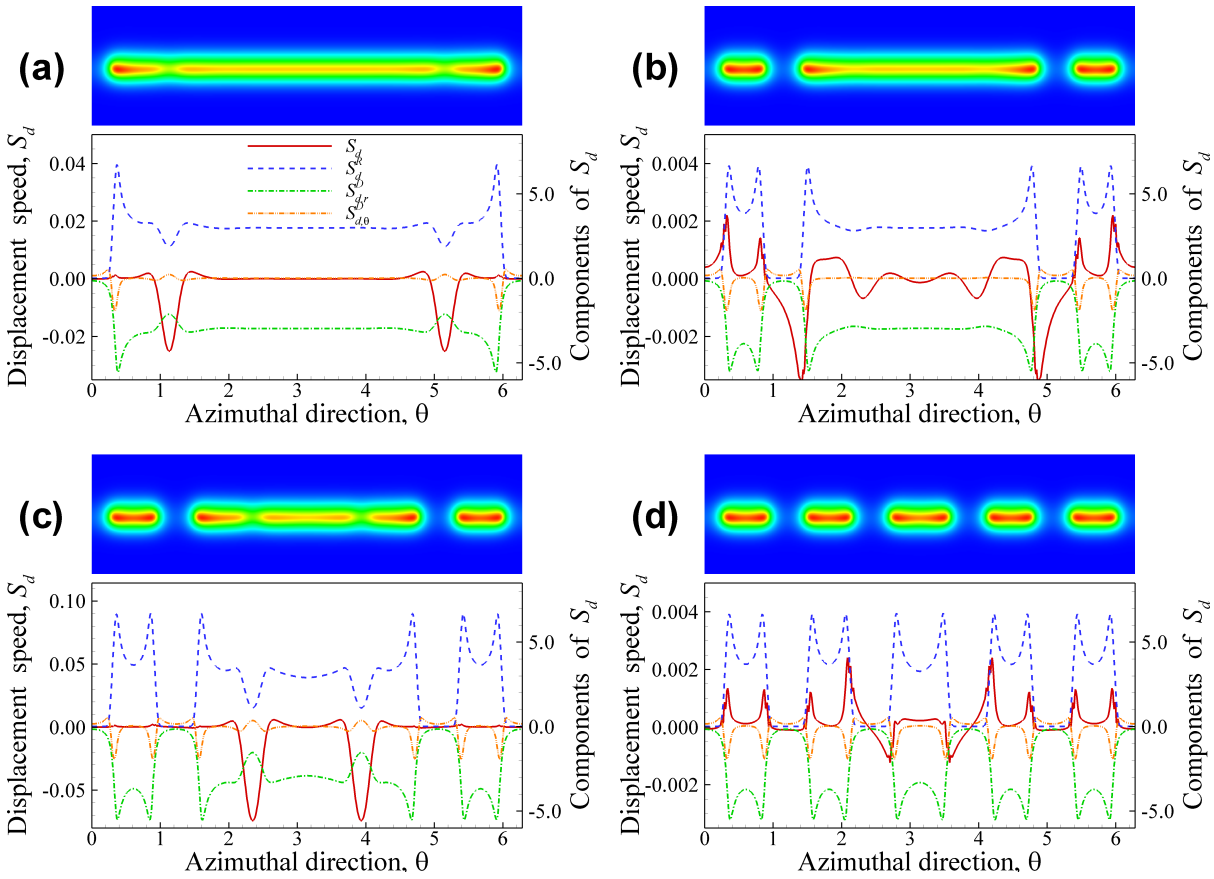

Figure 2.14: Temperature isocontours (top) and the corresponding 1-D profiles of the displacement speed, S_d, and its components along the stagnation plane (bottom) from a horseshoe-shaped cellular flame at $Da = 14600$ for $|u_{r,1}/u_{r,2}| = 1.0$: (a) $t = 2400$, (b) 2800, (c) 5400, and (d) 7200

concave region towards the fuel next to the edges and therefore the defocusing effect of fuel mass diffusion with $Le_F < 1$ in the negatively-curved flame is enhanced, leading to local flame extinction similar to experiments [15]. This is manifested in S_d which exhibits relatively-large negative values due to the significant reduction of the reaction term at the extinction location. Following the local extinction two small flame cells and a large cellular flame featuring a non-premixed flame between the two flame edges are formed as shown in Fig. 2.14b. At this instant, the small flame cells grow while the large cellular flame shrinks, and as such, S_d exhibits relatively-small positive/negative values at the edges of the small flame cells/the large cellular flame. A short while later, this process repeats with another local flame extinction induced by the shape of the flame edges occurring in the large cellular flame (Fig. 2.14c). Ultimately, five flame cells develop approaching a steady state by adjusting their size and location (Fig. 2.14d).

In summary, when local flame extinction occurs, the corresponding S_d exhibits relatively-large negative values at the extinction locations (see Figs. 2.14a and c). Following the local flame extinction, the flame cells adjust their size and location, featuring relatively-small positive or negative S_d. As the size of the flame cell increases/decreases, S_d at the edges of the flame cell exhibits relatively-small positive/negative values as shown in Figs. 2.14b and d.

2.6 Conclusions

The diffusive-thermal instability of opposed non-premixed tubular flames near extinction is investigated using two-dimensional direct numerical simulations together with a linear stability analysis based on their 1-D steady solutions. The characteristics of the D-T instability of tubular flames are identified by a critical Damköhler number, Da_C, where the D-T instability first occurs, and the corresponding number of flame cells, N_{cell}, for three different tubular flames with different flame radii. To elucidate the effect of small and large perturbations on the D-T instability, the perturbed and C-shaped ICs are adopted for the 2-D simulations. The following results were obtained from the 2-D simulations together with the linear stability analysis:

1. The predicted Da_C through the linear stability analysis shows good agreement with that obtained from the 2-D simulations for the two different ICs.

2. The number of flame cell from the 2-D simulations with the perturbed IC is also found to be equal to an integer close to the maximum wavenumber, $k_{\max}$, obtained from the linear stability analysis.

3. However, N_{cell} from the 2-D simulations with the C-shaped IC is smaller than $k_{\max}$ and N_{cell} found from cases with the perturbed IC. This is primarily due to the strong reaction at the edge of the horseshoe-shaped cellular flame which is more likely to create larger flame cells and reduce N_{cell} within the limited space along the azimuthal direction.

4. Once the cellular instability occurs in the 2-D simulations with the C-shaped IC, N_{cell} remains constant until global extinction occurs by incomplete reaction. The flame cells can survive beyond the 1-D extinction Da due to the focusing effect of fuel mass diffusion into the flame cells, for which their size continually decreases as Da gradually decreases.

5. The horseshoe-shaped cellular flame is induced not by the $O(\varepsilon)$ perturbation but by the $O(1)$ disturbance, which may be a consequence of local flame extinction induced by the locally-high stretch rate occurring in experiments.

6. The dynamics of the flame cell formation was also quantified through the displacement speed analysis. The two flame edges of the horseshoe-shaped cellular flame remain stationary in the absence of any merging due to the balance between diffusion and reaction at the flame edges, manifested by $S_d = 0$.

7. Local flame extinction in the horseshoe-shaped cellular flame occurs at the concave region towards the fuel side, which can be identified by relatively-large negative values of S_d. After local extinction, the resultant flame cells with small S_d approach a steady state by adjusting their size and location.

Chapter III

Flame Instability of Opposed Non-premixed Tubular Flames near Radiation-induced Extinction Limit

In this chapter, the flame instabilities and flame cell dynamics in opposed non-premixed tubular flames near radiation-induced extinction limits are elucidated by performing 2-D numerical simulations. The results are compared to those of linear stability analysis to identify the onset of oscillatory and/or D-T instabilities near the radiation-induced extinction limit and to examine their flame features. The dynamics of flame cells beyond the radiation-induced extinction limit and flame characteristics in extremely high radiative intensity environment are also investigated.

3.1 Problem Formulation

3.1.1 1-D Axisymmetric Tubular Flames with Radiative Heat Loss

As in the previous Chapter II, an opposed non-premixed tubular flow configuration is adopted from experiments by Pitz and coworkers [15, 16, 19, 20, 98]. Under simultaneous presence of volumetric heat loss and stretch, non-premixed tubular flames can exhibit dual

extinction states: one induced by large stretch and the other by large heat loss [5, 7, 51]. Prior to performing 2-D simulations of tubular flames, therefore, we first carry out 1-D numerical simulations to examine the characteristics of their extinction states depending on radiative heat loss. Similar to those in previous studies [49, 51, 99], radiative heat loss is taken into account as a simple optically-thin radiation model in the energy equation. Then, the governing equations of temperature, fuel, and oxidizer species for the opposed non-premixed tubular flames with radiative heat loss are given by:

$$\begin{aligned}\widetilde{\rho}\widetilde{u}_r\frac{d}{d\widetilde{r}}\begin{pmatrix}\widetilde{c}_p\widetilde{T}\\ \widetilde{Y}_F\\ \widetilde{Y}_O\end{pmatrix} &= \frac{1}{\widetilde{r}}\frac{d}{d\widetilde{r}}\left(\widetilde{r}\frac{d}{d\widetilde{r}}\right)\begin{pmatrix}\widetilde{\lambda}\widetilde{T}\\ \widetilde{\rho}\widetilde{D}_F\widetilde{Y}_F\\ \widetilde{\rho}\widetilde{D}_O\widetilde{Y}_O\end{pmatrix}\\ &\quad+\widetilde{B}\widetilde{Y}_F\widetilde{Y}_O e^{-\widetilde{E}/\widetilde{R}\widetilde{T}}\begin{pmatrix}\widetilde{Q}\\ -\alpha_F\\ -\alpha_O\end{pmatrix}-4\widetilde{\sigma}\widetilde{K_p}\begin{pmatrix}\widetilde{T}^4-\widetilde{T}_\infty^4\\ 0\\ 0\end{pmatrix},\end{aligned} \tag{3.1}$$

where $\widetilde{T}$, $\widetilde{Y}_F$, and $\widetilde{Y}_O$ are the dimensional temperature, fuel mass fraction, and oxidizer mass fraction, respectively, with the density, $\widetilde{\rho}$, radial velocity, $\widetilde{u}_r$, specific heat, $\widetilde{c}_p$, thermal conductivity, $\widetilde{\lambda}$, fuel diffusivity, $\widetilde{D}_F$, oxidizer diffusivity, $\widetilde{D}_O$, frequency factor, $\widetilde{B}$, activation energy, $\widetilde{E}$, universal gas constant, $\widetilde{R}$, heat of reaction, $\widetilde{Q}$, stoichiometric coefficients, α_F and α_O, $\widetilde{\sigma}$, the Stefan-Boltzmann constant, $\widetilde{K_p}$, the Planck mean absorption coefficient, and independent variable, $\widetilde{r}$, denoting the radial direction. In this chapter, we adopt a constant density model to investigate flame instabilities assuming an ideal situation without complex flow generated by density variation or thermal expansion [4, 13, 14, 21, 24, 51, 84, 100]. Therefore, the analytic solution of the radial velocity, $\widetilde{u}_r$, is used as in [85, 100].

By normalizing the dimensional variables with appropriate reference values, i.e. $r = \widetilde{r}/\sqrt{\widetilde{\lambda}/\widetilde{\rho}\widetilde{c_p}\widetilde{\kappa}}$, $u_r = \widetilde{u}_r/\sqrt{\widetilde{\kappa}\widetilde{\lambda}/\widetilde{\rho}\widetilde{c_p}}$, $T = \widetilde{T}/\widetilde{T}_{\mathrm{ref}}$, $Y_F = \widetilde{Y}_F/\widetilde{Y}_{F,1}$, and $Y_O = \widetilde{Y}_O/\widetilde{Y}_{O,2}$, Eq. (3.1)

can be written in non-dimensional form with radiative heat loss:

$$u_r \frac{d}{dr}\begin{pmatrix} T \\ Y_F \\ Y_O \end{pmatrix} = \frac{1}{r}\frac{d}{dr}\left(r\frac{d}{dr}\right)\begin{pmatrix} T \\ Y_F/Le_F \\ Y_O/Le_O \end{pmatrix} + DaY_FY_Oe^{-T_a/T}\begin{pmatrix} q \\ -\alpha_F\widetilde{Y}_{O,2} \\ -\alpha_O\widetilde{Y}_{F,1} \end{pmatrix} - Ra\begin{pmatrix} T^4 - T_\infty^4 \\ 0 \\ 0 \end{pmatrix}, \tag{3.2}$$

where Le_F $(= \widetilde{\lambda}/\widetilde{\rho}\widetilde{c_p}\widetilde{D}_F)$ is the fuel Lewis number, Le_O $(= \widetilde{\lambda}/\widetilde{\rho}\widetilde{c_p}\widetilde{D}_O)$ is the oxidizer Lewis number, Da $(= \widetilde{B}/\widetilde{\rho}\widetilde{\kappa})$ is the Damköhler number, q $(= \widetilde{Y}_{F,1}\widetilde{Y}_{O,2}\widetilde{Q}/\widetilde{c}_p\widetilde{T}_{\rm ref})$ is the heat of reaction, T_a $(= \widetilde{E}/\widetilde{R}\widetilde{T}_{\rm ref})$ is the activation temperature, and Ra $(= 4\widetilde{\sigma}\widetilde{T}_{\rm ref}^3\widetilde{K_p}/\widetilde{\rho}\widetilde{c_p}\widetilde{\kappa})$ is the radiative heat loss parameter. Note that $\widetilde{\kappa}$ is the reference stretch rate and is inversely proportional to Da by definition. Note also that Da $(= \widetilde{B}/\widetilde{\rho}\widetilde{\kappa})$ represents the ratio of the convection time to the collision time of the system and is often called the collision Damköhler number [5]. Therefore, even stretch-induced flame extinction occurs at very large Da rather than $Da < 1$. Ra can be expressed as $Ra = Da \cdot I$, where I $(= 4\widetilde{\sigma}\widetilde{T}_{\rm ref}^3\widetilde{K_p}/\widetilde{B}\widetilde{c_p})$ is the radiative intensity which will be used as a key parameter determining the magnitude of radiative heat loss. The corresponding non-dimensional boundary conditions at the two inlets are given by:

$$\begin{cases} T = T_1,\ Y_F = 1,\ Y_O = 0,\ u_r = u_{r,1}, & \text{at } \ r = r_1, \\ T = T_2,\ Y_F = 0,\ Y_O = 1,\ u_r = u_{r,2}, & \text{at } \ r = r_2. \end{cases} \tag{3.3}$$

Note that the subscripts 1 and 2 denote the fuel and oxidizer inlets, respectively.

To investigate the flame instabilities of non-premixed tubular flames affected by radiative heat loss, we specify $q = 1.2$, $T_a = 8$, $Le_F = 0.3$, $Le_O = 1.0$, $\alpha_F\widetilde{Y}_{O,2} = 1.0$, $\alpha_O\widetilde{Y}_{F,1} = 0.36$, $r_1 = 20$, $r_2 = 100$, $T_1 = T_2 = 0.2$, $u_{r,1} = 1$, and $u_{r,2} = -1$. These values are properly adopted to render the maximum flame temperature, $T_{\max}$, at the stretch-induced extinction Damköhler number, $Da_{E,S}$, to be close to unity. Therefore, if $T_1 = T_2 = 0.2$ is assumed to be room temperature of 300 K, $T \approx 1$ represents approximately 1500 K [13, 100]. For more details of the problem formulation, readers are referred to [100].

3.1.2 1-D Steady Solutions

Figure 3.1 shows the response of the maximum flame temperature, $T_{\max}$, of the axisymmetric tubular flames to Da for four different I and the representative radial profiles of the temperature and mass fractions at two critical Damköhler numbers with $I = 10^{-8}$. The profile of the radial velocity, u_r, adopted for the present study is also shown in the figure. The response curves are obtained by solving the governing equations using the Newton-Raphson method with a simple continuation algorithm [84, 100]. It is readily observed from the figure that the nonadiabatic tubular flames have two extinction states similar to nonadiabatic non-premixed/premixed counterflow flames [5, 7, 51] and the extent of the combustible regime shrinks with increasing I. In high Da regime, $T_{\max}$ keeps decreasing with increasing Da for a given I due to the radiative heat loss until Da reaches a critical Damköhler number, $Da_{E,R}$, corresponding to the radiation-induced extinction. At this limit, the radiative heat loss overwhelms heat release from the flame, consequently leading to extinction despite large Da or low flame stretch. The effect of radiative heat loss is manifested by the shrinkage of the combustible regime or by large variation of $Da_{E,R}$ from 2.523×10^9 to 1.125×10^5 with increasing I.

In relatively-small Da regime, however, the effect of radiative heat loss is marginal and hence, the flame extinction occurs primarily by incomplete reaction due to high flame stretch [5, 49]. As such, the stretch-induced extinction Damköhler number, $Da_{E,S}$, remains nearly identical regardless of I. Even in the small Da regime, however, the effect of radiative heat loss becomes significant for extremely-large radiative intensity (i.e. $I = 3.7 \times 10^{-7}$) and hence, $Da_{E,S}$ for this case exhibits several times larger value than those for cases with small I. Therefore, the characteristics of tubular flames with $I = 10^{-8}$ are first investigated and then, those with an extremely-large radiation intensity of $I = 3.7 \times 10^{-7}$ are examined.

3.1.3 2-D Tubular Flames

To elucidate the characteristics of flame instability of non-premixed tubular flames with radiative heat loss, we extend the governing equations of 1-D steady tubular flames

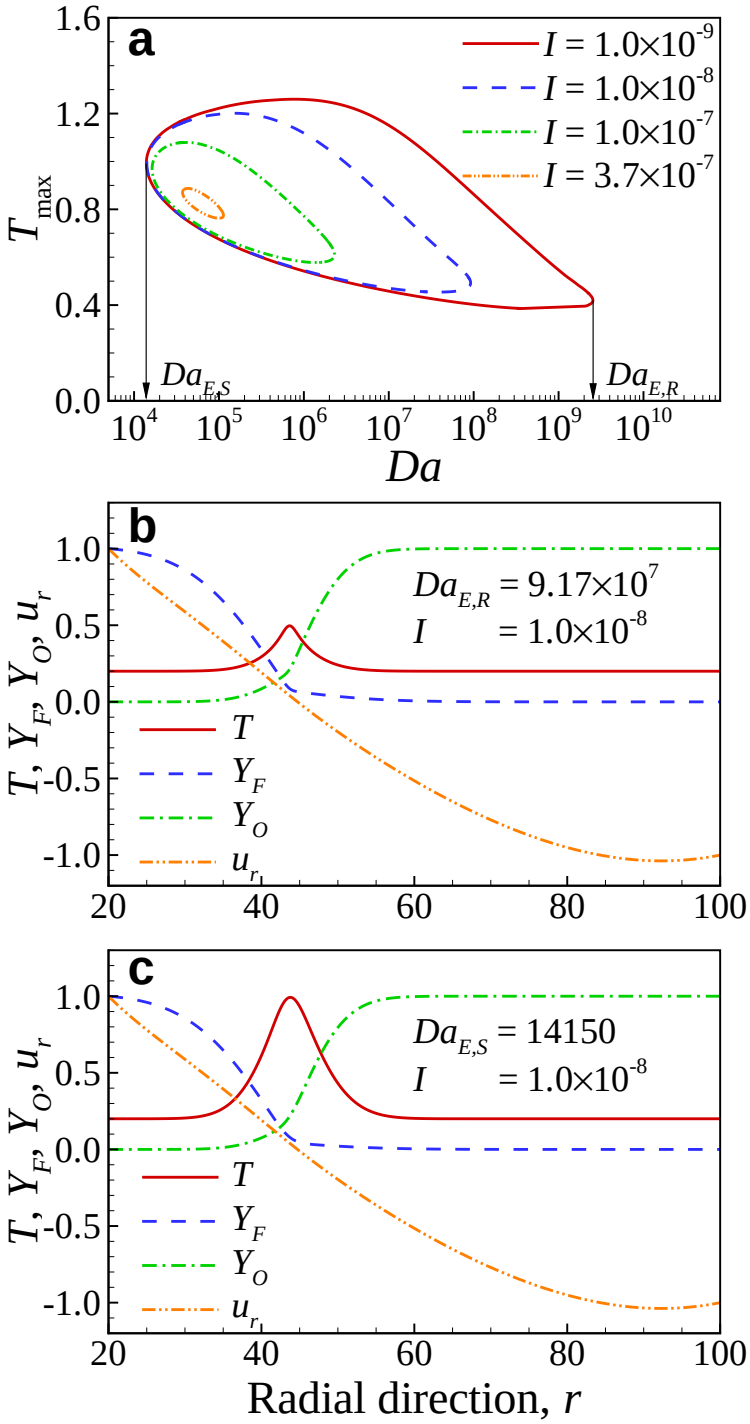

Figure 3.1: (a) The response of the maximum flame temperature, $T_{\max}$, to the Damköhler number, Da, for four different radiative intensities, I, and the radial profiles of temperature, fuel/oxidizer mass fractions, and radial velocity at (b) the radiation induced extinction Damköhler number, $Da_{E,R} = 9.17 \times 10^7$, and (c) the stretch induced extinction Damköhler number, $Da_{E,S} = 14150$, with $I = 10^{-8}$.

to time-dependent partial differential equations involving variations in the azimuthal direction, θ [4, 13, 21, 51, 84, 100]:

$$\left(\frac{\partial}{\partial t}+u_r\frac{\partial}{\partial r}\right)\begin{pmatrix}T\\Y_F\\Y_O\end{pmatrix}=\left(\frac{1}{r}\frac{\partial}{\partial r}\left(r\frac{\partial}{\partial r}\right)+\frac{1}{r^2}\frac{\partial^2}{\partial\theta^2}\right)\begin{pmatrix}T\\Y_F/Le_F\\Y_O/Le_O\end{pmatrix} + DaY_FY_Oe^{-T_a/T}\begin{pmatrix}q\\-\alpha_F\widetilde{Y}_{O,2}\\-\alpha_O\widetilde{Y}_{F,1}\end{pmatrix}-Ra\begin{pmatrix}T^4-T_\infty^4\\0\\0\end{pmatrix}. \tag{3.4}$$

The 2-D transient problems are also subject to the same boundary conditions of Eq. 3.3 in the $r-$direction as in the 1-D problems. Periodic boundary condition are imposed in the $\theta-$direction. 2-D numerical simulations of tubular flames are performed using a six-stage fourth-order explicit Runge-Kutta method for time integration and an eighth-order central finite-difference scheme for evaluating spatial derivatives [86, 87] as in [84, 100]. The message passing interface (MPI) is used for scalable parallelism. After a series of grid convergence tests, a grid system of 400 $\times$ 2400 is adopted to discretize the $r-$ and $\theta-$directions for all cases. A timestep, Δt, of 10^{-3} is required for accurate time integration.

For 2-D simulations, three different initial conditions (IC) are adopted to investigate the effects of disturbance magnitude (i.e., $O(\varepsilon)$ or $O(1)$) and shape (i.e., symmetric or asymmetric) on the flame instability and cell dynamics. Figure 3.2 shows three different initial temperature fields for 2-D simulations of opposed non-premixed tubular flame: (a) perturbed IC, (b) C-shaped IC, and (c) asymmetric IC.

The perturbed IC is obtained by superimposing a small sinusoidal perturbation of temperature ($\sim O(\varepsilon)$) on the steady solution field [100]:

$$T(r,\theta,t=0)=T_{\text{1-D}}(r)+\varepsilon\cdot\sin\theta\cdot(T_{\text{1-D}}(r)-T_1)\quad:0\le\theta<2\pi, \tag{3.5}$$

where $T_{\text{1-D}}(r)$ represents the 1-D steady temperature solution of Eq. 3.2. The perturbation amplitude of $\varepsilon=10^{-5}$ is selected through a series of 2-D simulations from which it is confirmed that there is no change in the number of flame cells and extinction behavior

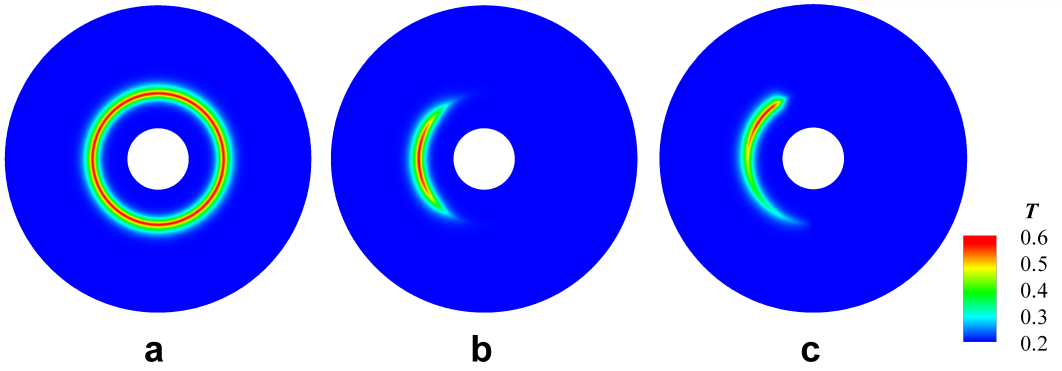

Figure 3.2: Three different initial temperature fields for 2-D simulations of opposed non-premixed tubular flame: (a) the perturbed IC, (b) the C-shaped IC, and (c) the asymmetric IC.

for $\varepsilon \leq 10^{-5}$ [100]. This initial condition is employed to investigate fundamental D-T instability of 2-D tubular flames as a function of Da.

The C-shaped IC is devised by combining intensely-burning and frozen-flow solutions through a smooth transition using the hyperbolic tangent function, representing large disturbance ($\sim O(1)$) [100]:

$$\mathbf{x}(r,\theta,t=0) = \mathbf{x}_{\text{1-D,F}}(r) + 1 \cdot \left[\left(\tanh(\theta-\theta_1) - \tanh(\theta-\theta_2)\right)/\sigma\right] \cdot \left(\mathbf{x}_{\text{1-D,B}}(r) - \mathbf{x}_{\text{1-D,F}}(r)\right)/2 \quad : 0 \leq \theta < 2\pi, \tag{3.6}$$

where $\mathbf{x}$ is the solution vector including T, Y_F, and Y_O; $\theta_1 = 3\pi/4$; $\theta_2 = 5\pi/4$; $\sigma = \pi/10$. The subscripts B and F represent intensely-burning and frozen-flow solutions. The C-shaped IC is adopted to identify the effect of large symmetric amplitude disturbance on flame dynamics. The third IC referred to as the asymmetric IC is employed to elucidate the effect of asymmetric disturbance on the flame dynamics especially at very large Da. The asymmetric IC is devised by shifting the peak of the C-shaped IC from π to 0.83π and by smoothly combining the Gaussian function ($\pi/2 \leq \theta < 0.83\pi$), a linear function, ($0.83\pi \leq \theta < 3\pi/2$), and the frozen-flow solution in the remaining area.

3.2 Stability Analysis

Prior to conducting the analysis of 2-D simulations, we performed linear stability analysis to understand the flame instability characteristics as in [13, 21, 100]. For this purpose, a steady solution of Eq. 3.1, denoted by an overbar, is perturbed with small harmonic perturbations:

$$T = \bar{T}(r) + \epsilon T'(r) e^{ik\theta+\lambda t},\ Y_F = \bar{Y}_F(r) + \epsilon Y'_F(r) e^{ik\theta+\lambda t},\ Y_O = \bar{Y}_O(r) + \epsilon Y'_O(r) e^{ik\theta+\lambda t}, \quad (3.7)$$

where λ is a complex number for which the real part, $\mathrm{Re}(\lambda)$, represents the growth rate, k is the wavenumber and ϵ is the small perturbation amplitude similar to ε in the perturbed IC. Substituting Eq. 3.7 into Eq. 3.4 and linearizing the equation yields:

$$\begin{aligned} \frac{1}{r}\frac{d}{dr}\left(r\frac{d}{dr}\right)\begin{pmatrix} T' \\ Y'_F/Le_F \\ Y'_O/Le_O \end{pmatrix} - u_r\frac{d}{dr}\begin{pmatrix} T' \\ Y'_F \\ Y'_O \end{pmatrix} - \begin{pmatrix} 4Ra\bar{T}^3 + k^2/r^2 + \lambda \\ k^2/r^2 Le_F + \lambda \\ k^2/r^2 Le_O + \lambda \end{pmatrix}\begin{pmatrix} T' \\ Y'_F \\ Y'_O \end{pmatrix} \\ + Da e^{-T_a/\bar{T}}\left(\bar{Y}_O Y'_F + \bar{Y}_F Y'_O + \frac{\bar{Y}_F\bar{Y}_O}{\bar{T}^2}T_a T'\right)\begin{pmatrix} q \\ -\alpha_F\widetilde{Y}_{O,2} \\ -\alpha_O\widetilde{Y}_{F,1} \end{pmatrix} = 0, \end{aligned} \quad (3.8)$$

where the boundary conditions are $T' = Y'_F = Y'_O = 0$ at both $r = r_1$ and $r = r_2$. An eigenvalue problem of $(\mathbf{A} - \lambda\mathbf{B})\mathbf{x}' = 0$ is then obtained by discretizing Eq. 3.8, where $\mathbf{x}'$ is the discretized solution vector including T', Y'_F, and Y'_O.

We obtain the largest growth rate, λ_R, among many $\mathrm{Re}(\lambda)$ by solving the eigenvalue problem for given Da and k because λ_R plays a critical role in determining instability characteristics of strained flames as demonstrated in [4, 21, 24, 100]. By examining the variation of λ_R with respect to k at a given Da, we can predict the instability characteristics of 2-D tubular flames. If all λ_R exhibit negative values over the entire range of k, small disturbances would decay and hence, we would obtain a stable noncellular tubular flame. However, if any λ_R exhibits a positive value at a certain k, even infinitesimally-small disturbances could grow in time, resulting in the occurrence of D-T instability [100]. Furthermore, when the imaginary part of λ corresponding to λ_R, λ_I, exhibits a non-zero value, tubular flames would show oscillatory behavior.

Figure 3.3 shows λ_R as a function of k for several different Da near the 1-D radiation-induced extinction limit, $Da_{E,R} = 9.17 \times 10^7$, with $I = 10^{-8}$. Note that dotted segments in the figure denote the existence of non-zero λ_I. Several points are noted from the figure. First, we can expect that cellular flame instability occurs when Da is greater than $Da_{C,C} = 5.76 \times 10^7$ at which the first non-negative λ_R appears (see Fig. 3.3a). In our previous study [100], it was confirmed through the linear stability analysis and 2-D simulations that the D-T instability starts to occur at such Damköhler number that the maximum λ_R, $\lambda_{R,\max}$, exhibits a positive value at a certain wavenumber.

Second, we can also expect that the oscillatory instability may start at $Da_{C,D} = 5.15 \times 10^7$ where the first non-zero λ_I appears (see Fig. 3.3a). Within the range of Da between $Da_{C,D}$ and $Da_{C,G} = 6.17 \times 10^7$, the oscillatory instability would decay because all λ_R corresponding to non-zero λ_I exhibit negative values. However, when Da is greater than $Da_{C,G}$, the oscillatory instability would grow because λ_R corresponding to nonzero λ_I becomes positive. In addition, when Da becomes sufficiently large, we cannot observe any nonzero λ_I, which implies that there would be no oscillatory instability (see Fig. 3.3c).

Third, the maximum wavenumber, $k_{\max}$, at which λ_R attains its maximum value decreases gradually from 28.8 at $Da_{C,C} = 5.76 \times 10^7$ with increasing Da. In addition, the maximum λ_R and the range of k exhibiting positive λ_R also increases with increasing Da. It was also confirmed from our previous study [100] that the values of $k_{\max}$ and $\lambda_{R,\max}$ together with the range of k with positive λ_R are closely related to the number of flame cells and the vulnerability of 2-D tubular flames to the D-T instability, respectively. To be more specific, the number of flame cells is nearly identical to $k_{\max}$ value and the D-T instability occurs more quickly in time with increasing $\lambda_{R,\max}$. This is because large Da induces more radiative heat loss from the flame, resulting in large λ_R near the radiation-induced extinction limit. This is different from the characteristics of λ_R response to Da near the stretch-induced extinction limit, where the $\lambda_{R,\max}$ and the range of k exhibiting positive λ_R increases with decreasing Da due to incomplete reaction [100].

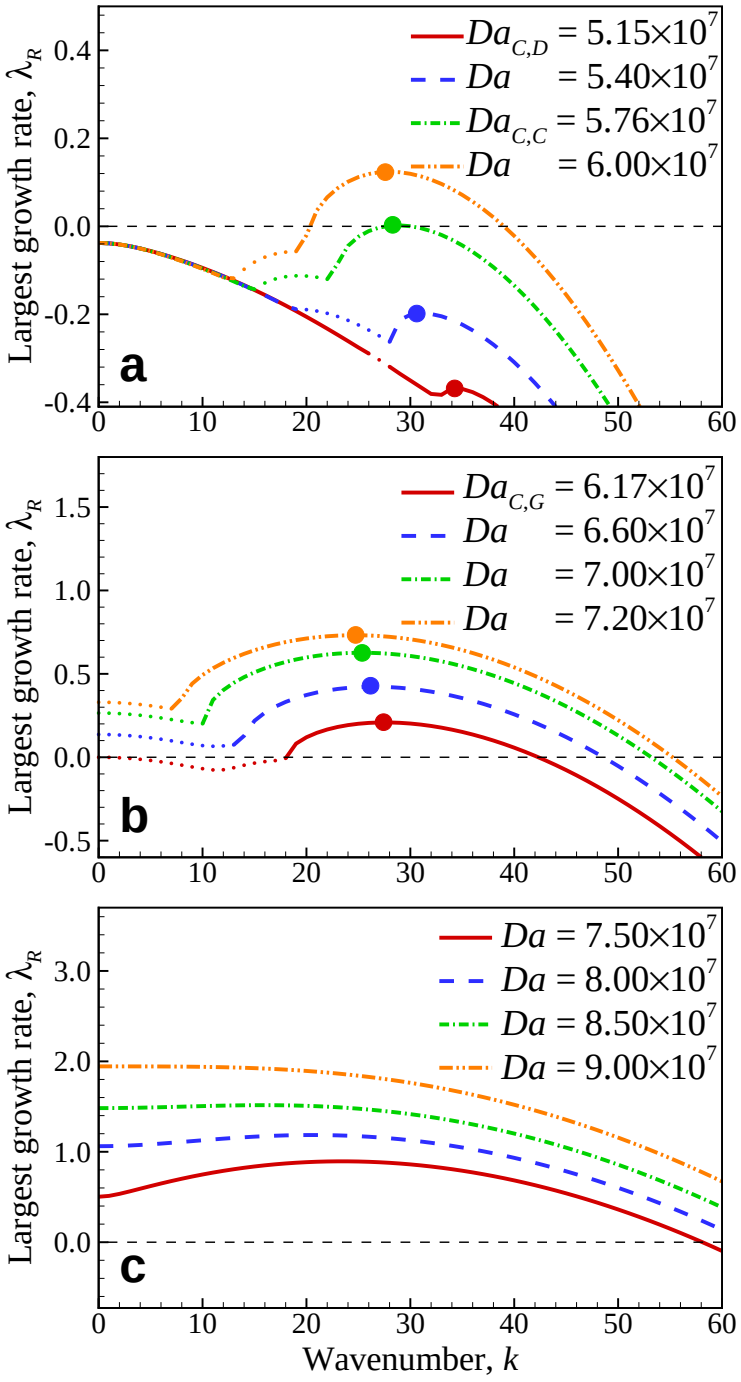

Figure 3.3: The largest growth rate, λ_R, as functions of the wavenumber, k, for several different Damköhler number, Da, with $I = 10^{-8}$. Dotted segments represent nonzero imaginary part of λ ($\lambda_I \neq 0$). The solid circles represent the points of $\lambda_{R,\max}$ and $k_{\max}$.

3.3 The D-T and Oscillatory Instabilities with the Perturbed IC

In this section, we investigate the transient dynamics of D-T and oscillatory instabilities and consequent steady characteristics of a cellular flame in opposed non-premixed tubular flames with radiative heat loss at different Da near the radiation-induced extinction limit. For this purpose, we performed 2-D numerical simulations of tubular flames with the perturbed IC. Here, we adopt the perturbed IC with small amplitude disturbance to numerically initiate flame instabilities, similar to the infinitesimally-small perturbation in the linear stability analysis. Therefore, we can identify the origin of flame instabilities by comparing the simulation results with those from the linear stability analysis.

Figure 3.4 shows the temperature isocontours of a steady cellular flame developed from the perturbed IC at $Da_{E,P} = 6.27 \times 10^7$. For comparison purpose, we also show those at the stretch-induced extinction limit of $Da_{E,S}$ in the figure. Note that flame instabilities lead to total extinction of all 2-D tubular flames with the perturbed IC beyond $Da_{E,P}$. Henceforth, $Da_{E,P}$ is denoted as the radiation-induced 2-D extinction Damköhler number with the perturbed IC. Two points are noted from the figure. First, we can readily observe that the flame cell size at $Da_{E,P}$ is much smaller than that at $Da_{E,S}$ and the number of flame cells, N_{cell}, at $Da_{E,P}$ is much larger than that at $Da_{E,S}$; N_{cell} for the two cases are found to be 7 and 27, respectively. Considering the results of the linear stability analysis, it is reasonable that the cellular flame near $Da_{E,P}$ has more flame cells than that at $Da_{E,S}$. From our previous study [100], it was verified that N_{cell} in 2-D simulations is nearly identical to the corresponding $k_{\max}$ value from the linear stability analysis; for two cases, $k_{\max}$ values are found to be 7.8 and 27.4, respectively.

From the linear stability analysis, it is observed that as the radiation intensity increases from 10^{-9} to 3.7×10^{-7}, $Da_{E,R}$ decreases from 2.523×10^9 to 1.125×10^5 and $k_{\max}$ at $Da_{C,G}$ near $Da_{E,R}$ changes from 38.9 to 11.9. However, $Da_{E,S}$ slightly increases from 1.397×10^4 to 3.737×10^4 with increasing I and the corresponding $k_{\max}$ values changes from 7.8 to 9.7. This result implies that the number of flame cells related to $k_{\max}$ is highly

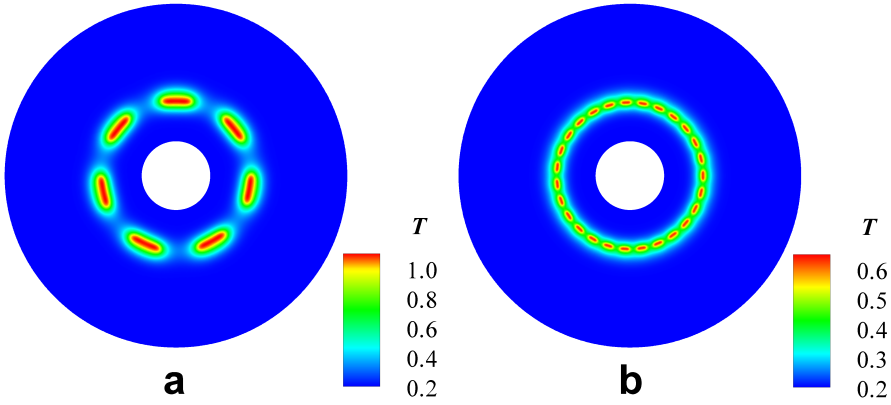

Figure 3.4: Temperature isocontours of steady cellular flames induced by the D-T instability from the perturbed IC with $I = 10^{-8}$ at (a) the stretch-induced extinction limit, $Da_{E,S} = 14150$, and (b) 2-D radiation-induced extinction limit, $Da_{E,P} = 6.27 \times 10^7$.

dependent on the magnitude of Damköhler number when the D-T instability occurs. In Eq. 3.8, the source terms including Da and $-k^2/r^2$ terms are the main diagonal elements of $\mathbf{A}$ in the eigenvalue problem of $(\mathbf{A} - \lambda\mathbf{B})\mathbf{x}' = 0$. Therefore, if a cellular flame instability occurs at significantly large Da, only large k value may possibly compensate for such large source term including Da so that $\lambda_{R,\max}$ can exhibit relatively-small values as shown in Fig. 3.3. Therefore, since the combustible regime increases with decreasing I, the D-T instability occurs progressively at large Da with decreasing I and hence, $k_{\max}$ increases with decreasing I as shown in Fig. 3.1b.

Second, $T_{\max}$ at $Da_{E,P} = 6.27 \times 10^7$ is 0.634, which is much smaller than $T_{\max}$ of 1.24 at $Da_{E,S}$. Overall, the temperature of noncellular tubular flame at high Da is much smaller than that at low Da due to significant radiative heat loss as shown in Fig. 3.1b. To overcome such large radiative heat loss at $Da_{E,P}$, therefore, the flame cells cannot help but reduce their size and benefit from the focusing effect of the fuel with small Lewis number.

To further identify the radiation effects on flame structure, we analyze transport budgets of each cellular flame along three different radial and azimuthal lines. Figure 3.5 shows the magnitudes of transport budgets including convection, diffusion, reaction, and radiation terms of the temperature equation in Eq. 3.4. It is readily observed from Figs. 3.5a and b that for the flame cells at $Da_{E,S}$, the reaction term balances the diffusion

term while the convection and radiation terms are negligible. For the flame cells at $Da_{E,P}$ (see Fig. 3.5d and e), however, the reaction terms balance the radiation and diffusion terms. The magnitude of each term at $Da_{E,P}$ is greater than that of the corresponding term at $Da_{E,S}$ due to significantly-large Da while $T_{\max}$ at $Da_{E,P}$ is much lower than that at $Da_{E,S}$. These results verify that the radiative heat loss reduces the temperature of flame cells at $Da_{E,P}$ despite the large heat release due to significantly-large Da and the focusing effect of fuel with small Le_F enhanced by their small cell size with large curvature.

It is also observed that there exist quenched regions between the flame cells at $Da_{E,S}$ (see Figs. 3.5a and c). However, the balance between strong reaction and radiation heat loss at $Da_{E,P}$ leads to alternating locally-weak and locally-strong flame cells even at the steady state without local extinction (see Figs. 3.5d and f). It is of interest to note that from their experiments and detailed numerical simulations of the D-T instability of non-premixed hydrogen/air tubular flames, Hall and Pitz [98] found that there still exists low temperature chemistry featured by HO_2 and H_2O_2 between high temperature flame cells, which implies that the quenched regions at $Da_{E,S}$ in Fig. 3.5a and c may be an artifact caused by the one-step overall chemistry adopted in the present simulations.

The characteristics of flame instabilities in opposed tubular flames with radiative heat loss are further investigated by examining the transient dynamics of flame cell formation from a noncellular tubular flame with the perturbed IC. Figure 3.6 shows the temporal evolution of $T_{\max}$ for several cases at different Da from which four different regimes of flame response to the initial perturbation are identified. In Regime I, the oscillatory instability represented by $T_{\max}$ oscillation occurs from the beginning but it quickly decays, leading to a noncellular tubular flame without the D-T instability (see Fig. 3.6a). Although this decaying oscillatory instability is predicted from the linear stability analysis, it is rarely observed at the vicinity of $Da_{C,D}$ due to its small magnitude in 2-D simulations. In Regime II, the D-T instability takes over the decaying oscillatory instability, resulting in a cellular flame (see Fig. 3.6a). In this regime, $\lambda_{R,\max}$ starts to have positive values from the linear stability analysis. In Regime III, the oscillatory instability grows followed by the D-T instability in the end. Finally, the fast growth of the oscillatory

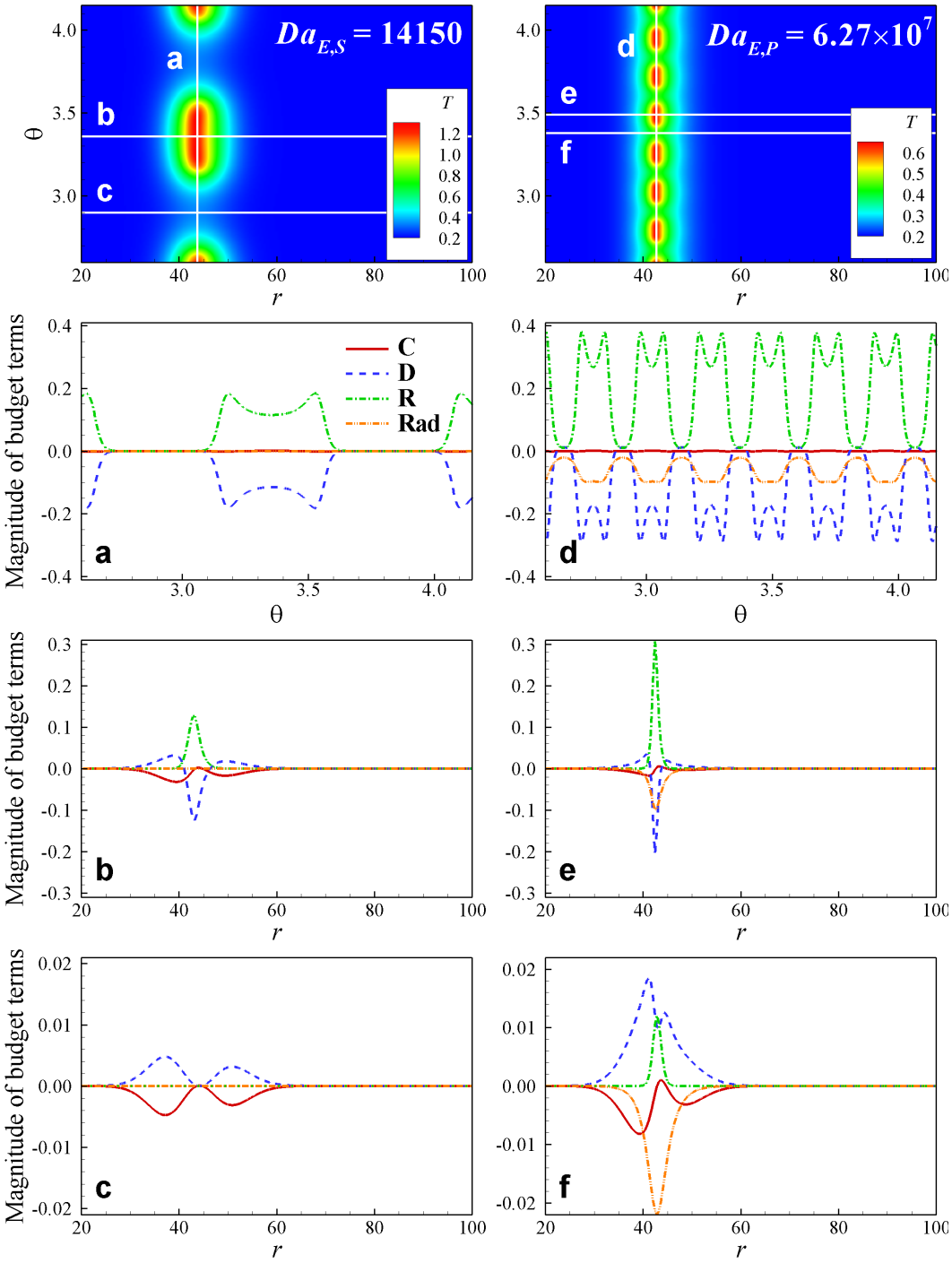

Figure 3.5: Profiles of convection, diffusion, reaction, and radiation terms along several different axial and azimuthal lines for the flames at (a–c) $Da_{E,S} = 14150$ and (d–f) $Da_{E,P} = 6.27 \times 10^7$. Top figures show locations of axial and azimuthal lines for (a–f).

instability results in total extinction of the tubular flame in Regime IV. Based on the results of the linear stability analysis and 2-D simulations, the four regimes of the flame response to the initial perturbation are summarized as follows:

1. Regime I – a noncellular flame with decaying oscillation ($Da_{C,D} \leq Da < Da_{C,C}$; see Fig. 3.6a).

2. Regime II – a cellular flame with decaying oscillation ($Da_{C,C} \leq Da < Da_{C,G}$; see Fig. 3.6a).

3. Regime III – a cellular flame with growing oscillation ($Da_{C,G} \leq Da \leq Da_{E,P}$; see Fig. 3.6b).

4. Regime IV – total extinction with growing oscillation ($Da_{E,P} < Da \leq Da_{E,R}$; see Fig. 3.6c).

Note that the critical Damköhler numbers such as $Da_{C,D}$, $Da_{C,C}$, and $Da_{C,G}$ in the 2-D simulations are nearly the same as the corresponding Da from the linear stability analysis, which verifies that the linear stability analysis is able to predict the oscillatory and D-T instabilities of the tubular flames for the 2-D simulations with reasonable accuracy.

It is of importance to note that in previous 1-D numerical simulations [49, 51], three different responses of diffusion flames triggered by radiative heat loss were identified regardless of fuel Lewis number: (1) decaying oscillatory solution, (2) diverging solution to extinction, and (3) stable limit-cycle solution. The limit-cycle solution lies between the decaying and diverging solutions such that it exhibits continuous oscillation without decaying or diverging. In this chapter, however, the limit-cycle flame response cannot be observed although the decaying oscillatory instability (Regime I) and diverging solution to extinction (Regime IV) are found. This is because the oscillatory instability is combined with the D-T instability near $Da_{E,R}$ when the fuel Lewis number is less then unity. Moreover, it is found from the present 2-D simulations and the linear stability analysis that the D-T instability always starts to occur at $Da_{C,C}$ less than the onset Damköhler number of the growing oscillatory instability, $Da_{C,G}$, as shown in Figs. 3.3

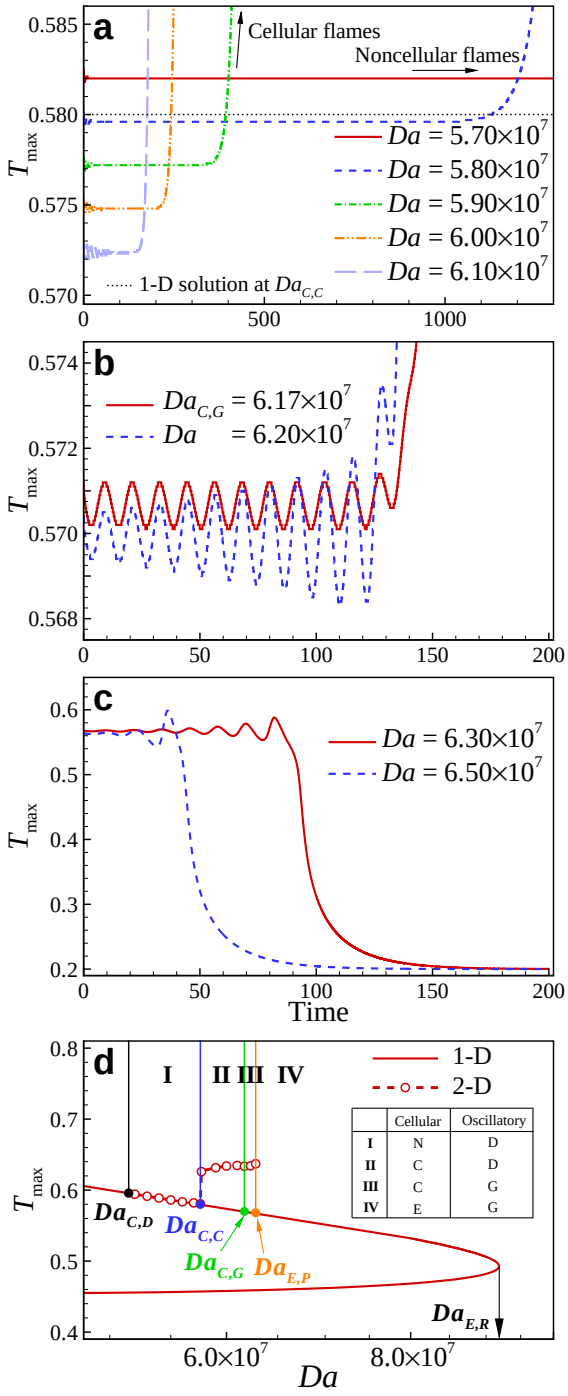

Figure 3.6: Temporal evolutions of the maximum flame temperature, $T_{\max}$, for (a – c) different Damköhler numbers, Da, and (d) the regime diagram of the flame response to the perturbed IC with $I = 10^{-8}$: I – a noncellular flame with decaying oscillation, II – a cellular flame with decaying oscillation, III – a cellular flame with growing oscillation, and IV – total extinction with growing oscillation. N: Noncellular flame, C: Cellular flame, E: Extinction, D: Decaying oscillation, and G: Growing oscillation.

and 3.6. Therefore, the D-T instability overwhelms the oscillatory instability with the limit-cycle as in case with $Da = 6.17 \times 10^7$ (Fig. 3.6b).

3.4 The D-T Instability with the C-shaped IC

In our previous study [100], the effect of large amplitude disturbance on the D-T instability was examined using the C-shaped IC to mimic an experimental procedure [15]; a horseshoe-shaped cellular flame is first generated from the C-shaped IC and then, relatively-large flame cells are subsequently formed with decreasing Da due to strong reaction at the edge of the horseshoe-shaped cellular flame, leading to a small number of flame cells compared to that with the perturbed IC [100]. In this section, we investigate the characteristics of flame response to the C-shaped IC by progressively increasing Da, similar to the above procedure; once a cellular flame with multiple flame cells is first formed from the C-shaped IC, successive simulations at successively larger Da are restarted from each of the previous steady solutions, resetting the simulation time to the beginning upon restarting.

Figure 3.7 shows the variation of $T_{\max}$ as a function of Da with $I = 10^{-8}$. Three representative temperature isocontours at different Da are also shown in the figure. Two points are to be noted. First, unlike the flame response near $Da_{E,S}$ [100], a horseshoe-shaped cellular flame is not observed near the radiation-induced extinction limit. Two flame edges developed from the C-shaped IC propagate towards each other and merge to form a noncellular flame whenever $Da < Da_{C,C}$. As such, flame cellularity from the C-shaped IC occurs at the exactly same Damköhler number, $Da = 5.77 \times 10^7$, as the perturbed IC.

Second, once a steady cellular flame with multiple flame cells is generated, its flame cell number remains the same with increasing Da until global extinction occurs at $Da_{E,T} = 1.85 \times 10^9$, which is qualitatively consistent with the result in [100]. As discussed above, in the 2-D simulations with the perturbed IC the number of flame cells changes according to $k_{\max}$ from the linear stability analysis. For the cases with the C-shaped IC, however, the flame cells generated from the C-shaped IC survive large radiative heat loss

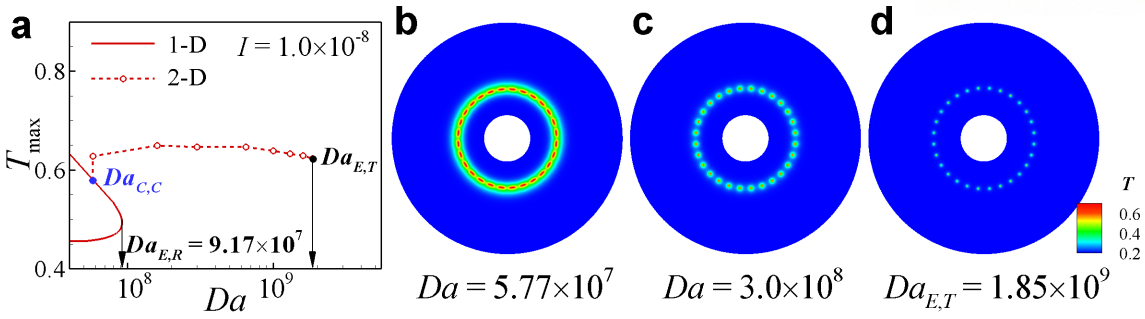

Figure 3.7: (a) The maximum flame temperature, $T_{\max}$, as a function of Damköhler number, Da, from the C-shaped IC for $I = 10^{-8}$ together with three representative temperature isocontours at (b) $Da = 5.77 \times 10^7$, (c) 3.0×10^8, and (d) 1.85×10^9.

by reducing their size as shown in Fig. 3.7. Even at very large Da, the energy gain by the focusing effect of fuel with small Le_F compensates for the energy loss by radiation such that the small flame cells can keep a balance between heat release and radiative heat loss, which is manifested by nearly constant $T_{\max}$ value regardless of Da. Therefore, the flame cells from the C-shaped IC survive beyond $Da_{E,R} = 9.17 \times 10^7$ up to global extinction at $Da_{E,T}$ as shown in the figure.

In fact, the flame cell size in the azimuthal direction, l_θ, generated from the C-shaped IC decreases gradually from 5.8 to $0.8 l_D$ as Da increases from 5.77×10^7 to $Da_{E,T} = 1.85\times10^9$. l_D is the diffusion length used for normalizing the coordinate directions in this chapter, and hence, it is unity by definition. Note that l_θ is measured by the full-width-half-maximum (FWHM) temperature. From an asymptotic analysis, Cheatham and Matalon [101] found that the flame cell sizes at the onset of instability are on the order of the diffusion length. More specifically, Metzener and Matalon [9, 88] reported that for planar diffusion flames, the characteristic cell size ranges from 3 to $12 l_D$. In this chapter, l_θ becomes less than l_D near $Da_{E,T}$. As mentioned above, this is primarily attributed to the shrinkage of the flame cells to survive significantly-large radiative heat loss beyond $Da_{E,R}$.

3.5 Flame Cell Dynamics with the C-shaped and Asymmetric IC's

Nanduri et al. [51] reported the existence of 2-D propagating cellular flames in counterflow configuration at Da beyond 1-D radiation-induced extinction limit, $Da_{E,R}$. In this section, therefore, we investigate the dynamics of flame cells which survive beyond $Da_{E,R}$ by performing 2-D simulations of opposed tubular flames with the C-shaped and asymmetric IC's. Propagating flame cells can be generated as follows; two IC's are generated from the 1-D steady solution at $Da_{E,P} = 6.27 \times 10^7$ and then, 2-D simulations with the IC's are performed at Da beyond $Da_{E,R}$ as well as $Da_{E,P}$.

Figure 3.8 shows the temporal evolution of edge flames originated from the C-shaped IC at $Da = 6.0 \times 10^8$ beyond $Da_{E,R} = 9.17 \times 10^7$. The initial C-shaped flame shrinks almost immediately after the start of the simulation due to excessive radiative heat loss. Meanwhile, two relatively-strong reaction fronts develop at both ends of the flame and a diffusion flame in the middle becomes weak as shown in Fig. 3.8a. Then, the flame splits into two edge flames which propagate towards each other (see Figs. 3.8b and c). Finally, they collide each other, leading to total extinction (see Figs. 3.8d). If an edge flame exists beyond $Da_{E,R}$ somehow as in Fig. 3.8, it loses its diffusion flame tail due to excessive radiative heat loss enough to extinguish the corresponding 1-D steady flame such that only its flame edge can survive, at which the reaction enhanced by both the focusing effect of fuel with small Le_F and large Da compensates for the excessive radiative heat loss. In addition, an edge flame has propagating characteristics by nature such that the edge flames developed from a cellular flame keep propagating toward unburned mixture with positive flame speed.

The dynamics of propagating edge flames is quantified by evaluating the propagation speed of the flame cells. The propagation speed of the edge flames is obtained by evaluating a displacement speed which measures the velocity of a scalar isocontour (e.g. temperature and fuel/oxidizer mass fractions) relative to local flow velocity. In this chapter, the azimuthal flow velocity is zero and hence, the displacement speed directly represents

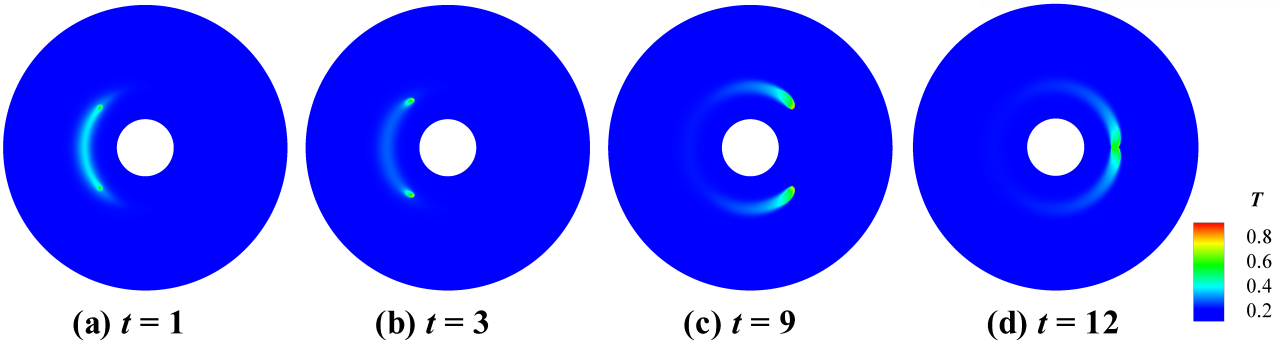

Figure 3.8: Temporal evolution of flame cells originated from the C-shaped IC at $Da = 6.0 \times 10^8$ with $I = 10^{-8}$: (a) $t = 1$, (b) 3, (c) 9, and (d) = 12.

the propagation speed of the edge flames along the azimuthal direction. In the context of constant density, the displacement speed, S_d, can be defined by [89–92, 94, 97, 100]:

$$S_d = S_d^R + S_{d,r}^D + S_{d,\theta}^D = \frac{1}{|\nabla T|}\left[\omega + \frac{1}{r}\frac{\partial}{\partial r}\left(r\frac{\partial T}{\partial r}\right) + \frac{1}{r^2}\frac{\partial^2 T}{\partial \theta^2}\right], \tag{3.9}$$

where S_d^R, $S_{d,r}^D$, and $S_{d,\theta}^D$ represent the net heat release or the sum of heat release and radiative heat loss, $r-$ and $\theta-$directional diffusion components of S_d, respectively. In this form, therefore, each component of the displacement speed is a measure of its corresponding contribution to the edge flame propagation. Note that in our previous study [100], it was found that S_d exhibits positive values when an edge flame is generated or propagates towards unburned mixture while negative S_d appears at locations where local extinction occurs.

Figure 3.9 shows the temperature isocontours of the edge flames and the corresponding 1-D profiles of the displacement speed and its components along the maximum heat release plane at different times. As discussed above, the reaction fronts in Fig. 3.9a have positive S_d while the diffusion flame in the middle exhibits negative S_d due to relatively-strong $r-$directional diffusion, which verifies that edge flames start to form at two flame edges and local flame quenching starts to occur in between. After that, two propagating edge flames exhibit large positive S_d at the front and large negative S_d at the rear (see Figs. 3.9b and c), which implies that the edge flames is composed of a thin relatively-strong reaction front and a relatively-weak reaction tail. At last, they are extinguished by the head-on collision, manifested in negative S_d throughout the flames (see Fig. 3.9d).

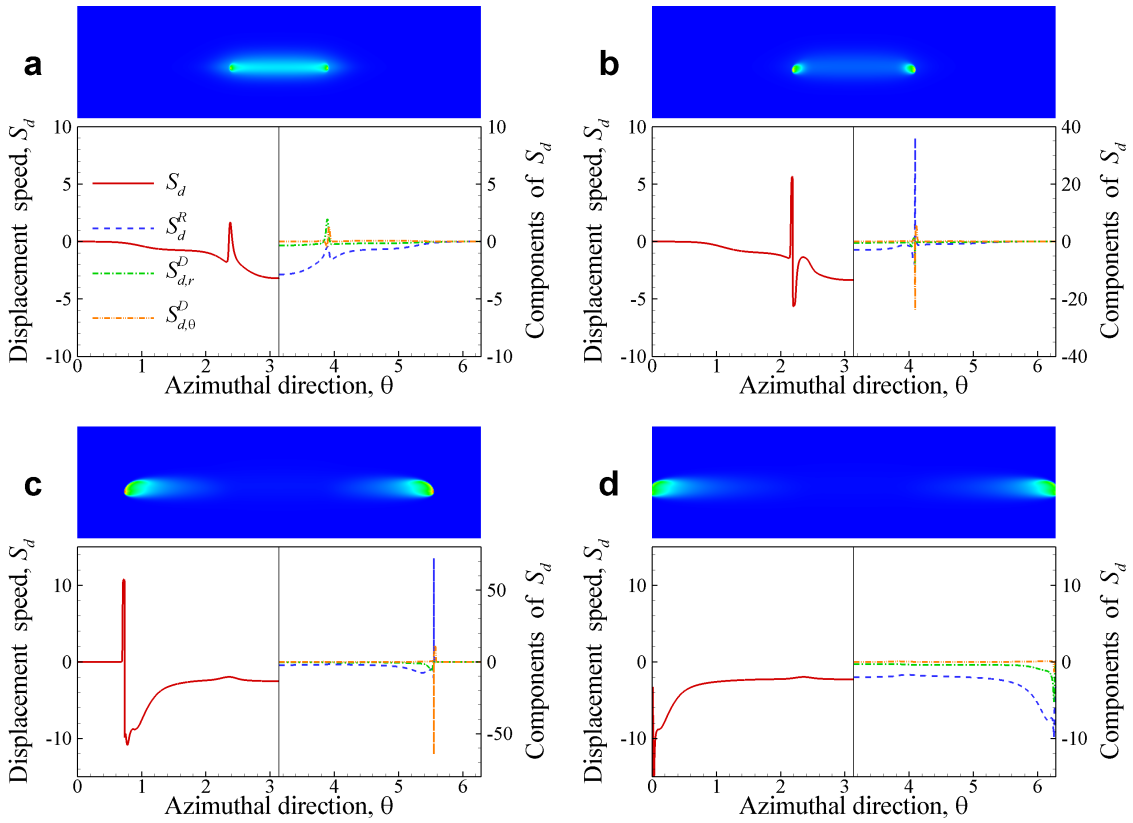

Figure 3.9: Temperature isocontours (top) and the corresponding 1-D profiles of the displacement speed, S_d, (left) and its components (right) along the maximum heat release plane (bottom) from two edge flames at $Da = 6.0 \times 10^8$ with $I = 10^{-8}$: (a) $t = 1$, (b) 3, (c) 9, and (d) 12.

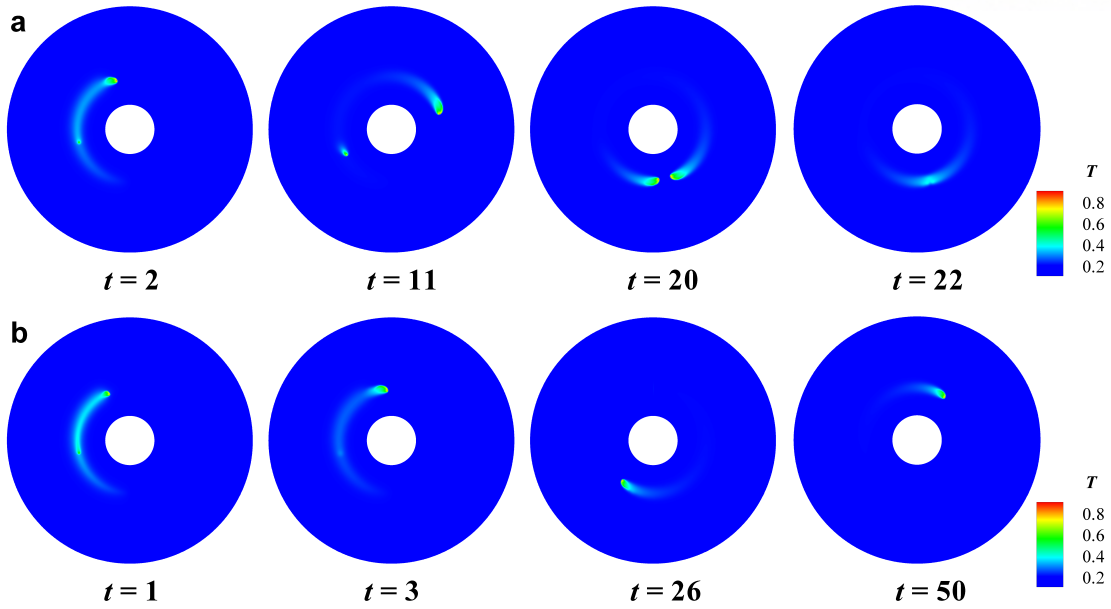

Figure 3.10: Temporal evolution of the tubular flames with the asymmetric IC at (a) Da = 5.0 $\times 10^8$ and (b) 6.0 $\times 10^8$ with $I = 10^{-8}$.

To verify the existence of a rotating edge flame, we performed additional 2-D simulations with the asymmetric IC. Figure 3.10 shows different snapshots of edge flames originated from the asymmetric IC at Da = 5.0 $\times 10^8$ and 6.0 $\times 10^8$. At Da = 5.0 $\times 10^8$, similar to the result with the C-shaped IC, two edge flames develop first from the asymmetric IC and total extinction occurs by their head-on collision. At Da = 6.0 $\times 10^8$, however, a relatively-weak reaction front fails to develop into an edge flame while a relatively-strong reaction front survives and keep rotating with constant propagation speed.

To further identify the characteristics of the rotating flame cell, the maximum flame temperature as a function of Da from the asymmetric IC are shown in Fig. 3.11. The displacement speed, S_d, and its components of the rotating flame cell are also shown in the figure. When Da is relatively low ($Da_{C,C} < Da \leq 1.0 \times 10^8$) and the consequent radiative heat loss is not high enough, a tubular flame with two edges develops first even from the asymmetric IC, subsequently evolving into a stationary cellular flame, similar to that in Fig. 3.7. When Da is relatively large ($1.0 \times 10^8 < Da \leq 5.7 \times 10^8$), two flame cells develop from the asymmetric IC and total extinction occurs by their head-on collision as shown in Fig. 3.10a. However, when Da is large enough (5.7 $\times 10^8 < Da \leq 1.5 \times 10^9$),

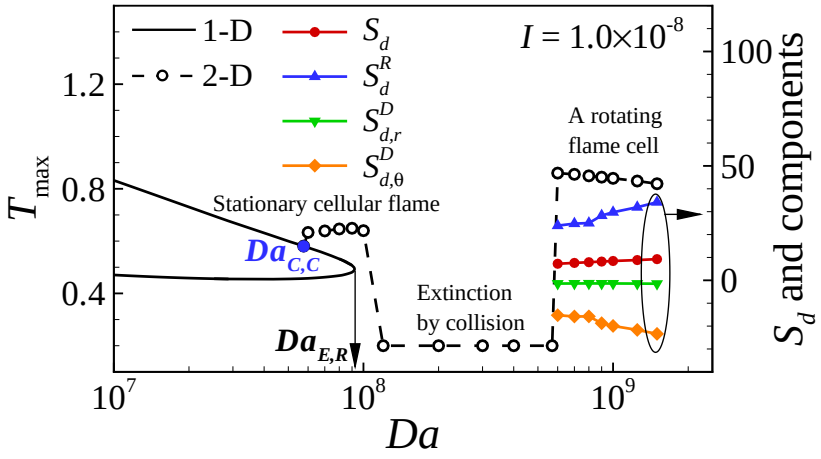

Figure 3.11: The maximum flame temperature, $T_{\max}$, as a function of Damköhler number, Da, from the asymmetric IC for $I = 10^{-8}$ together with the displacement speed and its components of rotating flame cells.

only a relatively-strong flame cell survives and keeps rotating as shown in Fig. 3.10b. When $Da > 1.5 \times 10^9$, however, the surviving flame cell becomes unstable due to large radiative heat loss and consequently, a small flame cell falls apart from it. Ultimately, the total extinction occurs by the head-on collision of two flame cells similar to that in Fig. 3.10a.

To elucidate the propagating characteristics of the rotating flame cells at high Da, we evaluated their steady displacement speed and its components as shown in Fig. 3.11. Note that they were measured at the maximum net heat release point using Eq. 3.9. It is readily observed from the figure that as Da increases from 6.0×10^8 to 1.5×10^9, S_d increases from 7.244 to 9.260 due to the increase of S_d^R. In this regime, the size of the rotating flame cell decreases with Da and as such, the focusing effect of fuel with small Le_F is enhanced, which increases both of the maximum local heat release and the consequent S_d^R. However, $T_{\max}$ is slightly decreased from 0.862 to 0.819 by large radiative heat loss despite the increase of the maximum local heat release. These results imply that the rotating flame cell can survive such large radiative heat loss by reducing its size and consequently increasing its local heat release and flame speed.

3.6 Effects of Extremely-high Radiative Intensity

As shown in Fig. 3.1b, $Da_{E,S}$ increases slightly and $Da_{E,R}$ decreases significantly with increasing I from 10^{-9} to 10^{-7}. In the case of an extremely-high radiative intensity (i.e. $I = 3.7 \times 10^{-7}$), however, the radiative heat loss significantly affects tubular flames such that the combustible regime considerably shrinks and $Da_{E,S}$ (= 37363) becomes comparable to $Da_{E,R}$ (= 112500). This result implies that the radiative intensity of 3.7×10^{-7} is high enough to affect the flame instability characteristics near both stretch-induced and radiation-induced extinction limits. In this section, therefore, we elucidate the characteristics of flame instabilities of opposed tubular flames under the extremely-high radiative intensity condition by performing 2-D numerical simulations with the perturbed IC. The results are compared to those of the linear stability analysis.

Figure 3.12 shows the temporal evolution of $T_{\max}$ at different Da, and the corresponding regime diagram of the flame response to the perturbed IC for $I = 3.7 \times 10^{-7}$. Two points are to be noted. First, the D-T and/or oscillatory instabilities occur through the whole combustible regime because tubular flames with extremely-large radiative heat loss become more vulnerable to flame instabilities. More specifically, the flame response to the perturbed IC is divided into three different regimes: the total extinction by growing oscillation (Regime IV) occurs when Da is less than 38050 and greater than 94800; the cellular flame with decaying oscillation (Regime II) appears between Da = 38732 and 88600; the cellular flame with growing oscillation (Regime III) occurs between Regime II and IV (see Fig. 3.12c).

Second, the number of flame cells in 2-D simulations changes from 10 to 12 with increasing Da from 38050 to 94800, according to $k_{\max}$ value of the linear stability analysis which varies from 10.0 to 11.9. Moreover, the decaying and growing oscillation behaviors of 2-D tubular flames also agree well with the results of the linear stability analysis as discussed in Sec. 3.2. Note that when the radiative intensity is significantly high, even high-stretched tubular flames are influenced by radiative heat loss such that the oscillatory instability appears even at low Da and the D-T instability occurs for tubular flames that survive within the combustible regime. It implies that under extremely-large radiative

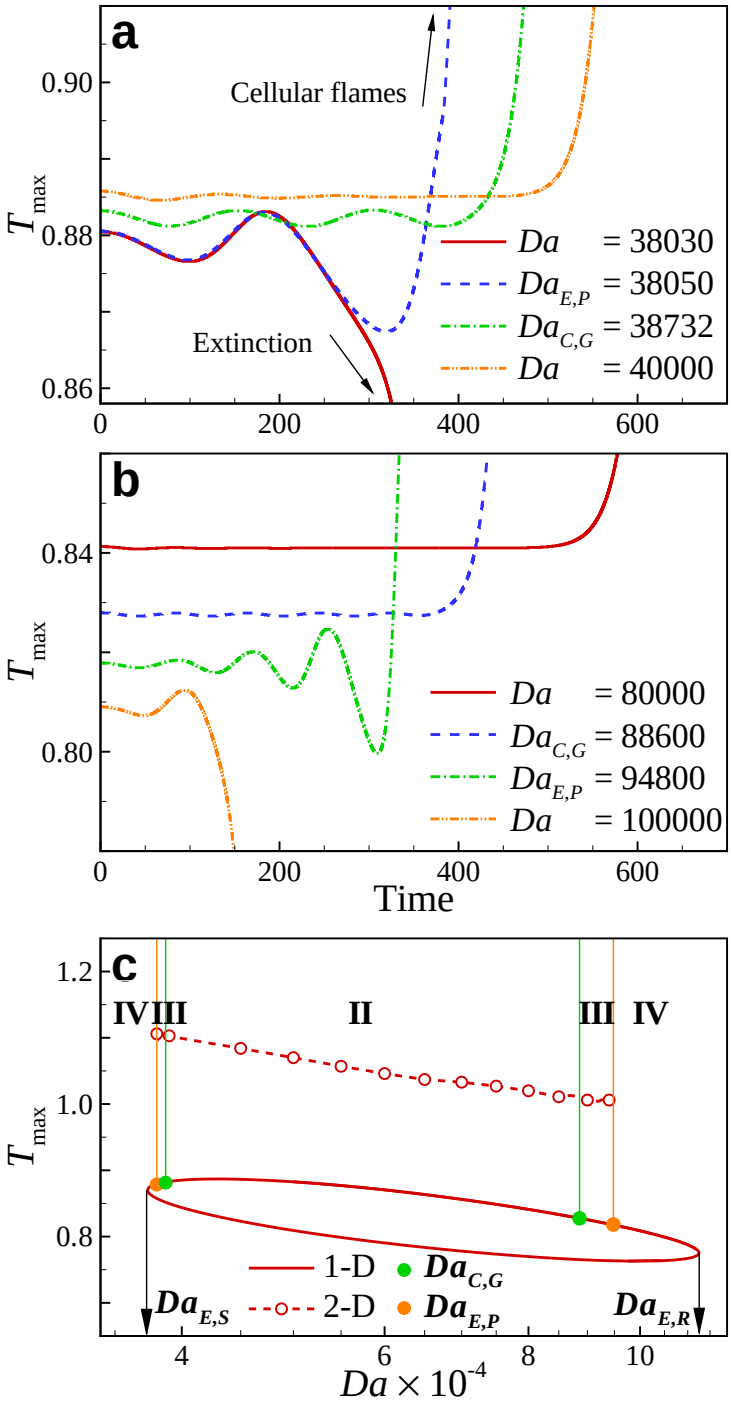

Figure 3.12: Temporal evolution of the maximum flame temperature, $T_{\max}$, at (a-b) different Damköhler numbers, Da, and (c) the corresponding regime diagram of the flame response to the perturbed IC for an extremely high radiative intensity, $I = 3.7 \times 10^{-7}$: II – a cellular flame with decaying oscillation, III – a cellular flame with growing oscillation, and IV – total extinction with growing oscillation.

heat loss, an opposed non-premixed tubular flame with low Le_F can survive only in the form of a cellular flame regardless of Da.

3.7 Conclusions

The flame instabilities and flame cell dynamics of opposed non-premixed tubular flames with radiative heat loss are investigated using 2-D numerical simulations with the linear stability analysis. To identify the effects of disturbance magnitude and shape of the initial conditions, three different initial conditions, (i.e. the perturbed IC, the C-shaped IC, and the asymmetric IC), are applied in the 2-D simulations. The budget analysis and displacement speed analysis are used to elucidate the characteristics of the flame cell structure and dynamics. In addition, the flame instabilities of tubular flames under extremely-high radiative intensity condition are also identified. The results in present study can be summarized as follows:

1. From 2-D numerical simulations with the perturbed IC, the flame response to the initial perturbation near the radiation-induced extinction limit, $Da_{E,R}$, is divided into four different regimes: (1) Regime I – a noncellular flame with decaying oscillation, (2) Regime II – a cellular flame with decaying oscillation, (3) Regime III – a cellular flame with growing oscillation, and (4) Regime IV – total extinction with growing oscillation.

2. From the linear stability analysis, the critical Damköhler numbers including $Da_{C,D}$, $Da_{C,C}$, and $Da_{C,G}$ that delineate the regime boundaries can be identified; they show good agreement with those from the 2-D simulations with the perturbed IC.

3. The radiation effects on flame structure are elucidated by examining the transport budgets of flame cells at both the stretch-induced extinction limit, $Da_{E,S}$, and 2-D radiation-induced extinction limit, $Da_{E,P}$. The comparison verifies that the radiative heat loss reduces the flame cell temperature at $Da_{E,P}$ despite both the large heat release due to significantly-large Da and the focusing effect of fuel with small Le_F due to the small cell size with large curvature.

4. From 2-D simulations with the C-shaped IC, it is found that once flame cells appear through the D-T instability near $Da_{C,C}$, they survive until total extinction occurs at $Da_{E,T}$ beyond $Da_{E,R}$. Meanwhile, the number of flame cells remains the same and the flame cell size continually decreases with increasing Da.

5. A tubular flame with the C-shaped IC splits into two propagating flame cells within the range of sufficiently-large Da beyond $Da_{E,R}$. The two flame cells lead to total extinction through the head-on collision. However, a rotating flame cell can be observed from a tubular flame with the asymmetric IC because a relatively-weak reaction front fails to develop into another rotating flame cell.

6. From the displacement speed, S_d, analysis, it is found that the propagating edge flame exhibits large positive S_d at the front and large negative S_d at the rear, which indicates that it is composed of a thin strong reaction front and a relatively-weak reaction tail.

7. Under the extremely-high radiative intensity condition, the D-T and/or oscillatory instabilities appear through the whole combustible regime such that tubular flames can survive only in the form of a cellular flame regardless of Da.

Chapter IV

Estimation of the NO_X Emission of Counterflow Non-premixed Flames under Supercritical Oxy-fuel Combustion Conditions

Apart from the previous chapters handling flame instabilities of opposed non-premixed tubular flames at atmospheric pressure, we will discuss the fundamental characteristics of counterflow non-premixed flames under supercritical oxy-fuel combustion conditions. The additional objective of the present study is to investigate the NO_X emission characteristics by performing one-dimensional numerical simulations with various N_2 amount in the fuel and oxidizer streams. The NO_X emission characteristics are further elucidated by separating the relative contributions of NO_X formation pathways such as thermal NO_X, prompt NO_X, and N_2O pathways, and the NO_X consumption pathway via reburn reactions (NO_X reburn mechanism) [56–59, 102].

4.1 Numerical Methods

To investigate the NO_X emission characteristics of the sCO_2 oxy-fuel combustion, one-dimensional numerical simulations of CH_4 versus O_2/CO_2 counterflow non-premixed

flames in an axisymmetric opposed jet configuration are performed using the OPPDIF [103] code with detailed chemical mechanisms. To take into account real gas effects, we adopt a modified Soave-Redlich-Kwong equation of state [104, 105] that is valid over a wide range of fluid conditions. Thermodynamic properties are expressed as a sum of an ideal reference value calculated from the CHEMKIN package [82] and a departure function incorporating real gas effects [106]. Dynamic viscosity and thermal conductivity are calculated using Chung's high pressure model [107], and binary mass diffusion coefficients at high pressure condition are estimated with Takahashi's model [108]. For the validation of the models, we compare the properties with those of NIST REFPROP data [1], which verifies that the present general-fluid models capture real gas behaviors reasonably well in a broad range of thermodynamic conditions. Figures 4.1– 4.3 show the density, specific heat, dynamic viscosity, and thermal conductivity of methane, oxygen, and carbon dioxide molecules at various temperature and pressure conditions. As shown in figures, all of the thermophysical properties calculated from the present numerical methods (i.e., lines in figures) agree well with the NIST data (i.e., symbols in figures), demonstrating that the real gas models are appropriate to analyze the flame structure under the sCO_2 oxy-fuel combustion condition.

For the present study, the San Diego mechanism with NO_X formation [59, 109] is adopted because it can describe reactions at relatively-high pressures. Since the San Diego mechanism is not validated against experiments at high pressures, we compare its flame temperature and major species profiles against those of USC-II [110] and AramcoMech mechanisms [111] at various conditions, which verifies that they are quantitatively in good agreement.

For the boundary conditions, the momentums of the fuel and oxidizer streams are identical to each other (i.e., $\rho_F {U_F}^2 = \rho_O {U_O}^2$) so that the stagnation point is located in the middle of the domain. The global strain rate, a, is used to characterize flow and flame, which is defined as $a = (|U_F| + |U_O|)/H$, where ρ is the density, U, the axial velocity, and H of 5.0 cm the distance between two inlets. The subscripts F and O represent the fuel and oxidizer streams, respectively. O_2 at the oxidizer stream is highly diluted with CO_2, thereby the mole fraction of O_2, X_{O_2}, varies from 0.15 to 0.30. As mentioned above,

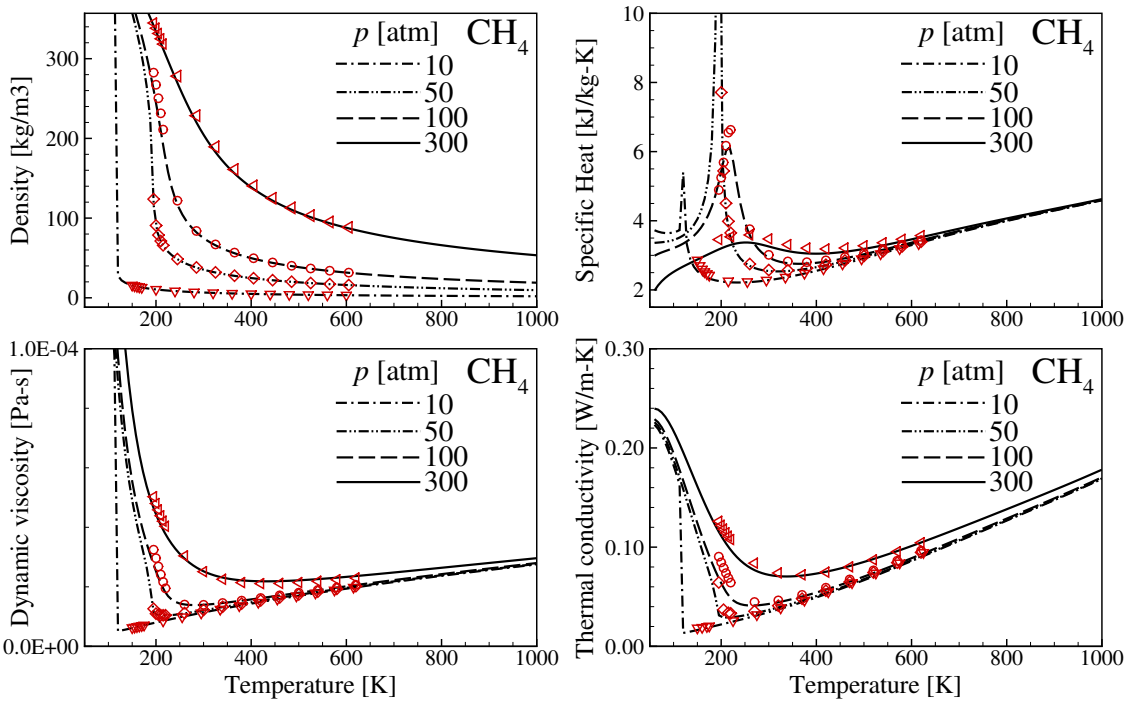

Figure 4.1: Validations of density, thermodynamic and transport properties of methane against NIST data [1] at various temperature and pressure conditions. Lines and symbols in figure represent the data obtained from the present numerical simulation and the NIST data, respectively.

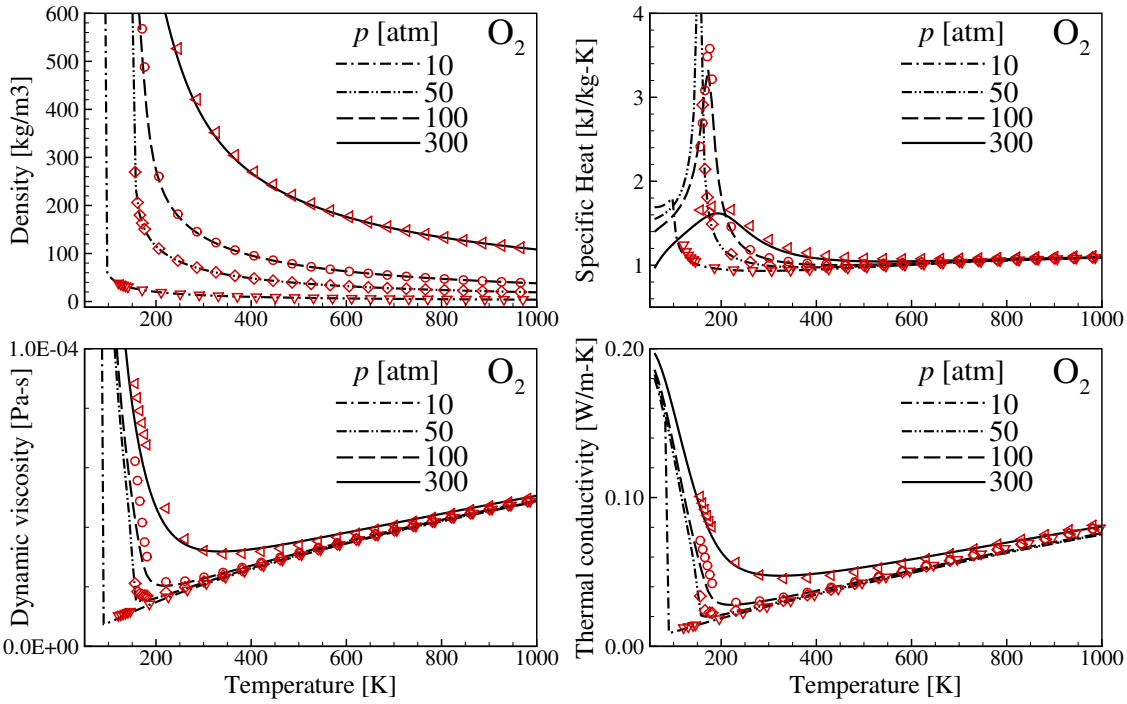

Figure 4.2: Validations of density, thermodynamic and transport properties of oxygen against NIST data [1] at various temperature and pressure conditions. Lines and symbols in figure represent the data obtained from the present numerical simulation and the NIST data, respectively.

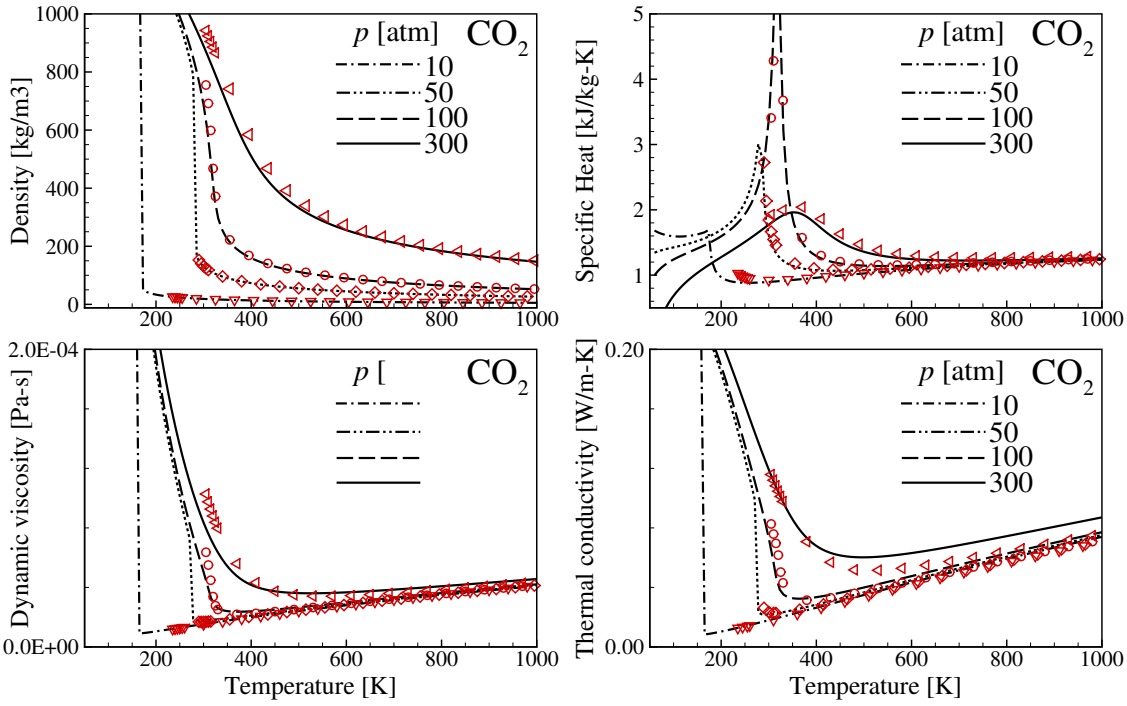

Figure 4.3: Validations of density, thermodynamic and transport properties of carbon dioxide against NIST data [1] at various temperature and pressure conditions. Lines and symbols in figure represent the data obtained from the present numerical simulation and the NIST data, respectively.

both fuel and oxidizer streams can include N_2, and hence, the amount N_2 is assumed to vary up to 10% by volume in pure methane fuel stream or O_2/CO_2 oxidizer stream. As such, the effect of N_2 amount in the fuel/oxidizer stream, $X_{N_2,F}/X_{N_2,O}$, can be compared. Pressure, p, is set to 300 atm unless otherwise stated, and the inlet temperatures of fuel and oxidizer streams are fixed to 300 and 1000 K, respectively. Most of these boundary conditions are in accordance with the design conditions of the non-premixed combustor for a direct-fired sCO_2 power system [54].

Note that there exist no reliable radiation models for mixtures with large X_{CO_2} at extremely-high pressures, and hence, we exclude the radiative heat loss, $\dot{q}_r$, from the simulations rather than including another uncertainty. To demonstrate our assumption, the thermal radiation effect under identical conditions is estimated, and this study is described in the next chapter.

4.2 Results and Discussions

4.2.1 Overall Flame Characteristics

Figure 4.4 shows the temperature profiles of CH_4 versus O_2/CO_2 counterflow non-premixed flames for various a and p. As readily observed from Fig. 4.4a, both the flame thickness, δ_f, and the maximum flame temperature, T_f, decrease with increasing a due to reduced residence time within the flame and subsequent reactant leakage. As p increases (see Fig. 4.4b), δ_f decreases significantly due to the momentum increase of the fuel and oxidizer streams for a given a. However, T_f increases first from 1957 to 2276 K within $p = 1 \sim 100$ atm and then levels off. This is primarily because radical recombination reaction rates increase with increasing pressure and are balanced with chain-branching reactions at high pressures [102].

To compare the NO_X formations of the sCO_2 oxy-fuel combustion and typical air-fuel combustion relevant to conventional gas-turbine, the structures of CH_4 versus O_2/CO_2 counterflow flame at $p = 300$ atm and CH_4/CO_2 versus air counterflow flame at $p = 30$ atm are shown in Fig. 4.5. For fair comparison, T_f are specified to be nearly identical by

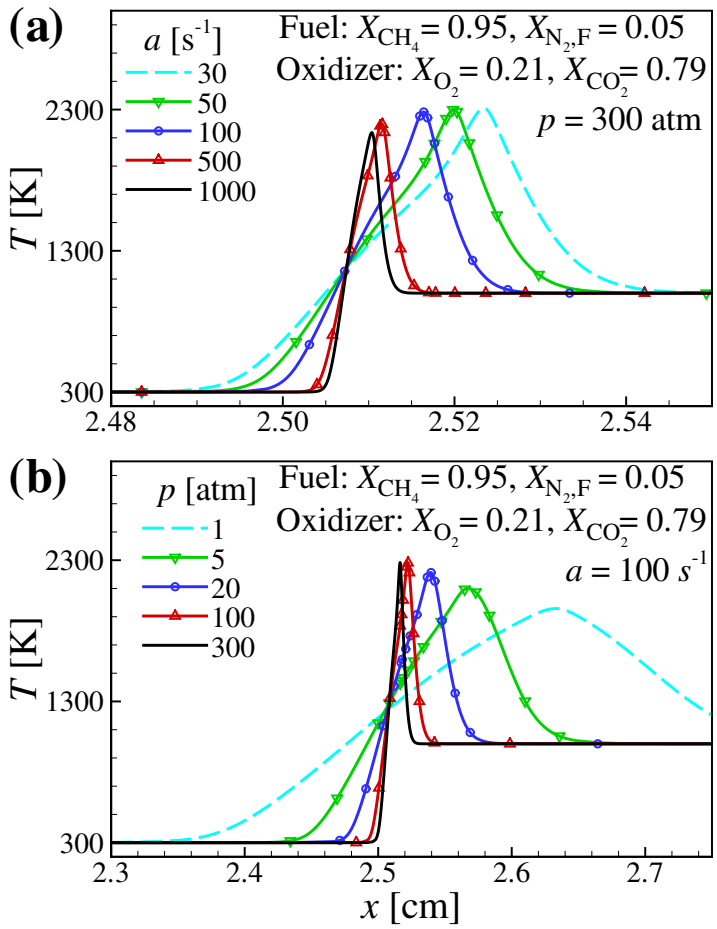

Figure 4.4: Temperature profiles of CH_4 versus O_2/CO_2 counterflow non-premixed flames for (a) various global strain rates and (b) various pressures. The fuel stream is $X_{CH_4} = 0.95$ and $X_{N_2,F} = 0.05$ and the oxidizer stream is $X_{O_2} = 0.21$ and $X_{CO_2} = 079$.

diluting the fuel stream with CO_2 for the air-fuel combustion case. It is readily observed that the temperature profiles of two flames are similar to each other despite their different δ_f. For both cases, the peak X_{NO} occurs at the location of T_f while NO_2 formation is negligible compared to that of NO. However, the peak X_{NO} of the oxy-fuel combustion is two orders of magnitude lower than that of the air-fuel combustion despite their nearly-identical T_f, which cannot be solely explained by the difference between $X_{N_2,O}$ in the air-fuel combustion and $X_{N_2,F}$ of the oxy-fuel combustion because $X_{N_2,O}/X_{N_2,F}$ is just $O(10)$. This is closely related to the dependence of NO_X formation on which stream includes N_2. Furthermore, X_{NO} for the oxy-fuel combustion drastically decreases from its peak at the fuel-rich zone, while that for the air-fuel combustion exhibits relatively smooth decrease at that zone. This implies that since the prompt NO_X and/or NO_X reburn reactions usually occur at fuel-rich zone [59], their relative contributions to the overall NO_X emission can be different under the oxy-fuel and air-fuel combustion conditions. The above characteristics of NO_X emission will be further discussed in the following two sections.

4.2.2 Effect of N_2 amount in Fuel and Oxidizer Streams

As mentioned earlier, a small amount of N_2 can be included in both fuel and oxidizer streams in the sCO_2 oxy-fuel combustion. Therefore, here we investigate the effect of $X_{N_2,F}$ and $X_{N_2,O}$ on the NO_X formation at various conditions by adopting the emission index of NO_X, $EINO_X$, that represents the amount of NO_X generation per unit fuel consumption, which is defined by [112]:

$$\mathrm{EINO_X} = \frac{\int_0^H (\dot{\omega}_{NO} W_{NO} + \dot{\omega}_{NO_2} W_{NO_2}) dx}{-\int_0^H \dot{\omega}_{CH_4} W_{CH_4} dx}, \tag{4.1}$$

where x is the axial distance from the fuel inlet, and $\dot{\omega}_k$ and W_k are the production rate and molecular weight of species k, respectively. Figure 4.6 shows the variations of $EINO_X$ as a function of $X_{N_2,F}$ and $X_{N_2,O}$ for various X_{O_2}. Three points are noted.

First, the variation of $EINO_X$ is more sensitive to X_{O_2} than $X_{N_2,F}$ and $X_{N_2,O}$. This is because T_f increases significantly with increasing X_{O_2} while it does not change much with X_{N_2}: the maximum difference in T_f, $\delta T_{f,max}$, among the flames with different X_{O_2} is greater than 850 K, while $\delta T_{f,max}$ for different X_{N_2} is less than 50 K. In general, thermal

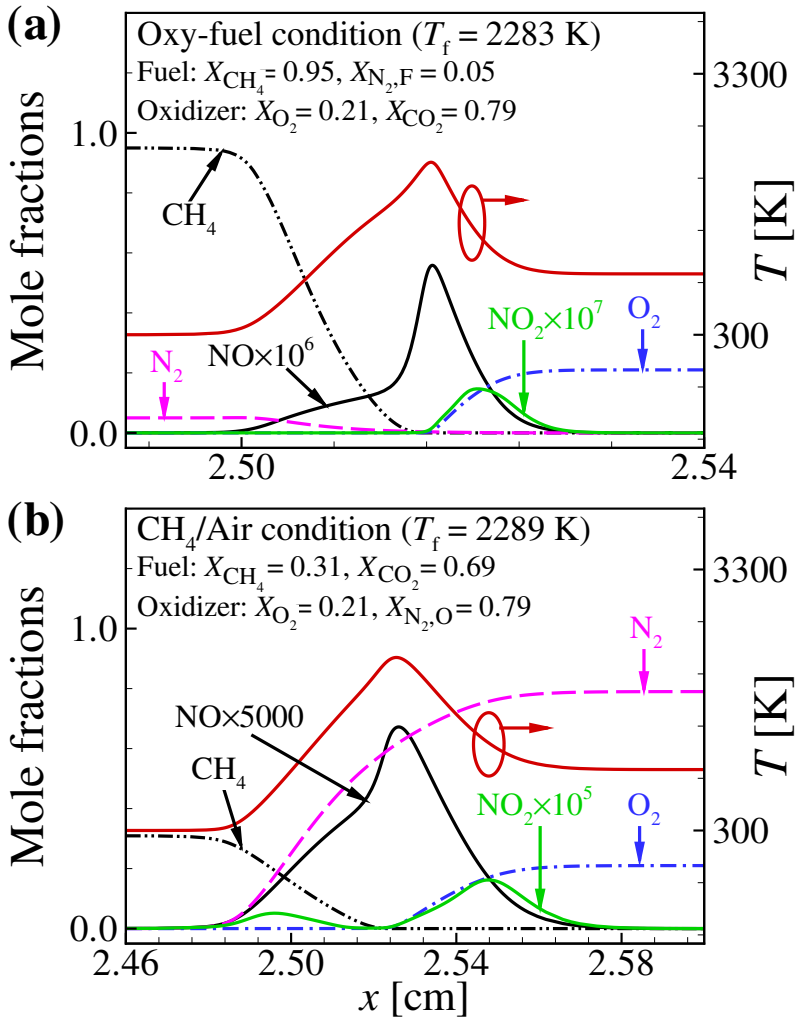

Figure 4.5: Profiles of temperature and mole fractions of important species for (a) CH_4 versus O_2/CO_2 counterflow non-premixed flames ($X_{N_2,F} = 0.05$ and $X_{O_2} = 0.21$) at 300 atm and (b) CH_4/CO_2 versus air counterflow non-premixed flame ($X_{CO_2,F} = 0.69$) at 30 atm. For both cases, $a = 100\ s^{-1}$.

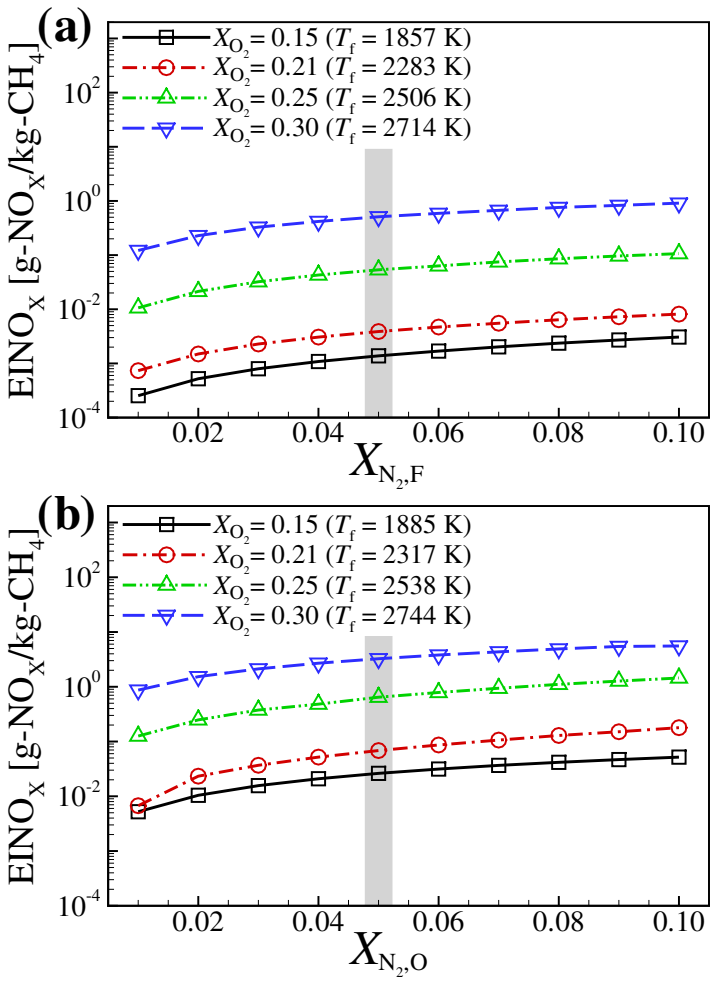

Figure 4.6: EINO$_X$ of CH_4 versus O_2/CO_2 counterflow non-premixed flames as a function of (a) $X_{N_2,F}$ and (b)$X_{N_2,O}$ for various X_{O_2} at p = 300 atm and a = 100 s^{-1}. T_f are evaluated for the flames with $X_{N_2,F}$ = 0.05 and $X_{N_2,O}$ = 0.05 (highlighted in grey).

NO_X increases significantly with increasing T_f, and hence, high T_f induces more NO_X emission.

Second, $EINO_X$ from $X_{N_2,F}$ remains extremely low when approximately $T_f < 2300$ K regardless of $X_{N_2,F}$ (see Fig. 4.6a), which is negligible compared to that from the air-fuel combustion at 30 atm. For instance, the $EINO_X$ of the oxy-fuel combustion with $X_{O_2} = 0.21$ at 300 atm is 0.001–0.008 g-NO_X/kg-CH_4 depending on $X_{N_2,F}$ (see the dash-dotted line in Fig. 4.6a) while that of the air-fuel combustion at 30 atm (the case in Fig. 4.5b) is found to be 2.43 g-NO_X/kg-CH_4. However, the $EINO_X$ of the oxy-fuel combustion becomes comparable to that of the air-fuel combustion when X_{O_2} is large enough to raise T_f to approximately 2700 K. Note that according to tests for an sCO_2 oxy-fuel combustor [54], T_f can increase to 2750 K, and hence, NO_X emission should be taken into account for the design of the sCO_2 oxy-fuel combustor although natural gas contains only a small amount of N_2.

Third, $EINO_X$ from $X_{N_2,O}$ is an order of magnitude larger than that from $X_{N_2,F}$ at given X_{O_2}, and becomes comparable to that of the air-fuel combustion at 30 atm when approximately $T_f > 2500$ K. Since T_f difference between cases with $X_{N_2,F}$ and $X_{N_2,O}$ is marginal, this result also indicates the dependence of NO_X generation on which stream contains N_2.

To precisely examine the NO_X emission characteristics depending on which stream includes N_2, we adopt a pseudo species of nitrogen, PN_2, that has the same thermodynamic and transport properties as N_2 but does not participate in any chemical reactions. Three different cases are performed: for a baseline case, 5% of N_2 is included in both streams; for two other cases, one of two streams include 5% of N_2 while the other stream does 5% of PN_2. By replacing N_2 with PN_2 in each stream, we can effectively estimate the effect N_2 ingress on the NO_X emission while keeping their T_f nearly identical. Note that unlike previous cases, we specify the same inlet temperature of 1000 K for both streams to eliminate their effect on the NO_X emission. The variations of $EINO_X$ and flame structures for three different cases are shown in Fig. 4.7.

From Fig. 4.7a, we can readily identify that for the case with N_2 in both streams, most of NO_X emission originates from NO_X generated by N_2 in the oxidizer stream, and

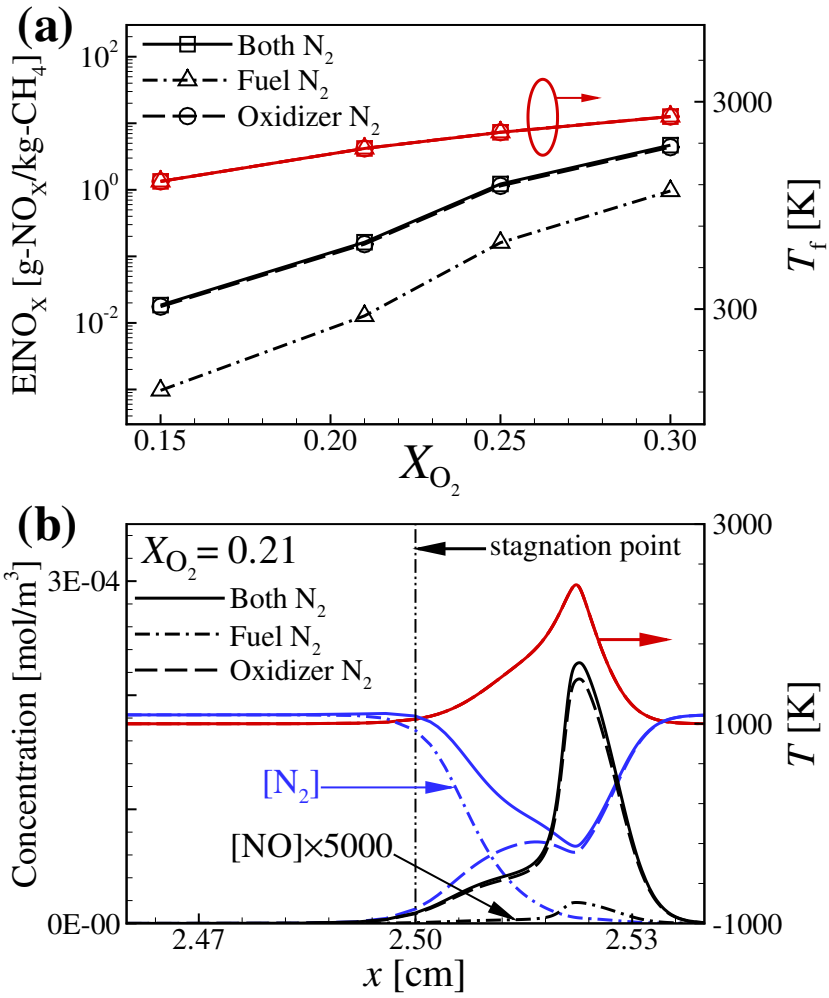

Figure 4.7: (a) $EINO_X$ and T_f as a function of X_{O_2} and (b) the profiles of N_2 and NO concentrations, and temperature for CH_4 versus O_2/CO_2 counterflow non-premixed flames with $X_{O_2} = 0.21$ at 300 atm and $a = 100\ s^{-1}$ for three different cases of N_2 ingress in both streams, in the fuel stream only, and in the oxidizer stream only, for all of which X_{N_2} or $X_{PN_2} = 0.05$.

is approximately an order of magnitude larger than that for the case with N_2 in the fuel stream, similar to the results in Fig. 4.6. To understand the discrepancy of $EINO_X$ between the cases, the profiles of N_2 and NO concentrations and temperature for three cases with $X_{O_2} = 0.21$ are shown in Fig. 4.7b. Since the flame lies in the oxidizer side relative to the stagnation point, the transport of N_2 in the fuel stream to the reaction zone occurs only through the diffusion process. Consequently, N_2 concentration in the flame zone for the case with N_2 in the fuel stream is much lower than that for the case with N_2 in the oxidizer stream, leading to the significant difference of NO_X formation between two cases. In this regard, NO_X emission difference between two N_2-ingress scenarios for the counterflow non-premixed flames can be mitigated as the global equivalence ratio based on the mass flow rate of two inlets, ϕ, approach the stoichiometry because the flame with $\phi = 1$ lies closer to the stagnation point [56]. Nonetheless, we believe that in a practical non-premixed sCO_2 oxy-fuel combustor, vigorous reaction occurs at the mixing layer where a relatively-high speed fuel jet meets a relatively-low speed oxidizer jet, and hence, its combustion condition is more similar to that of the present simulations. These results imply that the suppression of NO_X emission from the sCO_2 oxy-fuel combustion can be primarily achieved by prohibiting N_2 from infiltrating the ASU.

4.2.3 NO_X Reaction Pathway Analysis

We further elucidate the NO_X emission characteristics under the sCO_2 oxy-fuel combustion conditions by analyzing the NO_X formation/consumption pathways. In conventional hydrocarbon/air flames, the reaction pathways of NO_X formation are mainly composed of four different routes: thermal NO_X , prompt NO_X , N_2O , and NNH pathways while NO_X reburn process is the major NO_X consumption pathway [59]. Through thermal, prompt, and N_2O initiation reactions, N_2 is first decomposed and converted into N, HCN, and N_2O, which react with other species to form NO. Some of NO generated from the NO_X formation pathways is then converted into NO_2 or is consumed via NO_X reburn pathways. Meanwhile, a certain amount of nitrogenous species generated from the NO_X reburn pathways return to NO_X through several reaction pathways. Therefore, here we adopt the

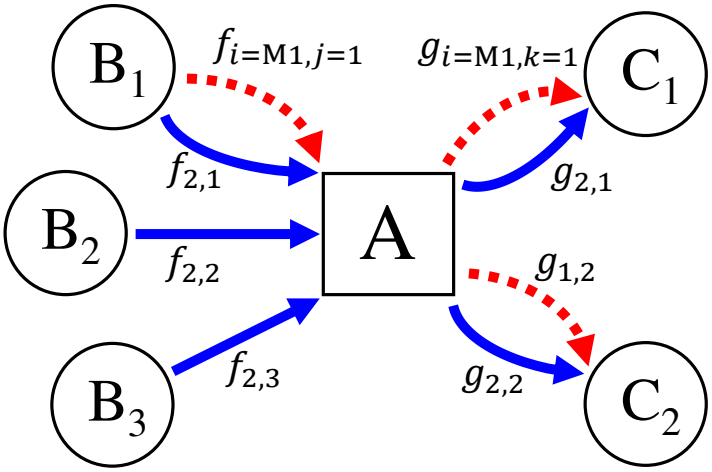

Figure 4.8: Schematic diagram for tracing nitrogen flux through species A [2].

same reaction pathways of NO_X formation/consumption to further elucidate the NO_X emission characteristics under the sCO_2 oxy-fuel combustion conditions. Since the NO_X formation via NNH pathway is negligible at high pressures [58], NNH pathway is not addressed here. The initiation reactions for each NO_X formation/consumption pathway adopted in the study is summarized in Table 1.

We evaluate the relative contribution of each NO_X reaction pathway to the NO_X formation by tracing the origin of NO_X, based on the approach in [2]. For this purpose, the net reaction rates between all nitrogenous species are numerically integrated along the x-direction, which represents the net reaction flux between any two species. Then, a hierarchical structure is generated for each species to analyze all pathways leading to the formation/consumption of the species, which is illustrated in Fig. 4.8.

The flux from species A to C_k originated from i-th NO_X formation pathway, $g_{i,k}$, is expressed by:

$$g_{i,k} = G_k \frac{\sum_j f_{i,j}}{\sum_{i,j} f_{i,j}}, \tag{4.2}$$

where the indices i, j, and k correspond to NO_X formation pathways, reactant species, and product species, respectively. G_k is the net reaction flux between species A and C_k. $f_{i,j}$ represents the reaction flux from species j to A through i-th NO_X formation pathway. By tracing all the NO_X formation reaction fluxes, we can reasonably distinguish the relative contribution of each NO_X formation pathway to the NO_X emissions. Note that the sum

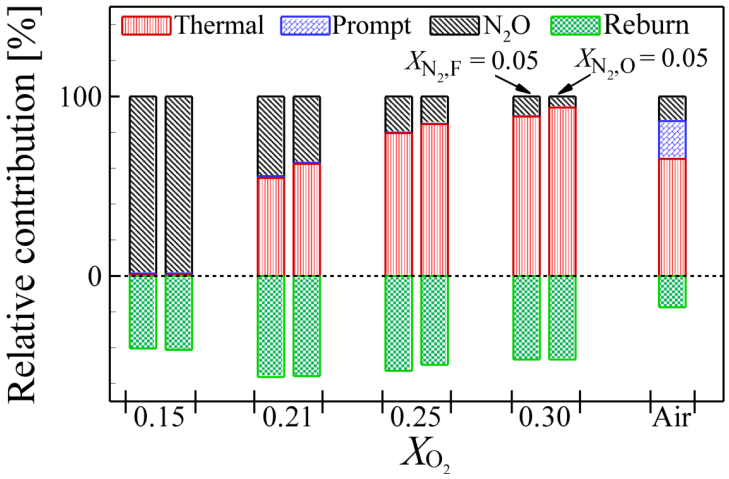

Figure 4.9: The relative contribution of each NO_X formation pathway to NO_X emission for CH_4 versus O_2/CO_2 counterflow non-premixed flames as a function of X_{O_2} at 300 atm and $a = 100\ s^{-1}$ and that for CH_4/CO_2 versus air counterflow non-premixed flame at 30 atm and $a = 100\ s^{-1}$. $X_{N_2,F} = X_{N_2,O} = 0.05$.

of NO_X formation reaction fluxes attributable reburn initiation pathways indicates the amount of NO_X which is converted back from the initial NO_X reburn route. Therefore, the relative contribution of "net" reburn pathway on NO_X consumption can be evaluated by (sum of NO_X formation reaction fluxes originated from the reburn initiation reactions) – (sum of reaction fluxes for the reburn initiation reactions), which is always a negative value.

Figure 4.9 shows the relative contribution of each NO_X formation pathway to the NO_X emission for CH_4 versus O_2/CO_2 counterflow non-premixed flames as a function of X_{O_2}. Those of the conventional CH_4/air counterflow flame at 30 atm in Fig. 4.5b are also shown in the figure. $X_{N_2,F}$ and $X_{N_2,O}$ are set to 0.05. Several points are noted.

First, for the oxy-fuel combustion, the N_2O pathway is the most dominant NOX emission pathway at relatively-low X_{O_2} while the contribution of thermal NO_X dominates over that of the N_2O pathway with increasing X_{O_2} or T_f. In addition, the prompt NO_X pathway is found to be negligible under the oxy-fuel combustion conditions, which is contrast to the air-fuel combustion at moderate pressure. As pressure increases, recombination reactions including $CH_3 + H + M \rightarrow CH_4 + M$ and $CH_3 + CH_3 + M \rightarrow C_2H_6 + M$

are enhanced, which inhibits the formation of small hydrocarbon radicals such as CH and CH_2 [113]. Moreover, CH_2 is more consumed via $CO_2 + CH_2 \rightarrow CO + CH_2O$ with increasing pressure under CO_2-rich conditions. As a result, the main formation of CH through $OH + CH_2 \rightarrow H_2O + CH$ is significantly reduced, leading to a reduction of its peak concentration by an order of magnitude as the pressure increases from 1 to 300 atm. Since the concentration of CH is too low to initiate the prompt NO_X route via $CH + N_2 \rightarrow HCN + N$ under the sCO_2 oxy-fuel condition, the NO_X emission via the prompt NO_X pathway becomes negligible under high pressures.

Second, the relative contribution of each NO_X formation pathway between cases with $X_{N_2,F}$ and $X_{N_2,O}$ are almost the same despite $O(10)$ differences in $EINO_X$ (see Fig. 4.7a), which substantiates that the increase of NO_X emission by N_2 ingress in the oxidizer stream is attributed to the amount of N_2 at the flame zone rather than thermo-chemical effects, as discussed above.

Third, the contribution of the reburn pathway to the total NO_X formation becomes significant under the sCO2 oxy-fuel combustion condition, compared to that of the air-fuel combustion at 30 atm. For instance, the relative contributions of the reburn pathway for the oxy-fuel combustion with $X_{O_2} = 0.21$ and $X_{N_2,F} = 0.05$ and the air-fuel combustion are approximately 56 and 17%, respectively, although their T_f are nearly identical. This is primarily because the peak concentrations of major reactants for NO_X reburn initiation reactions such as NO, HCCO, and CH_3 increase monotonically with increasing pressure, leading to an increase of the net reaction fluxes of NO_X reburn initiation. Furthermore, the reduction of C and H radicals at high pressure condition suppresses the NO_X formation reactions originated from NO_X reburn initiation reactions, which also serves to the increase of net NO_X reburn efficiency [59].

To understand the effect of pressure on the NO_X emission characteristics, the $EINO_X$ and the relative contribution of three major NO_X formation and NO_X reburn pathways as a function of pressure for CH_4 versus O_2/CO_2 counterflow non-premixed flames with $X_{N_2,F} = 0.05$ and $X_{O_2} = 0.21$ at $a = 100\ s^{-1}$ are shown in Fig. 4.10. Since the relative contributions of each NO_X formation pathway for cases with $X_{N_2,F}$ and $X_{N_2,O}$ are similar to each other, only the case with $X_{N_2,F}$ is investigated.

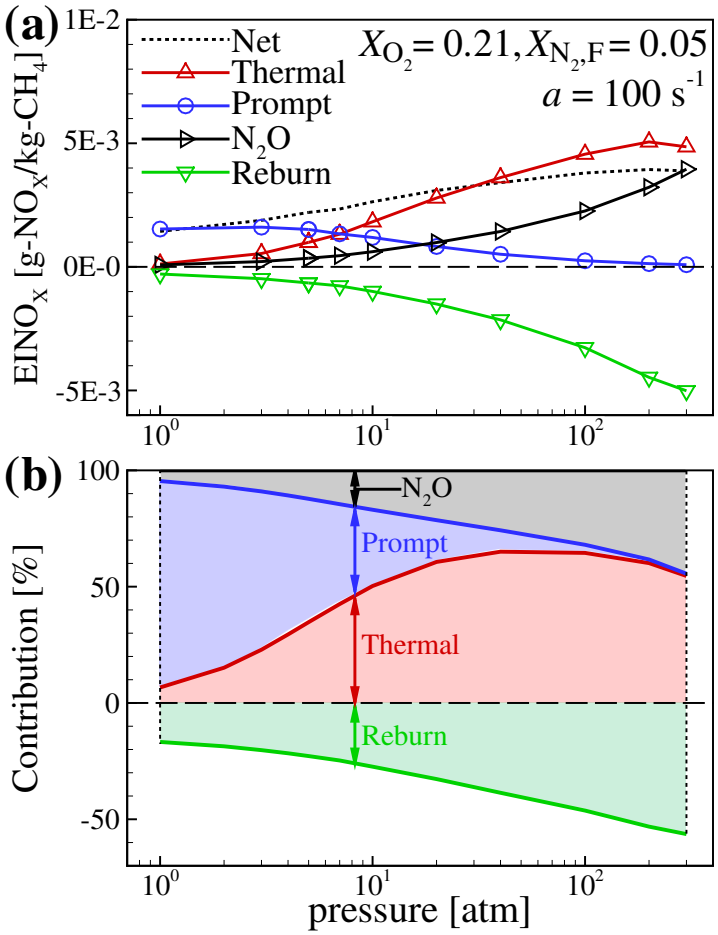

Figure 4.10: Variations of (a) $EINO_X$ and (b) the relative contribution of NO_X formation/reburn pathways as a function of pressure for CH_4 versus O_2/CO_2 counterflow non-premixed flames with $X_{N_2,F} = 0.05$ and $X_{O_2} = 0.21$ at $a = 100\ s^{-1}$.

At relative low-pressure condition (i.e., $p < 5$ atm), the prompt NO_X is the most predominant NO_X generation mechanism while its contribution continuously decreases with increasing pressure. Again, this is mainly because the increase of pressure inhibits the formation of CH and CH_2 radicals, which consequently weakens the prompt NO_X initiation reaction. However, the relative contribution of N_2O pathway increases monotonically with increasing pressure because the initiation of N_2O pathways starts with recombination reactions. Note that $N_2 + O + M \rightarrow N_2O + M$ is found to be a predominant N_2O initiation pathway at relatively-low pressures (i.e., $p < 20$ atm), while $H + O_2 + M \rightarrow HO_2 + M$ and subsequent $N_2 + HO_2 \rightarrow N_2O + OH$ reactions become more important at relatively-high pressure (i.e., $p > 20$ atm). Thermal NO_X is the major NO_X emission source at relatively-high pressure and its relative contribution slightly decreases when $p > 40$ atm due to the marginal increase of T_f (see Fig. 4.4b).

As discussed above, the relative contribution of NO_X reburn pathway increases monotonically with increasing pressure. This trend is observed not only for the oxy-fuel combustion at various X_{O_2} but also for the conventional air-fuel combustion (not shown here), which demonstrates that high pressure plays a critical role in enhancing the NO_X reburn process.

4.3 Conclusions

We elucidated the NO_X emission characteristics of the supercritical CO_2 oxy-fuel combustion by performing one-dimensional numerical simulations of CH_4 versus O_2/CO_2 counterflow non-premixed flames at 300 atm with the OPPDIF code. To take into account the real gas effects in the simulations, a real gas equation of state and general fluid-thermodynamic/transport models are incorporated into the code together with the San Diego mechanism of methane oxidation including NO_X formation. The following results were obtained from the present study.

1. The characteristics of NO_X emission were investigated by measuring $EINO_X$ for various $X_{N_2,F}$ and X_{O_2}. The amount of NO_X emission of the sCO_2 oxy-fuel combustion is significantly reduced compared to that of the conventional air-fuel combustion

even with the maximum allowable N_2 in the fuel stream ($X_{N_2,F} = 0.10$) while they become comparable if T_f of the sCO_2 oxy-fuel combustion is increased to approximately 2700 K by high X_{O_2}.

2. The effect of N_2 ingress on the characteristics of NO_X emission was further elucidated by including N2 in either the fuel or oxidizer stream while keeping their T_f nearly the same. Since the flame zone develops in the oxidizer side, the concentration of N_2 in the flame zone for the case with N2 in the oxidizer stream is much higher than that for the case with N_2 in the fuel stream. As such, the NO_X emission for the case with N_2 in the oxidizer stream is approximately ten times larger than that for the case with N_2 in the fuel stream.

3. The relative contributions of NO_X formation/consumption pathways to the total NO_X emission were estimated by the reaction pathway analysis. The relative contribution of prompt NO_X was found to be negligible for all sCO_2 oxy-fuel combustion cases, which is primarily attributed to the reduction of CH radical pool at high pressures. It was also found that N_2O pathway is predominant at low T_f due to the third-body recombination reactions, and thermal NO_X emission continuously increases with increasing T_f. The relative contribution of NO_X reburn pathway for the sCO_2 oxy-fuel combustion is much larger than that for the air-fuel combustion at 30 atm because both the initiation reactions and efficiency of NO_X reburn pathway are enhanced with increasing pressure.

Chapter V

Estimation of Thermal Radiation Effect on Counterflow Non-premixed Flames under Supercritical Oxy-fuel Combustion Conditions

As mentioned in the introduction, the most numerical simulations under supercritical oxy-fuel combustion conditions have been investigated in the adiabatic condition due to the absence of reliable radiation models. Therefore, the objective of the present study is to estimate the effect of thermal radiation on sCO_2 oxy-fuel combustion. Since there exist no proper radiation models at extremely-high pressure, we first derive two WSGG models by extrapolating the conventional and pressurized WSGG models and then compare their effects by performing one-dimensional simulations of CH_4 versus O_2/CO_2 counterflow non-premixed flames under sCO_2 oxy-fuel combustion conditions.

5.1 Thermal Radiation Models and Numerical Methods

For the conventional WSGG model [114], the emissivity of non-gray gas, ε, is represented by a weighted sum of several gray gas emissivity as follows:

$$\varepsilon = \sum_{i=1}^{n} a_i[1 - \exp(-\kappa_i XPL)], \tag{5.1}$$

where a_i and κ_i are the weighting factor and absorption coefficient of i^{th} gray gas, respectively, X is the sum of H_2O and CO_2 molar fractions, P is the total pressure, and L is the path-length.

For the pressurized WSGG model proposed by Shan et al. [68], the emissivity and weighting factors are expressed as:

$$\varepsilon = \sum_{i=1}^{n} a_i[1 - \exp(-\kappa_{p,i} XL)], \tag{5.2}$$

$$a_i = \sum_{j=0}^{m} c_{i,j} \left(\frac{T}{T_{\text{ref}}}\right)^j, \tag{5.3}$$

where the weighting factors of each gray gas are described by fourth-degree polynomials of temperature. The polynomial coefficients of the weighting factors and absorption coefficients are expressed as a polynomial of total pressure, P:

$$c_{i,j} = C2_{i,j}P^2 + C1_{i,j}P + C0_{i,j}, \tag{5.4}$$

$$\kappa_{p,i} = K2_i P^2 + K1_i P + K0_i, \tag{5.5}$$

where the six coefficients ($C0$, $C1$, $C2$, $K0$, $K1$, and $K2$) of i^{th} gray gas are tabulated as functions of pressure and the molar ratio of H_2O to CO_2, MR ($= X_{H_2O}/X_{CO_2}$) [68]. For the pressurized WSGG model, four gray gases are selected to guarantee a reasonable accuracy. For details of the pressurized WSGG model, readers are referred to [68]. For simplicity, henceforth, WSGG-Shan denotes the pressurized WSGG model proposed by Shan et al. [68].

To calculate the thermal radiation source term at high pressure, the absorption coefficients and weighting factors of gray gases of a pressurized WSGG model should be

specified as explained above. Since there are no WSGG models at extremely high pressure, we estimate the absorption coefficients and emissivity at 300 bar using the data of WSGG-Shan within 1 – 30 bar, from which the weighting factors are obtained. To be more specific, the absorption coefficients of four gray gases are first estimated by extrapolating the data using a logarithmic function for all MR. In the same way, the emissivity at 300 bar is then predicted by another logarithm function. Henceforth, WSGG-Log denotes a pressurized WSGG model that estimates the emissivity and absorption coefficients using the logarithmic extrapolation.

Figure 5.1a shows the estimated absorption coefficients of four different gray gases as a function of pressure for the WSGG-Log and WSGG-Linear models. Here, WSGG-Linear denotes a pressurized WSGG model that estimates the absorption coefficients of i-th gray gas at P by multiplying those of the WSGG-Shan model at 1 bar with P, or $\kappa_{p,i} = \kappa_i P$ and the weighting factors at 1 bar. An error bar in the figure represents the range of an absorption coefficient for different MR. It is readily observed from the figure that the WSGG-Linear model overestimates the absorption coefficients approximately by two orders of magnitude as compared to the data from Shan et al. [68] and those estimated by the WSGG-Log model. As such, the absorption coefficients of four gray gases for the WSGG-Linear model becomes approximately two orders of magnitude larger than those of other models regardless of pressure (see Fig. 5.1b).

Figure 5.2 shows the emissivity estimated by the WSGG-Log and WSGG-Linear models at 300 bar as a function of path-length for various temperatures and MR. It is readily seen from the figure that for both models, the emissivity increases with decreasing temperature and increasing MR for a given path-length while it increases with the path-length for given temperature and MR, similar to those at relatively-low pressures [68, 114]. In addition, the emissivity of the WSGG-Linear model becomes greater than that of the WSGG-Log model for relatively-small path-length while it becomes smaller for relatively-large path-length. This is because for the WSGG-Linear model, the emissivity is estimated using the absorption coefficients and weighting factors at 1 bar, while for the WSGG-Log model it is obtained from the logarithmic extrapolation as explained above.

In this chapter, to estimate the thermal radiation effect on CH_4 versus O_2/CO_2 coun-

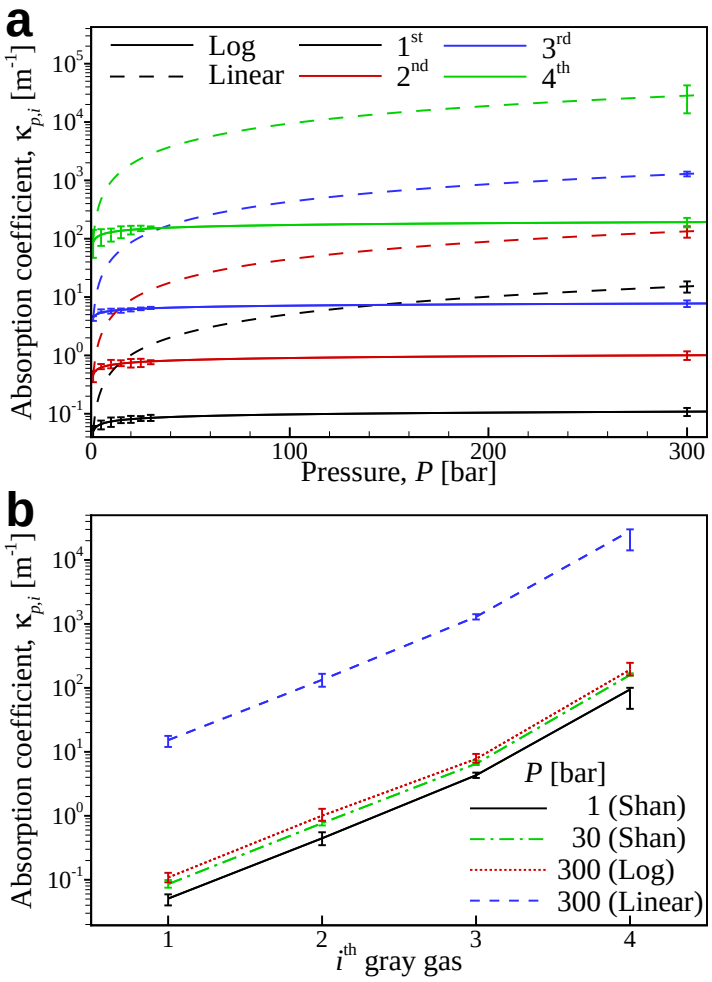

Figure 5.1: Estimated absorption coefficients, $\kappa_{p,i}$, (a) as a function of pressure for the WSGG-Log and WSGG-Linear models, and (b) for different models. An error bar represents the range of an estimated absorption coefficients for different MR.

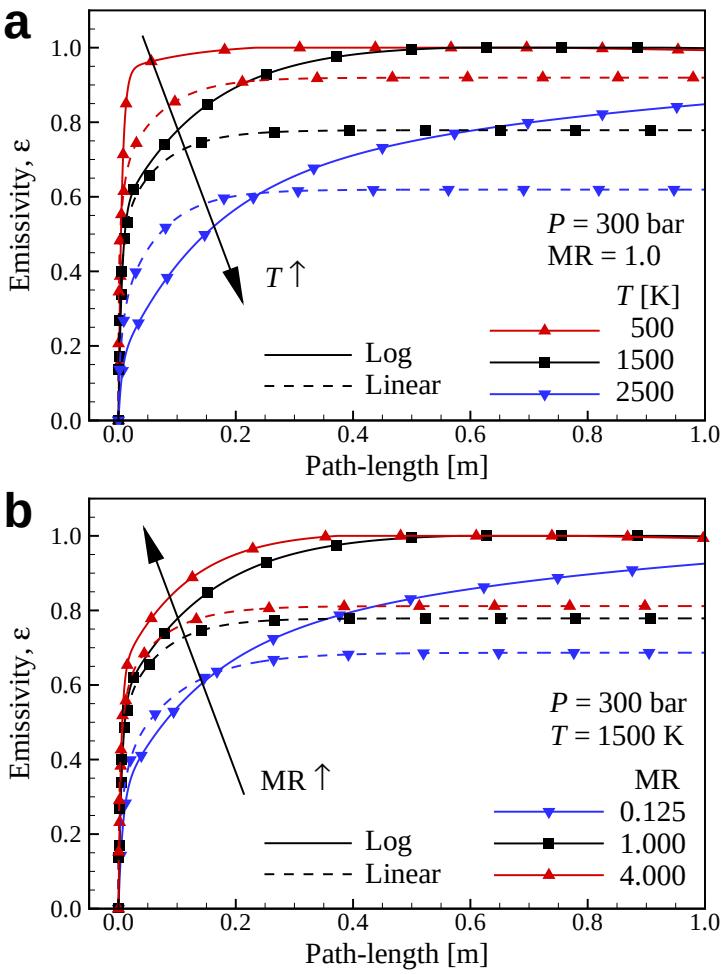

Figure 5.2: Estimated emissivity, ε, for the WSGG-Log model at 300 bar as a function of path-length for (a) various temperature with MR = 1 and (b) various MR with 1500 K.

terflow non-premixed flames under sCO_2 oxy-fuel combustion conditions, one-dimensional numerical simulations are performed using a modified OPPDIF code [62]. To take real gas effects into account, we incorporate a modified Soave-Redlich-Kwong equation of state [104, 105], real thermodynamic properties [106] based on CHEMKIN library [82], Chung's model [107] for real transport properties, and Takahashi's model [108] for binary mass diffusion coefficients at high pressure into the code [115]. Since we are interested in the radiation effect on flames such as reduction of flame temperature by radiative heat loss, the GRI-Mech 3.0 [116] is adopted for methane oxidation even though it is not validated for extremely-high pressures.

Using the modified OPPDIF code with various thermal radiation models, the flame characteristics are investigated by varying global strain rate, a, which is defined as $a = 2(|U_F| + |U_O|)/H$, where U is the axial velocity and H of 5 cm is the distance between two inlets. The subscripts F and O represent the fuel and oxidizer inlet, respectively. At each pressure, the strain rate varies from 10 s^{-1} till the flame is extinguished. The fuel is methane while the oxidizer is O_2 diluted by CO_2 (21% O_2 + 79% CO_2 by volume). The inlet temperatures of the fuel and oxidizer streams are 300 and 1000 K, respectively, which are similar to those of the non-premixed combustor of a direct fired sCO_2 gas turbine [54]. The radiative transfer equation (RTE) is solved using the discrete ordinate method (DOM) with S4 quadrature [66, 114, 117].

5.2 Results and Discussions

The thermal radiation effect on CH_4 versus O_2/CO_2 counterflow non-premixed flames under sCO_2 oxy-fuel combustion conditions are investigated in a wide range of strain rate and pressure. Figure 5.3 shows the maximum flame temperature, T_f, and temperature difference, ΔT_f, between the adiabatic and WSGG models as a function of strain rate for different pressures of 1, 30, and 300 bar. Here, the adiabatic model without radiative heat loss is denoted by ADI. Several points are noted from the figure.

First, T_f of the WSGG models becomes the largest approximately at $a = 100$ s^{-1} for all pressures. This is because T_f is reduced by radiative heat loss at relatively-low a (<

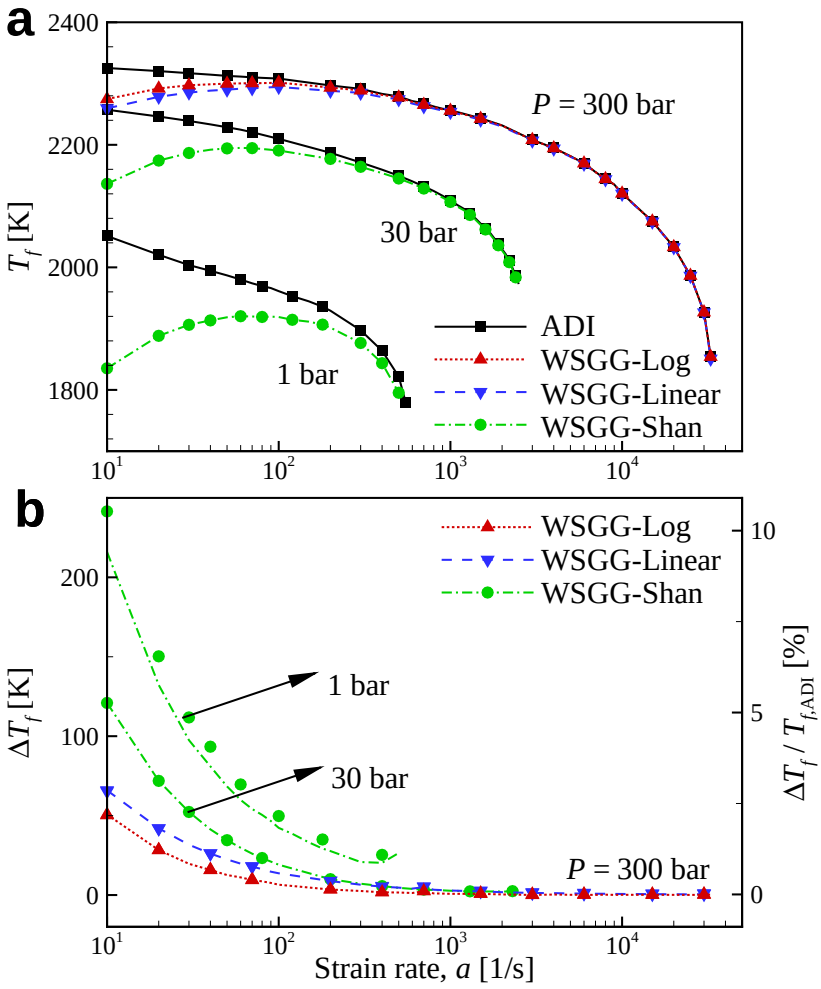

Figure 5.3: (a) Maximum flame temperature and (b) temperature difference (line) and the ratio (symbol) between adiabatic and various thermal radiation model cases as functions of strain rates at 1, 30, and 300 bar.

100 s^{-1}), and by reactant leakage and subsequent incomplete reaction at relatively-large a (> 100 s^{-1}) [5,49,118]. On the contrary, T_f of the ADI model keeps decreasing with a till flame extinction occurs by high a. As shown in Fig. 5.3b, therefore, ΔT_f between the ADI and WSGG models increases with decreasing a where radiative heat loss evaluated by the WSGG models becomes large.

Second, it is readily observed from Fig. 5.3b that ΔT_f between the ADI and WSGG models decreases with increasing pressure for a given strain rate. As a result, ΔT_f for the WSGG-Shan model are approximately 10.5% of $T_{f,\mathrm{ADI}}$ at 1 bar and 5.4% at 30 bar, respectively. Meanwhile, ΔT_f for the WSGG-Log and WSGG-Linear models are approximately 2.2 and 2.8% of $T_{f,\mathrm{ADI}}$, respectively, even at $a = 10^{-1}$ and 300 bar. As such, ΔT_f between the ADI and WSGG models at 300 bar is less than 1% of $T_{f,\mathrm{ADI}}$ in most range of strain rate.

It is worth mentioning that in this chapter, we adopted two WSGG models to describe the radiation effect at 300 bar: one is the WSGG-Log model that estimates the absorption coefficients and emissivity by reasonably extrapolating the data within 1 – 30 bar and the other is the WSGG-Linear model that estimates $\kappa_{p,i}$ as $\kappa_i P$ such that its absorption coefficients are usually overestimated by two orders magnitude as compared to those of the WSGG-Shan and WSGG-Log models; however, ΔT_f between the ADI and WSGG models at 300 bar are marginal even for relatively-low strain rates. This result implies that under sCO_2 oxy-fuel combustion conditions, the radiative heat loss effect on flame temperature drop is negligible, and hence, it would be reasonable to ignore the thermal radiation effect in numerical simulations of sCO_2 combustion, which, however, needs to be further verified in the future.

To identify the reason why ΔT_f between the ADI and WSGG models are so small at 300 bar, the profiles of flame temperature, T, reaction heat release rate, $\dot{Q}$, and radiative heat loss, $\dot{Q}_L$, at three different a of 10, 100, and 30000 s^{-1} for three different radiation models are shown in Fig. 5.4.

It is found that the maximum $\dot{Q}$, $\dot{Q}_{\max}$, is significantly decreased by three orders magnitude (i.e. $23.8 \rightarrow 0.42 \rightarrow 0.06$ kW/mm^3) regardless of the radiation models as a decreases from 30000 to 10 s^{-1}. However, $\dot{Q}_{L,\max}$ for the WSGG-Log changes from

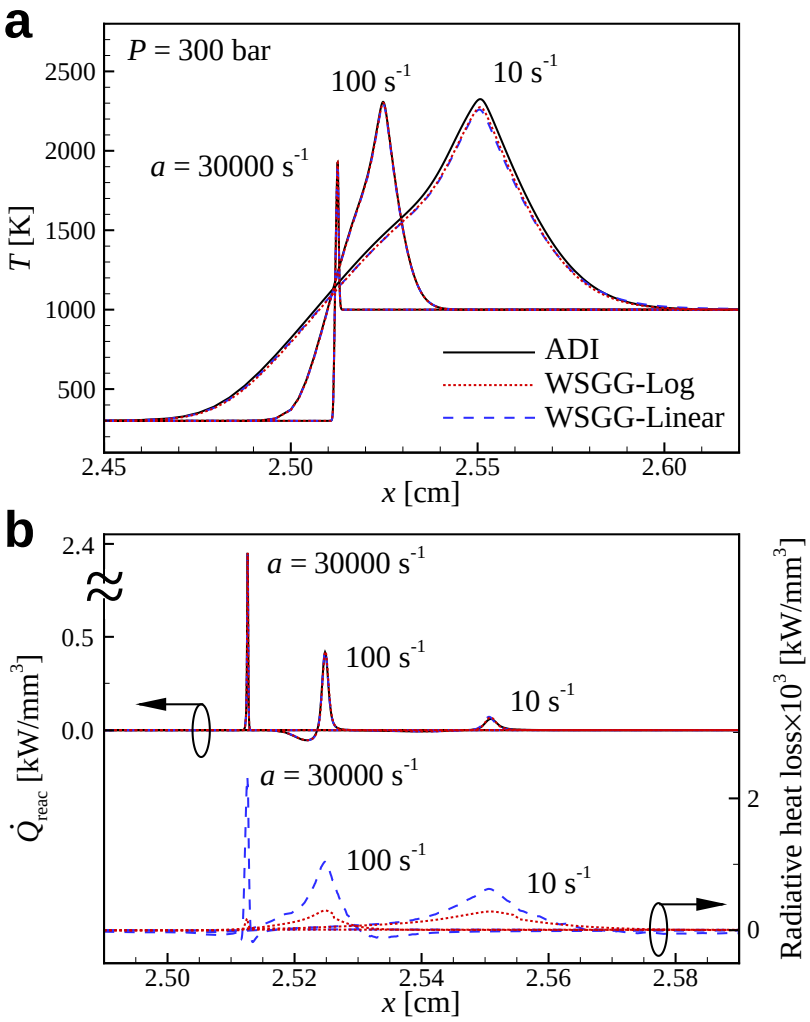

Figure 5.4: Profiles of (a) temperature and (b) reaction heat release, $\dot{Q}$, and radiative heat loss, $\dot{Q}_L$, at a = 10, 100, and 30000 s^{-1} and 300 bar for three different radiation models.

0.18 $\times 10^{-3}$ to 0.30 $\times 10^{-3}$ to 0.28 $\times 10^{-3}$ kW/mm^3 while for the WSGG-Linear model, it varies from 2.32 $\times 10^{-3}$ to 1.04 $\times 10^{-3}$ to 0.63 $\times 10^{-3}$ kW/mm^3. Therefore, $\dot{Q}_{L,\max}$ of both WSGG models at $a = 10$ s^{-1} become two orders magnitude smaller than $\dot{Q}_{\max}$, which quantitatively explains that ΔT_f between the ADI and WSGG models become approximately 2 – 3% of $T_{f,\mathrm{ADI}}$. At $a = 30000$ s^{-1}, however, $\dot{Q}_{L,\max}$ of the WSGG models become approximately four to five orders of magnitude smaller than $\dot{Q}_{\max}$, and hence, T_f of the WSGG models are nearly the same. It is of interest to note that for the WSGG-Linear model, $\dot{Q}_L$ is more estimated than that for the WSGG-Log model in the whole range of strain rate due to its significantly large absorption coefficients compared to those of the WSGG-Log model.

5.3 Conclusions

In this chapter, one-dimensional numerical simulations of CH_4 versus O_2/CO_2 counter-flow non-premixed flames under sCO_2 oxy-fuel combustion conditions were conducted with various radiation models such as the adiabatic (ADI) model and two pressurized WSGG model: one is the WSGG-Log model that estimates the absorption coefficients and emissivity by reasonably extrapolating the data within 1 – 30 bar of Shan et al. [68] and the other is the WSGG-Linear model that estimates $\kappa_{p,i}$ as $\kappa_i P$. The response of flame temperature to strain rates was investigated at 300 bar for the WSGG models by comparing with the ADI model. Under sCO_2 oxy-fuel combustion conditions, ΔT_f between the ADI and WSGG models are negligible in most range of strain rate because the reaction heat release is significantly larger than the radiative heat loss estimated by the WSGG models, which suggests that it may be reasonable to ignore the radiative heat loss from flames under sCO_2 oxy-fuel combustion conditions.

Chapter VI

Numerical Analysis for Performance Test of a Lean Premixed Model Gas Turbine Combustor

In Chapter II and III, flame instabilities of opposed non-premixed tubular flames are investigated by using 1-D/2-D numerical simulations under adiabatic and non-adiabatic conditions. In Chapter IV, one-dimensional numerical simulations of counterflow non-premixed flames are under supercritical oxy-fuel combustion conditions conducted to understand the fundamental characteristics and NO_X emission as different N_2 ingress situations. The thermal radiation effects on the flames are estimated in Chapter V. Although we have studied on the fundamental characteristics of strained non-premixed flames under various conditions, the ultimate objective of numerical simulations is to solve the real-scale problem.

In this chapter, therefore, the characteristics of swirled-stabilized turbulent lean-premixed CH_4/air flames under various conditions are investigated by performing 3-D RANS simulations. Based on the results of CFD simulations, the NO_X emission prediction is conducted by CRN models, and then the cycles to failure at the vulnerable regions in a single nozzle model combustor are also estimated by the thermal fatigue analysis. First, to validate numerical models and computational mesh of fluid fields, the results of numerical simulations are compared with the measurement of experiments. Two different

axial swirler nozzle models, high/low swirler nozzle (HSN/LSN), are used to investigate the fundamental characteristics of swirl-stabilize flames in a model combustor. The finite elements analysis (FEA) mapping CFD analysis results identifies areas vulnerable to the thermal strain. Finally, at damaged regions, the dynamic response analysis of the strain is compared to the ε-N curve to predict the thermal fatigue life of high temperature components. This process will proceed with the concept of finding the appropriate a nozzle type and operating condition like the design stage.

6.1 Experimental and Numerical Setup

6.1.1 Model Combustor

Figure 6.1 shows a schematic of the experimental setup of a gas turbine model combustor. This facility consists of a control part, measurement sensors, an axial swirler nozzle, a combustor, a cooling system, and an exhaust pipe. The sensors can measure a central velocity, temperatures at 9 points, and dynamic pressure. Turbulent lean-premixed CH_4/air flames can be measured through the quartz liner, around 300 mm length.

As mentioned above, the effects of swirler nozzles on combustion characteristics are

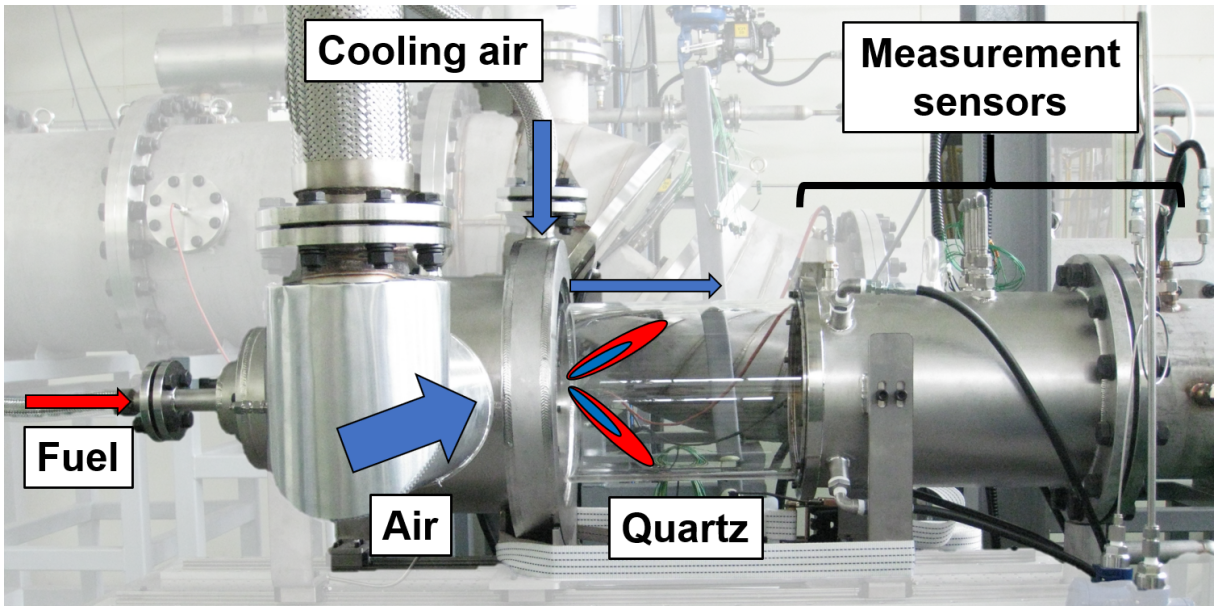

Figure 6.1: Experimental setup of a lean premixed model gas turbine combustor.

investigated in this chapter: a high swirler nozzle and a low swirler nozzle. The difference between two nozzles comes from the swirl vane angle and inner/outer diameter. In this context, swirl number, S, can be defined by [119]:

$$S = \frac{2}{3}\left[\frac{1-(r_i/r_o)^3}{1-(r_i/r_o)^2}\right]\tan\theta \tag{6.1}$$

where r_i and r_o are inner and outer diameter of a nozzle, and θ is swirl vane angle. In the present, corresponding swirler numbers of high and low swirler nozzle are 0.90 and 0.47, respectively. This difference is enough to expect the effect of swirl number. Considering only effects of different swirler types, the nozzle exit velocities for cases with the same equivalence ratio are matched regardless of different swirler geometry.

The flow field of a model combustor and computational mesh of the front mixing part and rear combustor part are shown in Fig. 6.2. The length and height of front mixing part as shown in Fig. 2b are 405 mm and 400 mm, respectively. The outer nozzle diameter of the high and low swirler nozzle are 105 mm and 135 mm, respectively. The distance from nozzle exit to outlet is approximately 1500 mm and the diameter is 250 mm. The structured hexahedral mesh is generated in most flow fields except the inlet parts which have relatively complex flow passages such as fuel ways, oxidizer ways, and a single nozzle. To precisely capture swirl-stabilized flames, the finer mesh is adopted at the combustor behind a single nozzle. For the high swirler nozzle case, the elements are 10.4 million while for the low swirler nozzle case, the elements of 7.3 million are used.

6.1.2 Numerical Methods

In this chapter, numerical simulations are divided into three parts: 3-D turbulent reacting flow simulation, prediction of NO_X emission and thermal fatigue analysis. First, CFD simulations are carried out using a commercial software, Fluent 2019 R2 [120]. Semi implicit method for pressure-linked equations (SIMPLE) algorithm, one of pressure based segregated algorithms, is used to obtain the pressure field, which is suitable for steady-state flows [78]. The realizable k-ε turbulence model with standard wall functions is adopted because it shows better performance than traditional k-ε turbulence model for various flows including rotation, boundary layers, separation, and recirculation [120].

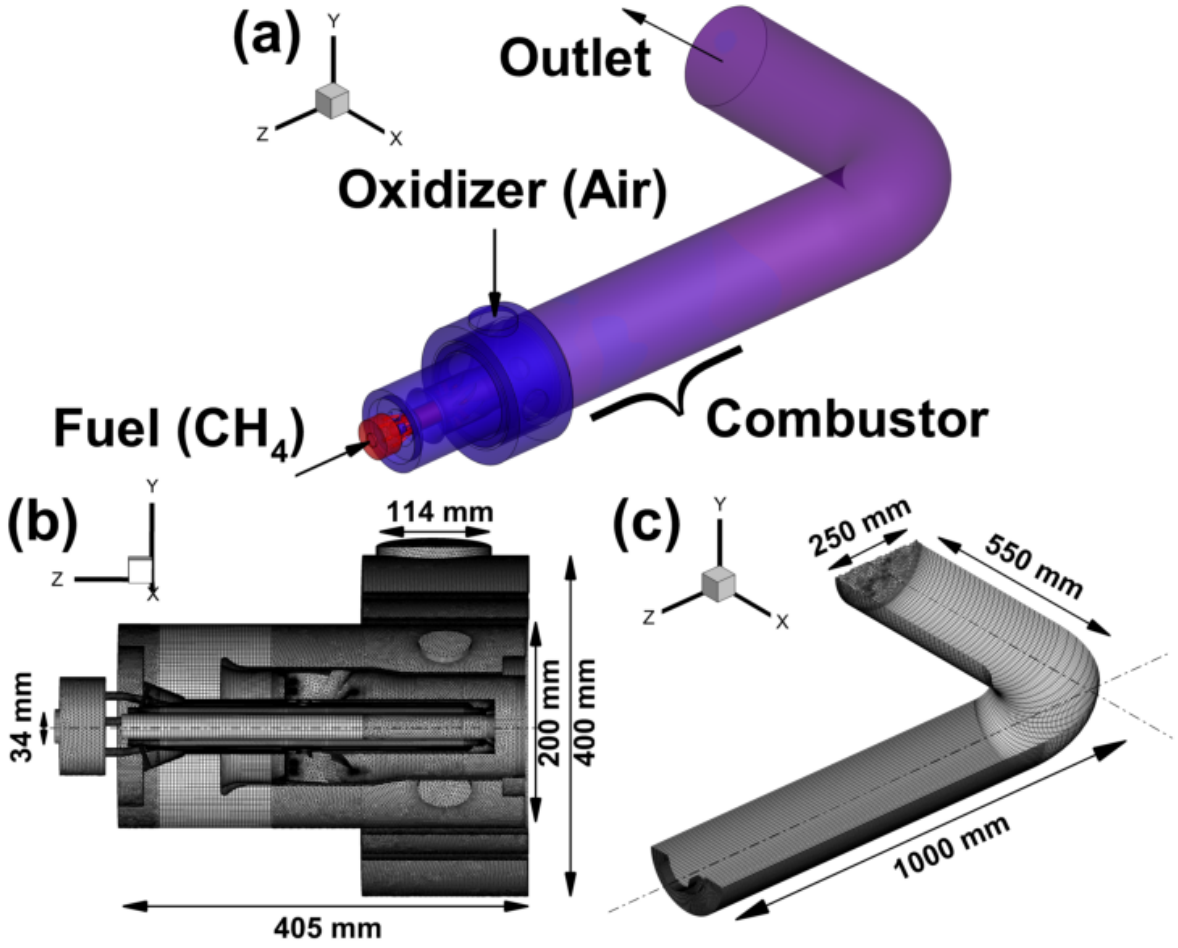

Figure 6.2: (a) Flow field of a model combustor and computational mesh of (b) front mixing part, (c) rear combustor and exhaust pipe part.

The turbulent Schmidt number, Sc_t, is set to 0.7. The eddy-dissipation model is used to solve the turbulence-chemistry interaction. To simulate methane/air flames, two-step methane/air global reaction mechanism by Westbrook and Dryer is adopted [121].

The nonreacting mixing problems are solved to attain good initial conditions for turbulent combustion simulations, and then high temperature field for ignition is patched at the combustor to initiate reaction. In the nonreacting mixing problems, default under-relaxation factors for all variables are applied. On the other hands, in the combustion simulations, the parameters are properly reduced to avoid the divergence.

For predicting NO_X emission based on CFD results, CRN analysis is conducted by using CHEMKIN-PRO 2019 R2 [82]. Although methane/air global reaction mechanism is adopted to reduce computational cost in 3-D turbulent reacting flow simulations, it is possible to use a detailed chemical mechanism without wasting computational times. In the present, therefore, GRI-3.0 mechanism for precise estimation of NO_X emission is employed [116].

The finite element analysis for the thermal fatigue analysis based on ε-N curve is carried out using Abaqus 2019 [83]. AISI type 304 stainless steel is chosen, and its major material properties are summarized as follows: the density, ρ, is 8 g/mm^3, the Young's modulus, E, is 200 GPa, the Poisson ratio, ν, is 0.29, the yield stress, ρ_y, is 215 MPa, the thermal conductivity, k, is 16.2 W/m-K, the coefficient of thermal expansion, α, is 18.7 μm/m-K [122–125]. In this chapter, the temperature and pressure field obtained from 3-D RANS simulations of turbulent combustion are mapped to inner boundary field of a model combustor. To solve a problem due to the mismatch between the grids of fluid and solid fields, the linear interpolation is employed. Initial fields of temperature and pressure are generated through heat transfer analysis with the material thickness of 8 mm, and then FEA is conducted.

6.1.3 Comparison of Experimental and Numerical Results

To validate the accuracy of RANS simulations, 3-D RANS combustion simulations are conducted and the results are compared to those of experiments. The experimental and numerical simulation conditions are listed in Table VI.1. These conditions are chosen to verify that the system is stable at around 40 % load condition before testing the full load. The mass flow rate and temperature of the fuel, pure methane, are 0.001891 kg/s and 454 K, and those of the air are 0.1256 kg/s and 635 K, respectively. The equivalence ratio is corresponding to 0.258. The experiments and numerical simulations are conducted at atmospheric pressure. In the process, the high swirler nozzle is used for validation.

Figure 6.3 shows some major variables of (a) a cold flow test and (b) a combustion test at specific planes. The velocity magnitude field on a x-z plane are plotted in the left column. The axial velocity for the cold flow test and the temperature distribution for the combustion test are measured at 500 mm and 700 mm downstream of the single nozzle exit, respectively. In the right column of Fig. 6.3, measure points are marked as black dots. A speed sensor is centrally located as shown in Fig. 6.3a. A total of nine

Cold flow test		
Mass flow rate (kg/s)	Air	0.0599
Temperature (K)		673
Combustion test		
Mass flow rate (kg/s)	Fuel	0.001891
	Air	0.1256
Temperature (K)	Fuel	454
	Air	635
Equivalence ratio		0.258
Operating pressure (atm)		1

Table VI.1: Experimental and numerical simulation condition: a cold flow test and combustion test

Cold flow test			
Position	$V_{Z,\text{Exp.}}$ (m/s)	$V_{Z,\text{Num.}}$ (m/s)	Error (%)
-	6.10	6.19	1.48
Combustion test			
Position	$T_{\text{Exp.}}$ (K)	$T_{\text{Num.}}$ (K)	Error (%)
1	1314.6	1273.7	3.92
2	1277.2	1291.2	1.39
3	1246.9	1271.3	2.51
4	1279.2	1285.4	0.62
5	1246.8	1302.5	5.72
6	1293.3	1287.5	0.56
7	1243.2	1271.1	2.88
8	1256.6	1292.0	3.61
9	1166.9	1276.9	12.3

Table VI.2: Temperature information at measured points in experimental and numerical results.

temperature sensors are separated by ± 50 mm in the x-direction and ± 62.8 mm in the y-direction from the origin as shown in Fig. 6.3b. The measured and numerical data are compared in Table VI.2. The average errors of a cold flow test and a combustion test are 1.48 % and 3.72 %, respectively. Therefore, it means that the numerical mesh and models are reasonable in this chapter. In addition, it is found that the flow field is arranged and stabilized by the flame. The detail in the characteristics of the swirl-stabilized flames will be discussed in the next section.

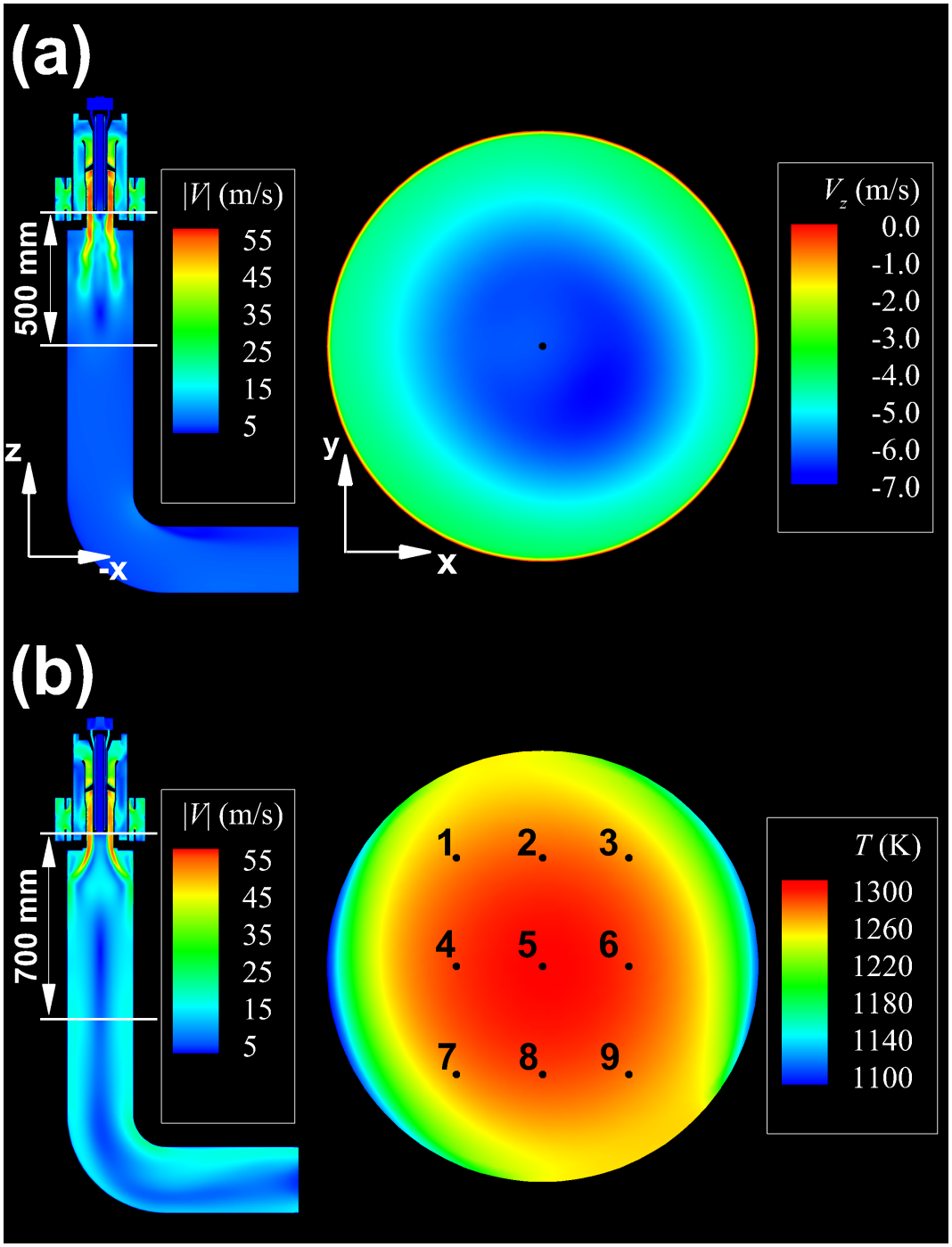

Figure 6.3: Velocity fields and temperature field of (a) a cold flow test and (b) a combustion test.

6.2 Results and Discussions

6.2.1 Computational Fluid Dynamics Analysis of 3-D Turbulent Reacting Flows

To elucidate the effects of different equivalence ratios and swirler numbers, 3-D RANS simulations of turbulent premixed flames are conducted. The equivalence ratios of 0.5, 0.6, and 0.7 are adopted for both high and low swirler nozzle cases. The inlet temperatures of the fuel and oxidant are 300 K and 700 K, respectively. The mass flow rate of the fuel is set to 0.004559 kg/s for the high swirler nozzle cases, and that of air is varied with the equivalence ratio. Similarly, for the low swirler nozzle cases, the temperatures of two inlets are identical to that of high swirler nozzle cases. However, the mass flow rate of the fuel is set to 0.00849 kg/s, which is approximately two times larger than that for the high nozzle cases to compensate for the difference between nozzle diameters. Reynolds number of each case is varied from 1.20×10^5 to 1.74×10^5, and this value is large enough to generate turbulent flow.

Figure 6.4 shows isocontours of the temperature and reaction rate of Reaction 1 (CH_4+$1.5O_2 \rightarrow CO + 2H_2O$) at a x-z plane of the high swirler nozzle combustor and the low swirler nozzle combustor for different equivalence ratios. Several points are noted from the figure. First, V-shaped flames are readily observed for all cases. If the momentum of pre-mixture at the nozzle exit is not large enough to generate inner recirculation zone, the flames is closed and does not exhibit a V-shaped flame. The swirl-stabilized flames for high swirler cases have higher flame angle and shorter flame length than those for low swirler cases. The angles of the high and low swirler nozzle flames at $\phi = 0.5$ are approximately 24.2deg and 11.8deg, respectively. The flame lengths of the high and low swirler nozzle cases are approximately 15 and 30 cm, respectively, which implies that a relatively strong outer recirculation zone is developed with increasing the swirl number from 0.47 to 0.90.

Second, the maximum temperature of high (low) swirler nozzle cases increases from 1836.0 K (1981.0 K) to 2224.0 K (2290.2 K) with increasing ϕ. For the whole cases, the

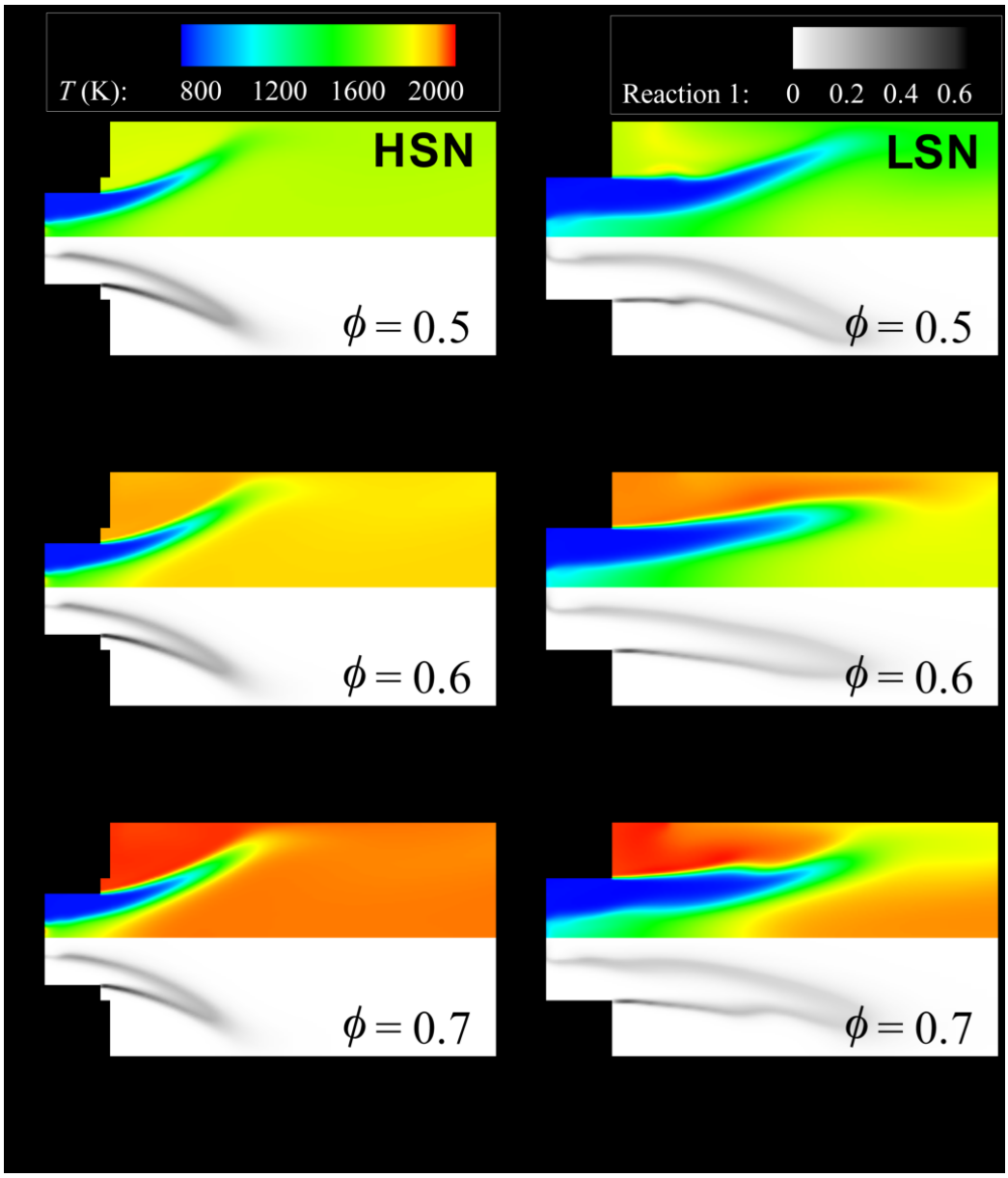

Figure 6.4: Temperature isocontours and reaction rate of Reaction 1 of high swirler nozzle (left) and low swirler nozzle (right) with $\phi = 0.5$, 0.6, and 0.7.

maximum temperature occurs at the outer recirculation zone. This is because the flow in the outer recirculation zone is confined by the wall and flame and keeps being heated by the flame. The reaction rates in high swirler nozzle cases are also relatively higher than those in low swirler nozzle cases, which implies that the high swirler nozzle makes the flames more stable and stronger with less amount of fuel and air than that the low swirler nozzle.

To figure out the characteristics of flow fields with different swirler types, the axial velocity and its magnitude with streamlines are shown in Fig. 6.5. It is easily observed that recirculation zones are developed for both cases. Depending on the location of the recirculation zones, they can be divided into two parts: 1) inner recirculation zone and 2) outer recirculation zone. It has been found that a strong flow swirl can stabilize flames by increasing flame speed with higher turbulence intensity and by improving mixing, featuring shorter flames and reduced NO. In addition, one of the major roles of the swirl is to develop recirculation zones that generate low velocity regions to anchor the flame [126]. For the high swirler nozzle case, the swirl develops stronger at the inner recirculation zone than that at the outer recirculation zone. However, for the low swirler nozzle case, the inner recirculation zone considerably diminishes because the swirl effect of the low swirler nozzle is much less significant than that of the high swirler nozzle. In summary, better flame characteristics are obtained for the high swirler nozzle cases because of the effects of stronger recirculation zones.

6.2.2 Prediction of NO_X Emission by Chemical Reactor Networks

To elucidate the NO_X emission characteristics for cases with different nozzles and operating conditions, the chemical reactor network (CRN) method is applied to 3-D RANS simulation results. Figure 6.6 shows examples of divided reactor zones of high (upper) and low (bottom) swirler nozzle cases at $\phi = 0.5$ for the CRN method. A schematic of a CRN model for a high swirler nozzle case is also shown in the figure, of which numerical domain is divided into 6 different reactors including 5 perfectly stirred reactors (PSRs)

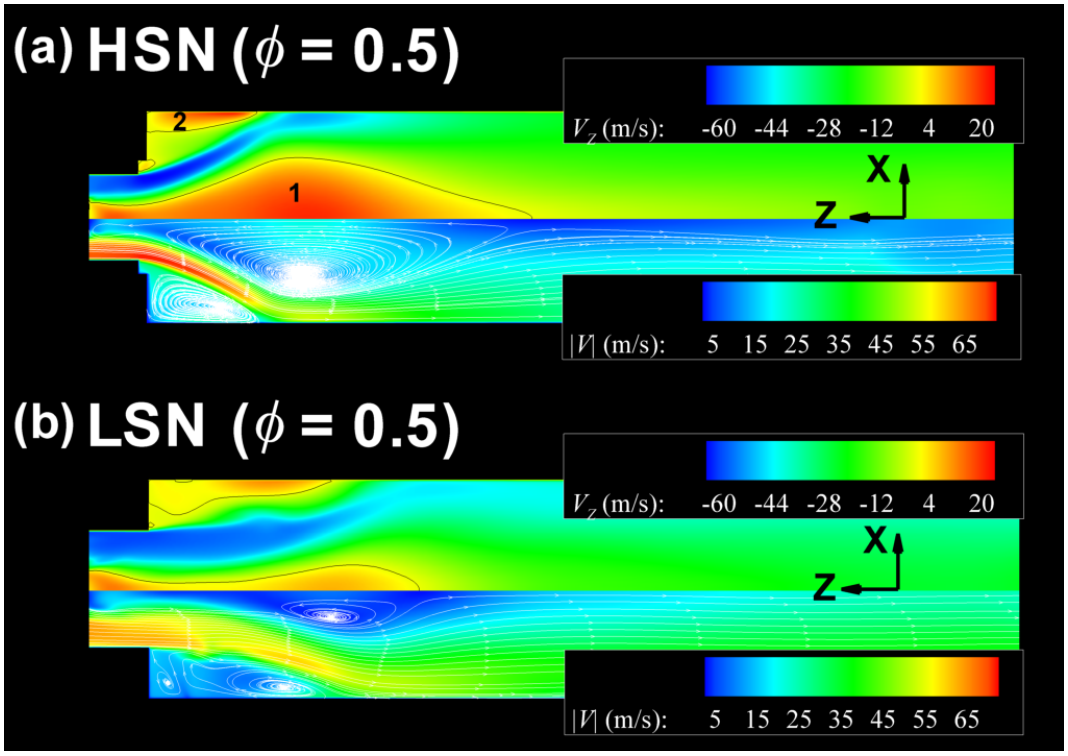

Figure 6.5: Z-velocity, V_z, and velocity magnitude, $|V|$, with streamlines of (a) a high swirler nozzle case and (b) a low swirler nozzle case with $phi = 0.5$. Black lines of upper parts represent $V_z = 0$.

and 1 plug flow reactor (PFR): I. Mixing zone, II. Flame zone, III. Outer recirculation zone, IV. Inner recirculation zone, V. Intermediate flame zone, and VI. Post flame zone. Although it was found that a detailed CRN model shows better accuracy close to the experimental data [80], in this chapter, a simple CRN model with only 6 elements is chosen to make the problem simple because there exists no big difference for the purpose of qualitative comparison.

It is readily observed from Fig. 6.6b that for the high swirler case with $\phi = 0.5$, 92 % flow comes into an intermediate flame zone through a flame zone and only 8 % products are leaked into the outer recirculation zone. Also, 90 % mass flow from an intermediate flame zone enters the post flame zone, and the rest 10 % flow remains in an inner recirculation zone. In the same way, each reactor condition at different cases is decided by considering mass flow rates between adjacent zones. To quantitatively measure NO_X emission from the model combustor, the emission index of NO_X, $EINO_X$, at each reactor is adopted, which is defined by:

$$\mathrm{EINO_X}(j) = \frac{(\dot{m}_{\mathrm{NO}} - \sum \dot{m}^*_{\mathrm{NO}}) + (\dot{m}_{\mathrm{NO_2}} - \sum \dot{m}^*_{\mathrm{NO_2}})}{-(\dot{m}_{\mathrm{CH_4}} - \sum \dot{m}^*_{\mathrm{CH_4}})} \tag{6.2}$$

where j is the reactor number, $\dot{m}^*_k$ is the inlet mass flow rate of species k, and $\dot{m}_k$ is the outlet mass flow rate of species k, respectively. The Eq. (2) means the ratio of generated mass flow rate of NO_X to consumed mass flow of fuel at a reactor of j.

Figure 6.7 shows temperature and $EINO_X$ at each PSR in high and low swirler nozzle cases with different equivalence ratios. Several points are noted. First, for all cases temperature increases significantly right after the mixing zone (I) due to the reaction, and hence, most NO_X is generated at the flame zone (II), the intermediate flame zone (V), and the post flame zone (VI). However, the NO_X generation at the inner and outer recirculation zones (III and IV) is relatively negligible NO_X although temperature at the recirculation zones is high. These results are primarily attributed to that the main flow passes through PSR I, II, V, and VI. Second, $EINO_X$ is increased with increasing ϕ because the flame temperature increases with ϕ as expected, which implies that the thermal NO_X reaction pathway plays a critical role in NO_X emissions. Third, it is readily observed that the amount NO_X generation for the high swirler cases is less than that of

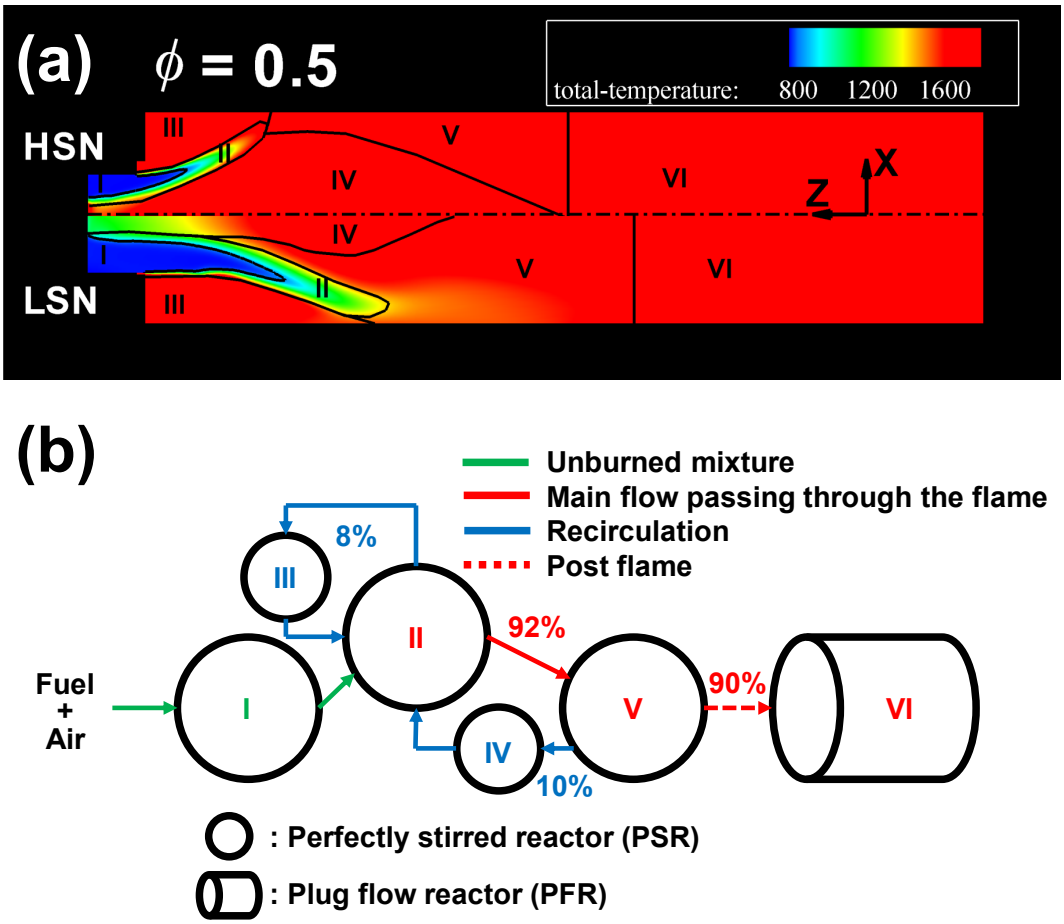

Figure 6.6: (a) Reactor zones of high (upper) and low (bottom) swirler nozzles at $\phi = 0.5$ and (b) a schematic of chemical reactor network composed of 5 perfectly stirred reactors (PSRs) and 1 plug flow reactor (PFR): I – Mixing zone, II – Flame zone, III – Outer recirculation zone, IV – Inner recirculation zone, V – Intermediate flame zone, and VI – Post flame zone.

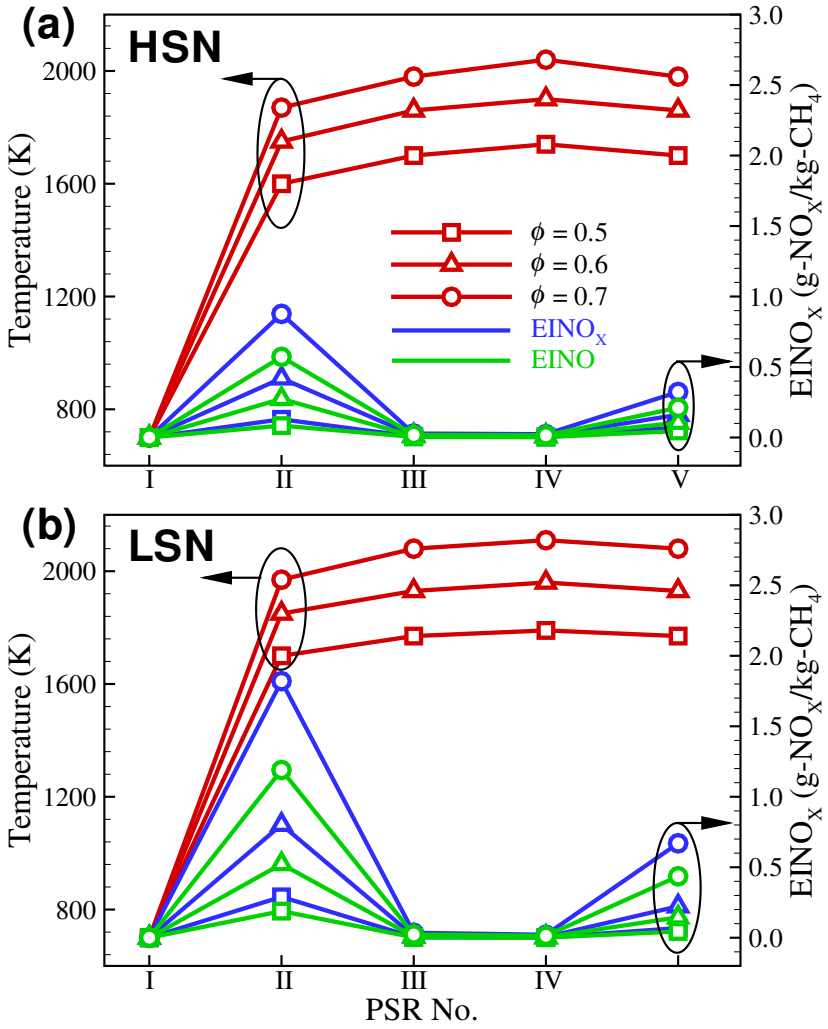

Figure 6.7: Temperature and EINO$_X$ at each perfectly stirred reactor (PSR) in (a) high and (b) low swirler nozzle cases with different equivalence ratios.

the low swirler cases at the same ϕ. This is because the temperatures of the high swirler cases are relatively low compared to those of the low swirler cases even if the equivalence ratio is identical.

To figure out the effect of the post flame zone length on the NO$_X$ emission, the temperature and amount of NO$_X$ emission along the axial direction in the PFR are shown in Fig. 6.8 for both high and low swirler nozzle cases with different equivalence ratios. The length of PFR is set to 140 cm, identical to that of the model combustor. The residence time is defined by the distance of PFR divided by average velocity in the post flame zone. It is readily observed from the figure that at the very forepart

of PSR, temperature first increases slightly and then levels off right downstream. The maximum temperature for the high swirler nozzle cases increases from 1805 to 2134 K with increasing ϕ. However, the maximum temperatures along the axial direction are nearly the same for both high and low swirler cases with the same ϕ except for the forepart because the equivalence ratios at the mixture nozzle exit are identical to each other. For the high (low) swirler cases, the amount of NO_X emission at the exit increases from 5.75 (5.87) to 276.2 (161.2) ppmvd with increasing ϕ. This is primarily because the residence time in the post flame region for the high swirler case are almost twice larger than those for the low swirler case at the same ϕ. Therefore, even though the starting NO_X amounts at the post flame zone for the low swirler cases are relatively large compared to those for the high swirler cases, NO_X is more generated for the high swirler cases due to their longer cooking time for NO_X generation. This result implies that to reduce NO_X emission from a gas turbine combustor, not only the operating temperature should be decreased under lean premixed combustion, but the residence time reduction of combustion products within the combustor is also required, which can be achieved by increasing velocity and/or decreasing the system size through the optimization of flow passage.

6.2.3 Thermal Fatigue Analysis

To predict damaged areas and number of cycles to failure, thermal fatigue analysis was carried out using finite element analysis (FEA). The 3-D RANS simulation of reacting flow for a high swirler nozzle case with $\phi = 0.5$ is chosen for FEA. We map the inner boundary fields of the 3-D RANS simulation to those of FEA. In addition, we assume the initial condition for internal temperature as a thermal conduction model for the stainless steel with 8 mm thickness. To considering the material deformation in the combustion system, we tested various situations such as temperature variation of the working fluid, the pressure difference, and external forces. In this chapter, the structural deformation by the pressure difference or weight of a model combustor is found to be less than 1 % of the total value. Therefore, here we discuss only the deformation by thermal stress.

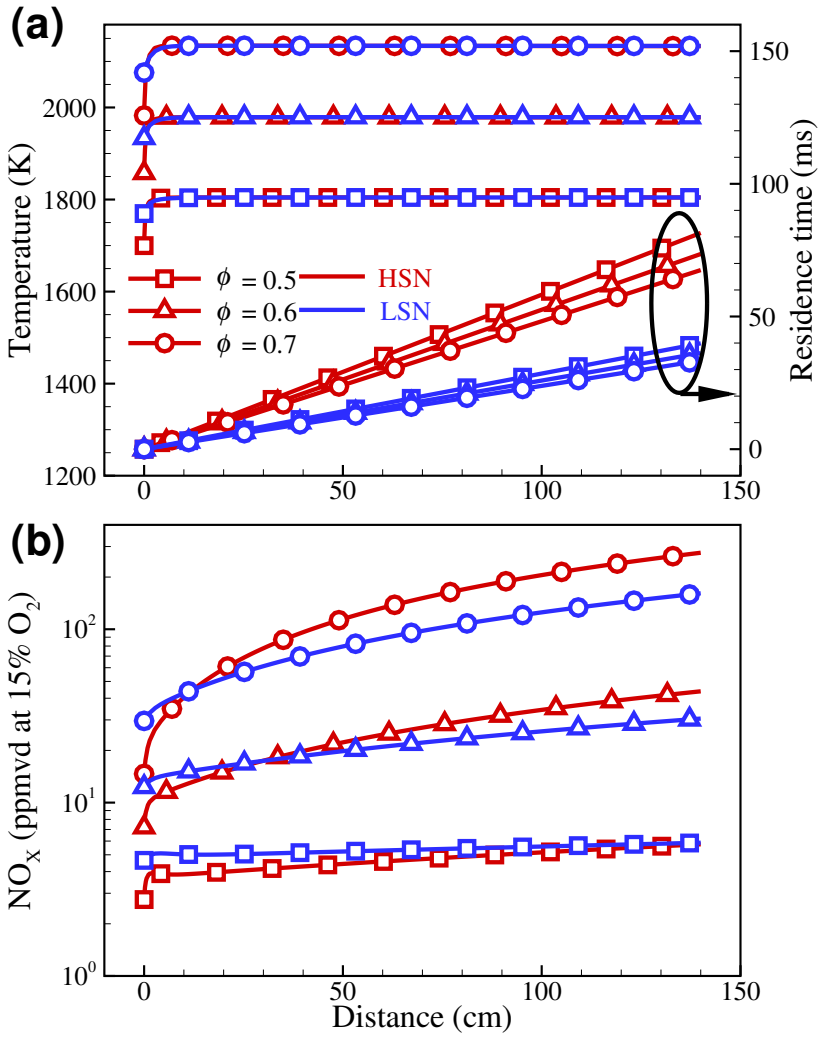

Figure 6.8: (a) Temperature, residence time and (b) amount of NO_X along the distance of plug flow reactor (PFR) in high/low swirler nozzle cases with different equivalence ratios.

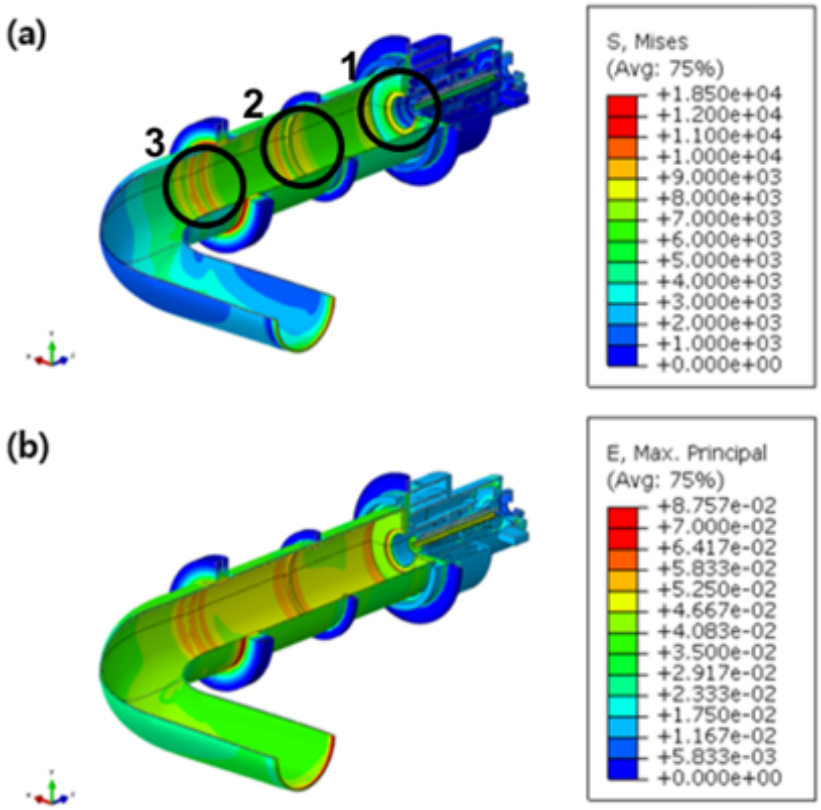

Figure 6.9: Contours of von Mises stress and maximum principal stress from finite element analysis.

Figure 6.9 shows the von Mises stress and maximum principal stress isocontours of the high swirler nozzle case at $\phi = 0.5$. The values of von Mises stress and the maximum principal stress are relatively large at the combustor liner due to combustion products, which is noticeable at three regions as follows: Region 1 is a single nozzle exit, and Regions 2 and 3 are fastened by additional structure. Basically, Region 1 composed of many parts is complicated, and the temperature variation is also large due to the coexistence of a fresh mixture and combustion products. Furthermore, in these regions, the material cannot be freely expanded due to the fixed parts. From this situation, fatal thermal fatigues can be caused by frequently turning on/off the power system.

If the combustion system is suddenly turned on, the dynamic responses at three representative areas where the thermal fatigue is expected are shown in Fig. 6.10. Overall, the strain amplitude, ε, initially oscillates with a large amplitude and then decays over time. The maximum strain amplitudes at region 1, 2, and 3 are 0.17, 0.12, and 0.08,

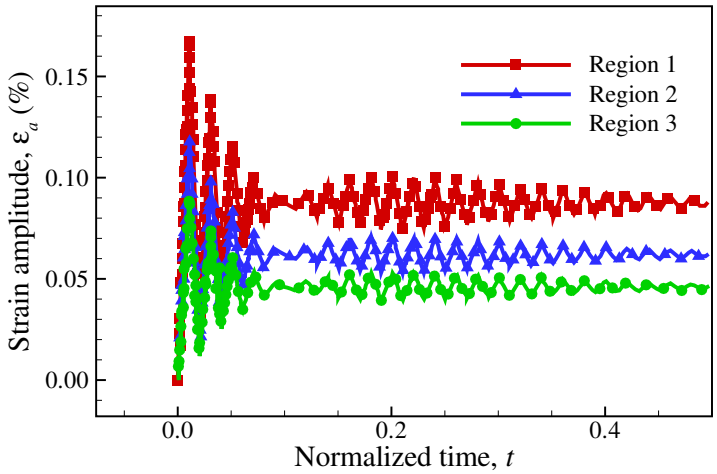

Figure 6.10: Strain amplitude, ε_a, response at three predicting damaged areas such as Region 1, 2, and 3.

respectively. In the steady state condition, the strain amplitudes are about 0.08, 0.06, and 0.05. The fatigue ε-N behavior of AISI type 304 stainless steel specimen with different temperature conditions has been already obtained in previous studies (see Fig. 1 in [127]). Although the temperature range is not included in the ε-N curve, this was used to investigate the cycles to failure, based on weak interaction with different temperature. From the behavior, in the present case, the fatigue life at Region 1 is estimated at approximately 4.0×10^5 cycles. Similarly, the cycles to fatigue of approximately 10^7 and 10^8 are obtained at Region 2 and 3, respectively. It is found that in the model combustor, the further away from the swirling flame, the longer the cycles to failure.

Figure 6.11 shows dynamic response at the weakest region to temperature variation. During gas turbine operation, unexpected situations such as over-/under-supply of fuel or oxidizer and cooling system problem can lead to unstable operating condition in the combustor. As in the previous analysis, the temperature and pressure fields are applied at Region 1, and then amount of fluctuation of temperature field continuously increases (decreases) to + 20 % (– 20 %) of the initial values. For the increase of temperature, dynamic response of the maximum of strain amplitude varies from 0.17 to 0.20. From the ε-N curve, the thermal fatigue life cycles can be estimated to be 1.4×10^5, 1/3 times of the cycles by the initial fluctuation. For the decrease case, on the other hands, the maximum

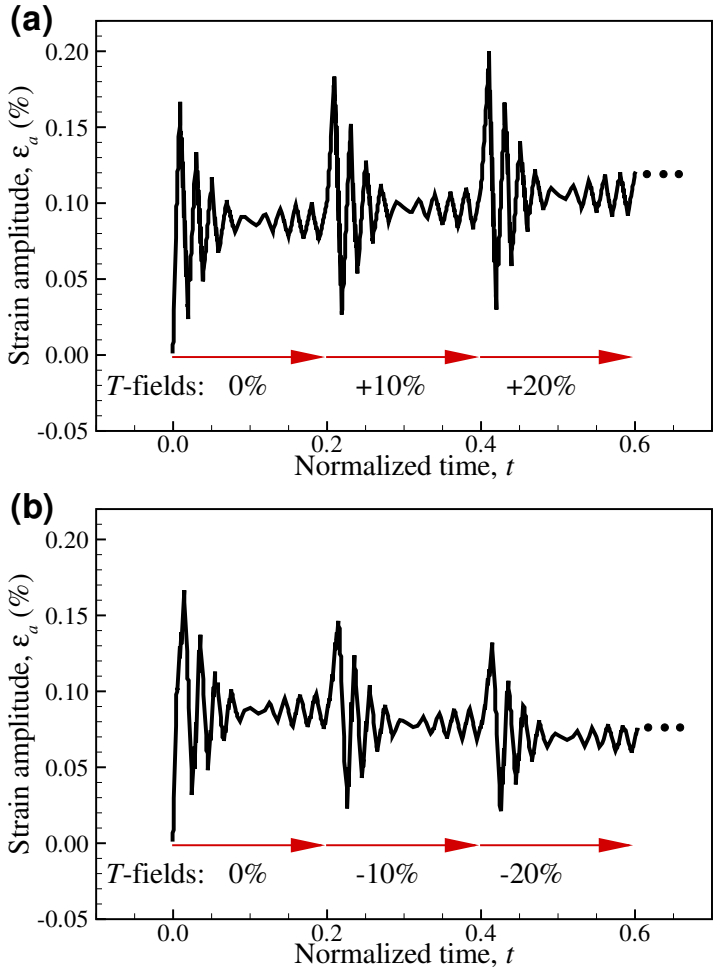

Figure 6.11: Dynamic response at the most vulnerable region with (a) increasing and (b) decreasing temperature.

value of 0.14 is obtained in the third period. The life increases to 2.86×10^6, around 7 times of that at the initial time. These results indicate that the material life decreases more for high temperature conditions. Finally, in a model gas turbine combustor, the cycles to failure under different temperature fields and strain amplitudes are summarized as shown in Fig. 6.12. It is expected that the life of AISI type 304 stainless steel is significantly reduced by the high strain amplitude from the high temperature.

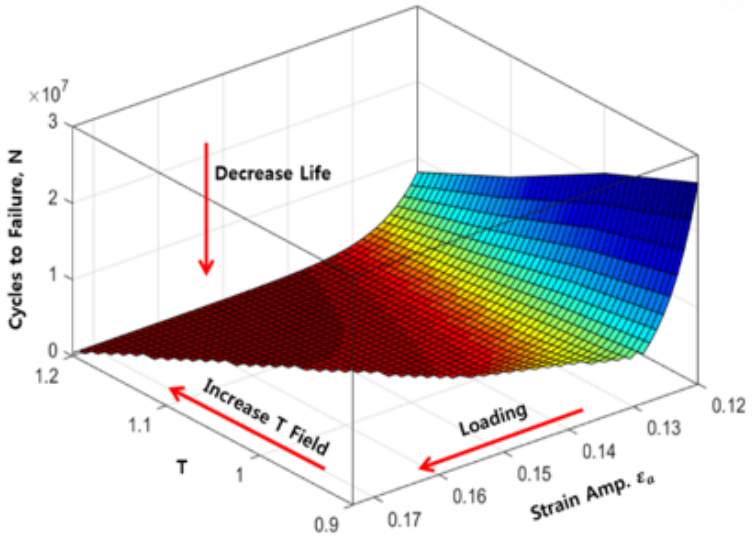

Figure 6.12: Cycles to failure under different temperature fields and strain amplitudes.

6.3 Conclusions

This study investigated the characteristics of turbulent combustion, NO_X emission, and fatigue life cycles of a model gas turbine combustor by performing 3-D RANS simulations, chemical reactor network analysis, and thermal fatigue analysis based on the ε-N curve. The results are summarized as follows:

1. The axial velocity and temperatures of the 3-D RANS simulations for the nonreacting and reacting cases were compared with experiments, which shows reasonable accuracy (1.48 % and 3.72 % errors, respectively).

2. For all cases with the high/low swirler nozzle, a V-shaped flames are observed. However, the length and angle of the flames for the high swirler nozzle cases are found to be shorter and higher than those of the low swirler nozzle cases. Relatively strong recirculation zones develop for the high swirler cases such that the outer (inner) recirculation zone is enlarged (shrunken) compared to that for the low swirler cases.

3. The maximum flame temperature for both high and low swirler nozzle cases increases with increasing equivalence ratio from 0.5 to 0.7. The maximum tempera-

ture occurs at the outer recirculation zone because this region is significantly heated while being confined by a swirling flame.

4. The amount of NO_X emission is reduced with decreasing flame temperature. At the post flame zone, NO_X emission continues to increase due to the residence time. Initially, relatively large amount of NO_X is generated for the low swirler nozzle case due to the relatively high temperature. However, the residence time of the combustion products within the post flame zone for the high swirler nozzle cases is two times larger than that for the low swirler nozzle cases, and hence, the NO_X amount at the exit for the high swirler nozzle become larger than that for the low swirler nozzle cases.

5. Through the finite element analysis, the maximum von Mises stress and maximum principal stress are found to occur at the joint parts of the combustor. Furthermore, from the dynamic responses of strain amplitude to temperature variation, Region 1 located behind a single nozzle is found to be the most vulnerable area due to the complicated components and large temperature difference between relatively cold pre-mixture and heated products by reactions.

6. It is found through a series of numerical simulations that the thermal fatigue analysis based on the ε-N curve can be used to predict the cycles to failure at specific regions. The increase of temperature aggravates the thermal fatigue problem while the decrease of temperature relieves it in the combustor.

Chapter VII

Conclusions

In the present study, the flame instabilities of opposed non-premixed tubular flames and comprehensive combustion characteristics including NO_X emission under conventional and supercritical oxy-fuel combustion conditions have been numerically investigated in the adiabatic and non-adiabatic condition.

The cellular formation by the diffusive-thermal instability are observed near the stretch-induced extinction limit, $Da_{E,S}$. As using two different initial conditions such as the perturbed IC ($\sim O(\varepsilon)$) and C-shaped IC ($\sim O(1)$), the reason why the discrepancy between the experiment and numerical prediction by the linear stability analysis appears is elucidated. The following results are obtained:

- The region of cellular instability and the number of flame cells, obtained from the 2-D simulations with the perturbed IC, are predicted by the linear stability analysis with good agreement.
- The number of flame cells from the 2-D simulations with the C-shaped IC is smaller than the results with the perturbed IC.
- Once the cellular flames appears in the cases of the C-shaped IC, the number of flame cells remains constant until the global extinction.
- The horseshoe-shaped cellular flame is induced by the $O(1)$ disturbance from the unintended and locally-high stretch rate in experiments.

The D-T instability of the opposed non-premixed tubular flame is not only observed near the stretch-induced extinction limit as described in Chapter II, but also near the radiation-induced extinction. The effects of radiative heat loss on opposed non-premixed tubular flames are arranged as follows:

- From 2-D simulations with the perturbed IC, the flame response is divided into four different regimes: (1) Regime I – a noncellular flame with decaying oscillation, (2) Regime II – a cellular flame with decaying oscillation, (3) Regime III – a cellular flame with growing oscillation, and (4) Regime IV – total extinction with growing oscillation.

- The flame behaviors near the radiation-induced extinction limit, such as the number of flame cells and the critical Das, are also predicted by the linear stability analysis with good agreement.

- Depending on relative strength of two flame cell from different initial flames, the total extinction through the head-on collision or a rotating flame cell are found beyond the radiation-induced extinction Da.

- Under the extremely-high radiative intensity condition, flame instabilities occur through the whole combustible regime.

The NO_X emission characteristics and pressure effects on counterflow non-premixed flames have been investigated under sCO_2 oxy-fuel combustion conditions. The application of real gas models to the OPPDIF code [103] shows good agreement with the thermodynamic and transport properties with NIST REFPROP data [1]. The results are summarized as follows:

- The amount of NO_X for the case with N_2 in the oxidizer stream is approximately ten times larger than that for the case with N_2 in the fuel stream.

- As the mole fraction of N_2 and O_2 increases, the $EINO_X$ increases. Additionally, it is found that the variation of $EINO_X$ is more sensitive to the amount of O_2 than that of N_2.

- The relative contribution of prompt NO_X is found to be negligible under sCO_2 oxy-fuel combustion conditions.

- The relative contribution of NO_X reburn pathway increases with increasing pressure.

To identify the thermal radiation effect on CH_4 versus O_2/CO_2 counterflow non-premixed flames under sCO_2 oxy-fuel combustion conditions, the different WSGG models are estimated and applied to 1-D numerical simulations. The results are obtained as follows:

- The two WSGG models are estimated by different extrapolation ways: one is the WSGG-Log model that estimates the absorption coefficients and emissivity by reasonably extrapolating the data within 1–30 bar of Shan et al. [68] and the other is the WSGG-Linear model that estimates $\kappa_{p,i}$ as $\kappa_i P$, based on traditional WSGG model [114].

- The temperature difference between the adiabatic and WSGG models at 300 bar is less than 1% of adiabatic flame temperature in most range of strain rate.

Finally, numerical simulations of a model gas turbine combustor with two different nozzles are conducted by using commercial softwares. The numerical models are validated by the comparison with the velocity and temperature values at specific points measured in experiments. The conclusions are described as follows:

- The maximum flame temperature for both high and low swirler nozzle cases decreases with the decrease of equivalence ratio from 0.7 to 0.5.

- The NO_X amount at the exit is meaningfully decided by the flame temperature and the residence time within the post flame zone.

- The finite element analysis and thermal fatigue analysis based on the ε-N curve can predict the most vulnerable area damaged by the thermal fatigue and the cycles to failure.

7.1 Future Work

Over the past few decades, in the combustion field, many researchers have been willing to try to develop the clean and efficient combustion technology to preserve the environment and save the energy. To develop new combustion technology, both of theoretical and practical study are necessary to understand phenomena under new conditions. In this context, the importance of CFD simulations cannot be emphasized enough because of many advantages; to reduce the development cost; to obtain comprehensive and detailed information unlike experiments that give limited data from limited sensors and measurements; to try a variety of designs and conditions in design process. Also, the development of high performance computing enables us to solve the larger and more complex problems.

As mentioned before, Pitz and coworkers have been already studied on the various characteristics of premixed and non-premixed tubular flames [3, 15, 16, 18–20, 22, 23, 85]. In [18], a study on both of negatively-curved and positively-curved diffusion flames was numerically conducted by the comparison between opposed jet flames and opposed non-premixed tubular flames. Chen and Ju [128] investigated the effects of curvature, stretch and radiation on extinction limit of positively-curved premixed flames. As such, the tubular configuration is widely used to study on the curvature effects on flames because of the advantage of uniform stretch and curvature which can be varied independently. However, detailed investigation on negatively-curved premixed tubular flames have not been conducted. In addition, the radiation effects on premixed and non-premixed flames with different magnitude and sign of the curvature will be identified by using tubular configuration.

Liang et al. [129] investigated the laminar flame speed of supercritical H_2/air and CH_4/air premixed flames. However, detailed investigation under various mixture condition have not been conducted. Also, it may show different results in premixed flames. In addition, Chen et al. [130] found that flame speed and flammability limit were affected by radiation absorption at elevated pressures up to 5 atm. In the context, the pre-mixture consist of strong absorber, CO_2, with relatively-low temperature will be heated by the relatively-high temperature products in the post flame zone. The effects of the thermal

radiation on premixed flames should be studied at extremely high pressure, although the reliable radiation model and chemical reaction mechanism at extremely high pressure may be needed.

Although the negligible influence of the radiation on counterflow non-premixed flames is carefully supposed under supercritical oxy-fuel combustion conditions, we genuinely have been curious about the radiative heat transfer in the real combustor. For instance, in the perspective of NO_X emission, the long residence time is one of the main causes of NO_X generation. To predict the amount of NO_X at the exit, 3-D large eddy simulations (LES) or RANS simulations of a model gas turbine combustor at extremely high pressure should be conducted with real gas models. In addition, the fundamental characteristics of turbulent flames will be investigated under supercritical oxy-fuel combustion.

References

[1] P. J. Linstrom and W. G. Mallard (Eds.), "NIST Chemistry WebBook, NIST Standard Reference Database Number 69," National Institute of Standards and Technology, Gaithersburg MD, 20899, USA, Tech. Rep., 2005.

[2] M. D. Bohon, T. F. Guiberti, S. M. Sarathy, and W. L. Roberts, "Variations in non-thermal NO formation pathways in alcohol flames," *Proc. Combust. Inst.*, vol. 36, pp. 3995–4002, 2017.

[3] R. W. Pitz, S. Hu, and P. Wang, "Tubular premixed and diffusion flames: Effect of stretch and curvature," *Prog. Energy. Combust. Sci.*, vol. 43, pp. 1–34, 2014.

[4] J. Buckmaster, "Edge-flames," *Prog. Energy. Combust. Sci.*, vol. 28, pp. 435–475, 2002.

[5] C. K. Law, *Combustion Physics*. Cambridge University Press, 2006.

[6] B. J. Lee, C. S. Yoo., and H. G. Im, "Dynamics of bluff-body-stabilized premixed hydrogen/air flames in a narrow channel," *Combust. Flame*, vol. 162, pp. 2602–2609, 2015.

[7] C. K. Law and C. J. Sung, "Structure, aerodynamics, and geometry of premixed flamelets," *Prog. Energy Combust. Sci.*, vol. 26, pp. 459–505, 2000.

[8] Y. X. Xin, C. S. Yoo, J. H. Chen, and C. K. Law, "A DNS study of self-accelerating cylindrical hydrogen-–air flames with detailed chemistry," *Proc. Combust. Inst.*, vol. 35, pp. 753–760, 2015.

[9] M. Matalon, "Flame dynamics," *Proc. Combust. Inst.*, vol. 32, pp. 57–82, 2009.

[10] R.-H. Chen, G. B. Mitchell, and P. D. Ronney, "Diffusive-thermal instability and flame extinction in nonpremixed combustion," *Proc. Combust. Inst.*, vol. 24, pp. 213–221, 1992.

[11] J. S. Kim, "Linear analysis of diffusional-thermal instability in diffusion flames with Lewis numbers close to unity," *Combust. Theory Model.*, vol. 1, pp. 13–40, 1997.

[12] J. S. Kim and S. R. Lee, "Diffusional-thermal instability in strained diffusion flames with unequal Lewis numbers," *Combust. Theory Model.*, vol. 3, pp. 123–146, 1999.

[13] M. Short, J. Buckmaster, and S. Kochevets, "Edge-flames and sublimit hydrogen combustion," *Combust. Flame*, vol. 125, pp. 893–905, 2001.

[14] M. Matalon and P. Metzener, "The effect of thermal expansion on diffusion flame instabilities," *J. Fluid Mech.*, vol. 647, pp. 453–472, 2010.

[15] S. W. Shopoff and P. Wang and R. W. Pitz, "The effect of stretch on cellular formation in non-premixed opposed-flow tubular flames," *Combust. Flame*, vol. 158, pp. 876–884, 2011.

[16] ——, "Experimental study of cellular instability and extinction of non-premixed opposed-flow tubular flames," *Combust. Flame*, vol. 158, pp. 2165–2177, 2011.

[17] A. Liñán, "The asymptotic structure of counterflow diffusion flames for large activation energies," *Acta Astron.*, vol. 1, pp. 1007–1039, 1974.

[18] P. Wang and S. Hu and R. W. Pitz, "Numerical investigation of the curvature effects on diffusion flames," *Proc. Combust. Inst.*, vol. 31, pp. 989–996, 2007.

[19] S. Hu, R. W. Pitz., and Y. Wang, "Extinction and near-extinction instability of non-premixed tubular flames," *Combust. Flame*, vol. 156, pp. 90–98, 2009.

[20] S. Hu and R. W. Pitz., "Structural study of non-premixed tubular hydrocarbon flames," *Combust. Flame*, vol. 156, pp. 51–61, 2009.

[21] J. D. Buckmaster and M. Short, "Cellular instabilities, sublimit structures and edge-flames in premixed counterflows," *Combust. Theory Model.*, vol. 3, pp. 199–214, 1999.

[22] C. A. Hall, W. D. Kulatilaka, J. R. Gord, and R. W. Pitz, "Quantitative atomic hydrogen measurements in premixed hydrogen tubular flames," *Combust. Flame*, vol. 161, pp. 2924–2932, 2014.

[23] C. A. Hall, W. D. Kulatilaka, N. Jiang, J. R. Gord, and R. W. Pitz, "Minor-species structure of premixed cellular tubular flames," *Proc. Combust. Inst.*, vol. 35, pp. 1107–1114, 2015.

[24] V. N. Kurdyumov, "Diffusive-thermal instability of premixed tubular flames," *Combust. Flame*, vol. 158, pp. 1718–1726, 2011.

[25] P. D. Ronney, "Effect of chemistry and transport properties on near-limit flames at microgravity," *Combust. Sci. Technol.*, vol. 59, pp. 123–141, 1988.

[26] ——, "On the mechanisms of flame propagation limits and extinguishment-processes at microgravity," *Proc. Combust. Inst.*, vol. 22, pp. 1615–1623, 1989.

[27] P. D. Ronney, "Understanding combustion processes through microgravity research," *Proc. Combust. Inst.*, vol. 27, pp. 2485–2506, 1998.

[28] L. K. Honda and P. D. Ronney, "Effect of ambient atmosphere on flame spread at microgravity," *Combust. Theory Model.*, vol. 133, pp. 267–291, 1998.

[29] J. D. Buckmaster and G. Joulin and P. D. Ronney, "The structure and stability of nonadiabatic flame balls," *Combust. Flame*, vol. 79, pp. 381–392, 1990.

[30] ——, "The structure and stability of nonadiabatic flame balls: II. Effects of far-field losses," *Combust. Flame*, vol. 84, pp. 411–422, 1991.

[31] J. D. Buckmaster and P. D. Ronney, "Flame-ball drift in the presence of a total diffusive heat flux," *Proc. Combust. Inst.*, vol. 84, pp. 2603–2610, 1998.

[32] M. S. Wu, J. B. Liu, and P. D. Ronney, "Numerical simulation of diluent effects on flame balls," *Proc. Combust. Inst.*, vol. 27, pp. 2543–2550, 1998.

[33] M. S. Wu, P. D. Ronney, R. O. Colantonio, and D. B. Vanzandt, "Detailed numerical simulation of flame ball structure and dynamics," *Combust. Flame*, vol. 116, pp. 387–397, 1999.

[34] J. Daou, F. Al-Malki, and P. D. Ronney, "Generalized flame balls," *Combust. Theory Model.*, pp. 269–294, 2009.

[35] U. Bonne, "Radiative extinguishment of diffusion flames at zero gravity," *Combust. Flame*, vol. 16, pp. 147–159, 1971.

[36] J. S. T'ien, "Diffusion flame extinction at small stretch rates: the mechanism of radiative loss," *Combust. Flame*, vol. 65, pp. 31–34, 1986.

[37] ——, "The possibility of a reversal of material flammability ranking from normal gravity to microgravity," *Combust. Flame*, vol. 80, pp. 355–357, 1990.

[38] T. Daguse, T. Croonenbroek, J. C. Rolon, N. Darabiha, and A. Soufiani, "Study of radiative effects on laminar counterflow $H_2/O_2/N_2$ diffusion flames," *Combust. Flame*, vol. 106, pp. 271–287, 1996.

[39] K. Maruta, M. Yoshida, H. Guo, Y. Ju, and T. Niioka, "Extinction of low-stretched diffusion flame in microgravity," *Combust. Flame*, vol. 112, pp. 181–187, 1998.

[40] F. C. Frate, H. Bedir, C. J. Sung, and J. S. T'ien, "On flammability limits of dry CO/O_2 opposed-jet diffusion flames," *Proc. Combust. Inst.*, vol. 28, pp. 2047–2054, 2000.

[41] S. L. Olson and J. S. T'ien, "Buoyant low-stretch diffusion flames beneath cylindrical pmma samples," *Combust. Flame*, vol. 121, pp. 439–452, 2000.

[42] B. Han and A. F. Ibarreta and C. J. Sung and J. S. T'ien, "Experimental low-stretch gaseous diffusion flames in buoyancy-induced flowfields," *Proc. Combust. Inst.*, vol. 30, pp. 527–535, 2005.

[43] ——, "Structure of low-stretch methane nonpremixed flames," *Combust. Flame*, vol. 149, pp. 173–190, 2007.

[44] Y. Ju, H. Matsumi, K. Takita, and G. Masuya, "Combined effects of radiation, flame curvature, and stretch on the extinction and bifurcations of cylindrical CH_4/air premixed flame," *Combust. Flame*, pp. 580–592, 1999.

[45] S. Tang, M. K. Chernovsky, H. G. Im, and A. Atreya, "A computational study of spherical diffusion flames in microgravity with gas radiation. Part I: Model development and validation," *Combust. Flame*, vol. 157, pp. 118–126, 2010.

[46] S. Tang, H. G. Im, and A. Atreya, "A computational study of spherical diffusion flames in microgravity with gas radiation. Part II: Parametric studies of the diluent effects on flame extinction," *Combust. Flame*, vol. 157, pp. 127–136, 2010.

[47] S. Cheatham and M. Matalon, "Heat loss and Lewis number effects on the onset of oscillations in diffusion flames," *Proc. Combust. Inst.*, vol. 26, pp. 1063–1070, 1996.

[48] S. Kukuck and M. Matalon, "The onset of oscillations in diffusion flames," *Combust. Theory Model.*, vol. 5, pp. 217–240, 2001.

[49] C. H. Sohn, J. S. Kim, S. H. Chung, and K. Maruta, "Nonlinear evolution of diffusion flame oscillations triggered by radiative heat loss," *Combust. Flame*, vol. 123, pp. 95–106, 2000.

[50] V. Nayagam and F. A. Williams, "Dynamics of diffusion flame oscillations prior to extinction during low gravity droplet combustion," in *Seventh International Conference on Numerical Combustion*, 1998, p. 46.

[51] J. R. Nanduri, C. J. Sung, and J. S. T'ien, "Structure and dynamic response of radiative diffusion flames," *Combust. Theory Model.*, vol. 9, pp. 515–548, 2005.

[52] R. J. Allam, M. R. Palmer, G. W. Brown, J. Fetvedt, D. Freed, H. Nomoto, M. Itoh, N. Okita, and C. Jones, "High efficiency and low cost of electricity generation

from fossil fuels while eliminating atmospheric emissions, including carbon dioxide," *Energy Procedia*, vol. 37, pp. 1135–1149, 2013.

[53] R. J. Allam, S. Martin, B. Forrest, J. Fetvedt, X. Lu, D. Freed, G. W. Brown, T. Sasaki, M. Itoh, and J. Manning, "Demonstration of the Allam cycle: An update on the development status of a high efficiency supercritical carbon dioxide power process employing full carbon capture," *Energy Procedia*, vol. 114, pp. 5948–5966, 2017.

[54] Y. Iwai, M. Itoh, Y. Morisawa, S. Suzuki, D. Cusano, and M. Harris, "Development approach to the combustor of gas turbine for oxy-fuel, supercritical CO_2 cycle," in *Proceedings of the ASME Turbo Expo 2015: Turbine Technical Conference and Exposition*, Montrèal, Canada, 2015.

[55] T. H. Kim, J. W. Park, H. Y. Park, J. Park, J. H. Park, and I. G. Lim, "Chemical and radiation effects on flame extinction and NO_x formation in oxy-methane combustion diluted with CO_2," *Fuel*, vol. 177, pp. 235–243, 2016.

[56] K.-P. Cheong, P. Li, F. Wang, and J. Mi, "Emissions of NO and CO from counterflow combustion of CH_4 under MILD and oxyfuel conditions," *Energy*, vol. 124, pp. 652–664, 2017.

[57] M. C. Drake and R. J. Blint, "Relative importance of nitric oxide formation mechanisms in laminar opposed-flow diffusion flames," *Combust. Flame*, vol. 83, pp. 185–203, 1991.

[58] S. V. Naik and N. M. Laurendeau, "LIF measurements and chemical kinetic analysis of nitric oxide formation in high-pressure counterflow partially premixed and nonpremixed flames," *Combust. Sci. Technol.*, vol. 176, pp. 1809–1853, 2004.

[59] J. C. Hewson and M. Bollig, "Reduced mechanisms for NO_x emissions from hydrocarbon diffusion flames," *Symp. (Int.) Combust.*, vol. 26, pp. 2171–2179, 1996.

[60] D. T. Banuti, P. C. Ma, J.-P. Hickey, and M. Ihme, "Thermodynamic structure of supercritical LOX-GH2 diffusion flames," *Combust. Flame*, vol. 196, pp. 364–376, 2018.

[61] J. Delimont, N. Andrrews, and L. Chordia, "Exploration of combustor design for direct fired oxy-fuel application in a sCO_2 power cycle," in *GPPS Montreal 18 - Global Power and Propulsion Forum*, Montreal, Canada, 2018.

[62] K. S. Jung, H. S. Bak, N. D. Nguyen, B. J. Lee, and C. S. Yoo, "Effects of N_2 ingress on the NO_x emission of CH_4 versus O_2/CO_2 counterflow non-premixed flames under supercritical oxy-fuel combustion conditions," *Combust. Flame*, vol. submitted, 2020.

[63] M. K. Denison and B. W. Webb, "A spectral line-based weighted-sum-of-gray-gases model for arbitrary RTE solvers," *ASME J. Heat Transfer*, vol. 115, pp. 1004–1011, 1993.

[64] C. Yin, L. C. R. Johansen, L. A. Rosendahl, and S. K. Kær, "New weighted sum of gray gases model applicable to computational fluid dynamics (CFD) modeling of oxy-fuel combustion: derivation, validation, and implementation," *Energy Fuels*, vol. 24, pp. 6275–6282, 2010.

[65] M. H. Bordbar, G. Węcel, and T. Hyppänen, "A line by line based weighted sum of gray gases model for inhomogeneous CO_2–H_2O mixture in oxy-fired combustion," *Combust. Flame*, vol. 161, pp. 2435–2445, 2014.

[66] S. H. Kang and C. S. Yoo, "A modification of the narrow band-based WSGG regrouping method for computation time reduction in non-gray gas radiation analysis," *Int. J. Heat Mass Transf.*, vol. 111, pp. 1314–1321, 2017.

[67] F. R. Centeno, R. Brittes, F. H. R. França, and C. V. da Silva, "Application of the WSGG model for the calculation of gas-soot radiation in a turbulent non-premixed methane-air flame inside a cylindrical combustion chamber," *Int. J. Heat Mass Transf.*, vol. 93, pp. 742–753, 2016.

[68] S. Shan, B. Qian, Z. Zhou, Z. Wang, and K. Cen, "New pressurized WSGG model and the effect of pressure on the radiation heat transfer of H_2O/CO_2 gas mixtures," *Int. J. Heat Mass Transf.*, vol. 121, pp. 999–1010, 2018.

[69] T. C. Lieuwen, *Unsteady combustor physics.* Cambridge University Press, 2012.

[70] T. Poinsot, "Prediction and control of combustion instabilities in real engines," *Proc. Combust. Inst.*, pp. 1–28, 2017.

[71] Y. J. Kim, D. K. Lee, and Y. Kim, "Experimental study on combustion instability and attenuation characteristics in the lab-scale gas turbine combustor with a sponge-like porous medium," *J. Mech. Sci. Technol.*, pp. 1879–1887, 2018.

[72] J. Hou, B. J. Wicks, and R. A. Antoniou, "An investigation of fatigue failures of turbine blades in a gas turbine engine by mechanical analysis," *Eng. Fail. Anal.*, pp. 201–211, 2002.

[73] V. Cuffaro, F. Cura, and R. Sesana, "Advanced life assessment methods for gas turbine engine components," *Procedia Engineering*, pp. 129–134, 2014.

[74] T. Sadowski and P. Golewski, "Detection and numerical analysis of the most efforted placed in turbine blades under real working conditions," *Computational Materials Science*, pp. 285–288, 2012.

[75] T. Tinga, J. F. van Kampen, B. de jager, and J. B. W. Kok, "Gas turbine combustor liner life assessment using a combined fluid/structural approach," *J. Eng. Gas Turbines Power*, pp. 69–79, 2007.

[76] A. Kelly and C. Zweben, *Comprehensive Composite Materials.* Pergamon Press, 2000.

[77] R. Agrawal, "Low cycle fatigue life prediction," *International Journal of Emerging Engineering Research and Technology*, pp. 5–15, 2014.

[78] D. Lee, J. Park, J. Jin, and M. Lee, "A simulation for prediction of nitrogen oxide emissions from lean premixed combustor," *J. Mech. Sci. Technol.*, pp. 1871–1878, 2011.

[79] J. Park, T. H. Nguyen, D. Joung, K. Y. Huh, and M. C. Lee, "Prediction of NO_X and CO emissions from an industrial lean premixed gas turbine combustor using a chemical reactor network model," *Energy Fuels*, pp. 1643–1651, 2013.

[80] T. H. Nguyen, S. Kim, J. Park, S. Jung, and S. Kim, "CFD-CRN validation study for NO_X emission prediction in lean premixed gas turbine combustor," *J. Mech. Sci. Technol.*, pp. 4933–4942, 2017.

[81] T. H. Nguyen, J. Park, S. Jung, and S. Kim, "A numerical study on NO_X formation behavior in a lean-premixed gas turbine combustor using CFD-CRN method," *J. Mech. Sci. Technol.*, pp. 5051–5060, 2019.

[82] R. J. Kee, F. M. Rupley, and J. A. Miller, "The CHEMKIN thermodynamic data base," Sandia National Labs., Livermore, CA, USA, Tech. Rep. SAND87-8215B, 1990.

[83] "ABAQUS, User's Manual, Version 2016," http://130.149.89.49:2080/v2016/index.html.

[84] C. S. Yoo, J. H. Chen, and J. H. Frank, "A numerical study of transient ignition and flame characteristics of diluted hydrogen versus heated air in counterflow," *Combust. Flame*, vol. 156, pp. 140–151, 2009.

[85] P. Wang, J. A. Wehrmeyer, and R. W. Pitz, "Stretch rate of tubular premixed flames," *Combust. Flame*, vol. 145, pp. 401–414, 2006.

[86] C. A. Kennedy, M. H. Carpenter, and R. M. Lewis, "Low-storage, explicit Runge—Kutta schemes for the compressible Navier-–Stokes equations," *Appl. Num. Math.*, vol. 35, pp. 117–219, 2000.

[87] C. A. Kennedy and M. H. Carpenter, "Several new numerical methods for compressible shear-layer simulations," *Appl. Num. Math.*, vol. 14, pp. 397–433, 1994.

[88] P. Metzener and M. Matalon, "Diffusive-thermal instabilities of diffusion flames: onset of cells and oscillations," *Combust. Theory Model.*, vol. 10, pp. 701–725, 2006.

[89] C. H. Gibson, "Find structure of scalar fields mixed by turbulence. I. Zero-gradient points and minimal gradient surfaces," *Phys. Fluids*, vol. 11, pp. 2305–2315, 1968.

[90] T. Echekki and J. H. Chen, "Structure and propagation of methanol–air triple flames," *Combust. Flame*, vol. 114, pp. 231–245, 1998.

[91] H. G. Im and J. H. Chen, "Structure and propagation of triple flames in partially premixed hydrogen–air mixtures," *Combust. Flame*, vol. 119, pp. 436–454, 1999.

[92] C. S. Yoo, R. Sankarna, and J. H. Chen, "Three-dimensional direct numerical simulation of a turbulent lifted hydrogen jet flame in heated coflow: flame stabilization and structure," *J. Fluid Mech.*, vol. 640, pp. 453–481, 2009.

[93] C. S. Yoo, E. S. Richardson, R. Sankaran, and J. H. Chen, "A DNS study on the stabilization mechanism of a turbulent lifted ethylene jet flame in highly-heated coflow," *Proc. Combust. Inst.*, vol. 33, pp. 1619–1627, 2011.

[94] C. S. Yoo, T. Lu, J. H. Chen, and C. K. Law, "Direct numerical simulations of ignition of a lean n-heptane/air mixture with temperature inhomogeneities at constant volume: Parametric study," *Combust. Flame*, vol. 158, pp. 1727–1741, 2011.

[95] C. S. Yoo, Z. Luo, T. Lu, H. Kim, and J. H. Chen, "A DNS study of ignition characteristics of a lean iso-octane/air mixture under HCCI and SACI conditions," *Proc. Combust. Inst.*, vol. 34, pp. 2985–2993, 2013.

[96] M. B. Luong, Z. Luo, T. Lu, S. H. Chung, and C. S. Yoo, "Direct numerical simulations of the ignition of lean primary reference fuel/air mixtures with temperature inhomogeneities," *Combust. Flame*, vol. 160, pp. 2038–2047, 2013.

[97] S. O. Kim, M. B. Luong, J. H. Chen, and C. S. Yoo, "A DNS study of the ignition of lean PRF/air mixtures with temperature inhomogeneities under high pressure and intermediate temperature," *Combust. Flame*, vol. 162, pp. 717–726, 2015.

[98] C. A. Hall and R. W. Pitz, "Experimental and numerical study of H_2-air non-premixed cellular tubular flames," *Proc. Combust. Inst.*, vol. 36, pp. 1595–1602, 2017.

[99] D. L. Jacono, A. Bergeon, and E. Knobloch, "Spatially localized radiating diffusion flames," *Combust. Flame*, vol. 176, pp. 117–124, 2017.

[100] H. S. Bak, S. R. Lee, J. H. Chen, and C. S. Yoo, "A numerical study of the diffusive-thermal instability of opposed nonpremixed tubular flames," *Combust. Flame*, vol. 162, pp. 4612–4621, 2015.

[101] S. Cheatham and M. Matalon, "A general asymptotic theory of diffusion flames with application to cellular instability," *J. Fluid Mech.*, vol. 414, pp. 105–144, 2000.

[102] C. H. Sohn, I. M. Jeong, and S. H. Chung, "Numerical study of the effects of pressure and air-dilution on NO formation in laminar counterflow diffusion flames of methane in high temperature air," *Combust. Flame*, vol. 130, pp. 83–93, 2002.

[103] A. E. Lutz, R. J. Kee, J. F. Grcar, and F. M. Rupley, "OPPDIF: A Fortran program for computing opposed-flow diffusion flames," Sandia National Labs., Livermore, CA, USA, Tech. Rep. SAND-96-8243, 1997.

[104] G. Soave, "Equilibrium constants from a modified Redlich-Kwong equation of state," *Chem. Eng. Sci*, vol. 27, pp. 1197–1203, 1972.

[105] M. S. Grabosi and T. E. Baubert, "A modified Soave equation of state for phase equilibrium calculations. 1. Hydrocarbon systems," *Ind. Eng. Chem. Process Des. Dev.*, vol. 17, pp. 443–450, 1978.

[106] R. C. Reid, J. M. Prausnitz, and B. E. Polling, *The properties of liquids and gases*, 4th ed. McGraw Hill, New York, 1987.

[107] T.-H. Chung, M. Ajlan, L. L. Lee, and K. E. Starling, "Generalized multiparameter correlation for nonpolar and polar fluid transport properties," *Ind. Eng. Chem. Res.*, vol. 27, pp. 671–679, 1988.

[108] S. Takahashi, "Preparation of a generalized chart for the diffusion coefficients of gases at high pressures," *J. Chem. Eng. Jpn.*, vol. 7, pp. 417–420, 1974.

[109] "San Diego Mechanism web page," http://combustion.ucsd.edu.

[110] H. Wang, X. You, A. V. Joshi, S. G. Davis, A. Laskin, F. Egolfopoulos, and C. K. Law, "USC Mech Version II. High-Temperature Combustion Reaction Model of H_2/CO/C_1–C_4 Compounds," http://ignis.usc.edu/USC_Mech_II.htm.

[111] W. K. Metcalfe, S. M. Burke, S. S. Ahmed, and H. J. Curran, "A hierarchical and comparative kinetic modeling study of C_1–C_2 hydrocarbon and oxygenerated fuels," *Int. J. Chem. Kinet.*, vol. 45, pp. 638–675, 2013.

[112] T. Takeno and M. Nishioka, "Species conservation and emission indices for flames described by similarity solutions," *Combust. Flame*, vol. 92, pp. 465–468, 1993.

[113] S. J. Klippenstein, M. Pfeifle, A. W. Jasper, and P. Glarborg, "Theory and modeling of relevance to prompt-NO formation at high pressure," *Combust. Flame*, vol. 195, pp. 3–17, 2018.

[114] M. F. Modest, *Radiative heat transfer*, 3rd ed. Elsevier Science, 2013.

[115] A. E. Lutz, R. J. Kee, J. F. Grcar, and F. M. Rupley, "OPPDIF: A Fortran program for computing opposed-flow diffusion flames," Sandia National Labs., Livermore, CA, USA, Tech. Rep. SAND-96-8243, 1997.

[116] G. P. Smith, D. M. Golden, M. Frenklach, N. W. Moriarty, B. Eiteneer, M. Goldenberg, C. T. Bowman, R. K. Hanson, S. Song, W. C. Gardiner, V. V. Lissianski, and Z. Qin, "GRI-Mech 3.0," http://combustion.berkeley.edu/gri-mech.

[117] C. S. Yoo and H. G. Im, "Transient soot dynamics in turbulent nonpremixed ethylene-air counterflow flames," *Proc. Combust. Inst.*, vol. 31, pp. 701–708, 2007.

[118] H. S. Bak and C. S. Yoo, "Flame instabilities and flame cell dynamics in opposed nonpremixed tubular flames with radiative heat loss," *Combust. Flame*, vol. 194, pp. 322–333, 2018.

[119] A. K. Gupta, D. G. Lilley, and N. Syred, *Swirl flows*. Abacus Press, 1984.

[120] "Ansys academic research cfd, fluent 2019 r2."

[121] C. K. Westbrook and F. L. Dryer, "Simplified reaction mechanisms for the oxidation of hydrocarbon fuels in flames," *Combust. Sci. Technol.*, pp. 31–43, 1981.

[122] P. D. Harvey, *Engineering Properties of Steels*. ASM International, 1982.

[123] D. Peckner and I. M. Bernstein, *Handbook of Stainless Steels*. McGraw-Hill Book Company, 1977.

[124] H. E. Boyer and T. L. Gall, *Engineering Properties of Steels*. ASM International, 1985.

[125] A. I. H. Committee, *Metals Handbook*. ASM International, 1990.

[126] J. Driscoll and J. Temme, "Role of swirl in flame stabilization," in *49th AIAA Aerospace Sciences Meeting including the New Horizons Forum and Aerospace Exposition*, Orlando, Florida, USA, 2011.

[127] O. K. Chopra, "Development of a fatigue design curve for austenitic stainless steels in lwr environments: A review," in *Proceedings of the ASME 2002 Pressure Vessels and Piping Conference. Pressure Vessel and Piping Codes and Standards*, Vancouver, BC, Canada, 2002.

[128] Z. Chen and Y. Ju, "Combined effects of curvature, radiation, and stretch on the extinction of premixed tubular flames," *Int. J. Heat Mass Transf.*, pp. 6118–6125, 2008.

[129] W. Liang, W. Li, and C. K. Law, "Laminar flame propagation in supercritical hydrogen/air and methane/air mixtures," *Proc. Combust. Inst.*, vol. 37, pp. 1733–1739, 2019.

[130] Z. Chen, "Studies of radiation absorption on flame speed and flammability limit of CO_2 diluted methane flames at elevated pressure," *Proc. Combust. Inst.*, pp. 2693–2700, 2007.

Acknowledgements

I would like to express my sincere gratitude to my advisor Prof. Chun Sang Yoo for great advices and assistance in my doctoral program. It is lucky for me that my advisor is him. I truly respected to the his insightful counsel on my research and even my life. I also thank to my doctoral committee members - Prof. Jaeseon Lee, Prof. Jae Hwa Lee, Prof. Jooha Kim, and Prof. Jeong Park, for their valuable comments on my thesis.

I always appreciate my group members because we have worthily discussed the research and even sharing our daily life. Their passion, potential, and performance have inspired me. I am probably not going to forget about lots of great memories with them. I will always miss them everywhere. Finally, I am also grateful to my family for believing and waiting for me. Without their unconditional support, I cannot complete this work.

This work was supported by BK21Plus funded by the Ministry of Education and by Basic Science Research Program through the National Research Foundation of Korea (NRF) funded by the Ministry of Science.